Title
Effects of osteoporosis therapies on bone biomechanics

Author
Easley, Sarah Kathleen

Publication Date
2010

Peer reviewed|Thesis/dissertation

Effects of Osteoporosis Therapies on Bone Biomechanics

by

Sarah Kathleen Easley

A dissertation submitted in partial satisfaction of the

requirements for the degree of

Doctor of Philosophy

in

Engineering – Mechanical Engineering

in the

Graduate Division

of the

University of California, Berkeley

Committee in charge:

Professor Tony M. Keaveny, Chair
Professor Panayiotis Papadopoulos
Professor Kevin E. Healy

Fall 2010

Effects of Osteoporosis Therapies on Bone Biomechanics

by

Sarah Kathleen Easley

ABSTRACT

Effects of Osteoporosis Therapies on Bone Biomechanics

by

Sarah Kathleen Easley

Doctor of Philosophy in Engineering – Mechanical Engineering

University of California, Berkeley

Professor Tony M. Keaveny, Chair

Anti-fracture therapies for the treatment of osteoporosis have been shown clinically to reduce the incidence of fracture; however, standard clinical measurements of bone density cannot sufficiently explain these large reductions. Therefore, the overall goal of this research is to develop a better understanding of the mechanisms through which anti-fracture therapies improve bone strength — a critical determinant of fracture risk — which should lead to improved assessment of treatment efficacy.

Combining the latest advances in micro-computed tomography and high-resolution micro-CT-based finite element modeling, we used repeated measures and parameter variations to isolate specific biomechanical effects of various bone characteristics that can be altered by disease and treatment. Specifically, we found that simulated microcavities in trabecular bone from a wide range of bone volume fraction and microarchitecture reduced the strength and altered the relationship between strength and bone volume fraction. While this effect was greater in low-density bone and when the microcavities were targeted to regions of high tissue strain, an appreciable biomechanical effect persisted for all types of bone. Since previous work with antiresorptive-treated canine bone did not find such an effect, questions remain regarding accurate representation of the morphology and micromechanics of actual resorption-induced cavities. Despite these uncertainties, our results provide new insight into the clinical relevance of stress risers caused by resorption cavities, suggesting that antiresorptive therapies may be most effective via mitigation of stress risers in a subset of patients with low bone volume fraction and high bone turnover.

Studying vertebrae from treated rats revealed that any treatment-induced changes in intra-specimen variations in tissue mineralization, as detected by quantitative micro-CT, had a negligible biomechanical effect at the whole bone level and in isolated trabecular bone. Intra-specimen variations in tissue mineralization did have a role in general biomechanical behavior, but this role was remarkably uniform across the four different treatment groups: sham control, ovariectomized (OVX), OVX+PTH, and

OVX+raloxifene. Finite element results showed that biomechanical treatment effects were dominated by treatment-induced changes in geometry and microarchitecture.

This research also produced an efficient pre-clinical framework for characterizing bone quality which should provide considerable insight into the mechanisms of biomechanical effects in a broad range of bone research applications, including aging, diseases, and pharmaceutical and genetic therapy. The approach takes advantage of the hierarchical structure of bone by evaluating the most biomechanically relevant characteristics at each physical scale to isolate the source of bone quality effects and prescribing subsequent analysis only when such effects are found. Using this framework, we found that neither ovariectomy nor PTH treatment had a net effect on bone quality of rat vertebrae during compressive loading suggesting that the observed changes in vertebral strength were primarily due to changes in bone quantity.

In closure, this dissertation research has increased knowledge regarding the mechanisms through which osteoporosis therapies improve bone strength without appreciably increasing bone mass. Further, it provides new methods for pre-clinical assessment of treatment efficacy. This dissertation also outlines areas of research to further advance our understanding of the effects of disease and drug therapies on bone biomechanics in human bone.

TABLE OF CONTENTS

LIST OF FIGURES

LIST OF TABLES

ACKNOWLEDGEMENTS

First, I would like to thank my advisor and mentor, Tony Keaveny, for providing me the opportunity to conduct my doctoral research in the Orthopaedic Biomechanics Lab. His enthusiasm, insight, and expert knowledge have been an inspiration throughout my time in the lab. I would also like to thank all the members of the OBL for making the lab a fun and supportive place to work. I would especially like to thank Aaron Fields for everything that comes with occupying the desk next to me for five years as we navigated the twists and turns of our graduate program together. His friendship has been invaluable. I owe a great deal of gratitude to Grant Bevill, Senthil Eswaran, and Carolyn Sparrey for their patient mentoring and immeasurable help and guidance. I also thank Jenni Buckley, Chris Chaplin, John Christensen, Bryan Fan, Wes Jackson, Mike Jekir, Fjóla Jóhannesdóttir, Liam Mullins, Shashank Nawathe, Javier Reina, Alissa Romens, Arnav Sanyal, Josuke Tanaka, Xiang Wang, and Jesse Woo for their smiling faces, inspiration, knowledge, and assistance. I would like to extend a special thank you to Chase Bennett, Michael Chang, Ting-Ting Chen, George Lu, Dmitriy Shindich, David Torello, and Ivana Yi for their contributions to this work; their unique perspectives and enthusiasm for the research was always refreshing. I am grateful to Chris Hernandez and Galateia Kazakia for providing opportunities for collaboration and for the mentorship and advice they gave along the way. I would also like to acknowledge Andy Burghardt and Sharmila Majundar for their assistance with the micro-CT imaging of the bones in this work. Finally, I am grateful Professors Panos Papadopoulos and Kevin Healy for serving on my dissertation committee.

I would like to acknowledge the National Institutes of Health (Grants AR43784, AR54448, AR47838) and Pfizer Inc. for providing funding support for this research. I also received support through fellowships from the College of Engineering and the Department of Mechanical Engineering. Computational resources were available through Grant UCB-266 from the National Partnership for Computational Infrastructure and through Grant MCA00N019 from TeraGrid.

On a more personal front, I would like to thank Sara Atwood. She has been a wonderful friend, running partner, bridesmaid, study-buddy, and all around superstar. I cannot imagine my time at Berkeley without her friendship and I cannot begin to express my gratitude for her support, encouragement, insight and inspiration. I would also like to thank all of the ladies of the Graduate Women of Engineering for providing a supportive community of fantastic, like-minded women. I am also grateful to my dear friend Sandy Freund for her continued support from afar as well as all the care packages and comic relief. She reminds me that there is life outside of grad school.

Finally, I offer a humongous thank you to my family for their unconditional love and support throughout my graduate studies. I am grateful to my Mom and Dad for everything — they have had the largest influence on my life and have inspired me to never give up your dreams. I thank my sister Jessica and soon-to-be brother-in-law Chris especially for doing most of the leg work for a multitude of backpacking trips in the Sierra which has provided much-needed rejuvenation in the fresh mountain air; those

trips together were always among the years' highlights. I am grateful to my sister Rachel for deciding on a moment's notice to move half way across the country to Berkeley to be my roomie so that I wouldn't have to live with a sketchy, random group of Craig's List people in a warehouse on San Pablo; I really value those years spent living together when she became my friend and not just my little sister. I also want to thank my in-laws, Steve and Lauri Metcalf, for their love and encouragement. Last, but certainly not least, I owe the hugest debt of gratitude to my husband, Chad. He has been patient and supportive throughout my time as a "perpetual student" even when it meant years of physical separation and ultimately uprooting his life to join me in the Bay Area. I know it hasn't always been easy with the stress and the late nights and I appreciate his love and steadfastness more than can be expressed.

1. INTRODUCTION

Osteoporosis is a skeletal disease characterized by low bone mass and deteriorated microarchitecture with a consequent increase in bone fragility and risk of fracture resulting from an imbalance in bone remodeling. The World Health Organization defines osteoporosis by an areal bone mineral density (BMD[1]) measurement — made with dual energy X-ray absortiometry (DXA) — that is 2.5 standard deviations below that of a sex-matched healthy young adult. Osteoporosis is a major public health problem; 50% of women and 25% of men over age 50 will have an osteoporotic fracture in their remaining lifetime [1]. According to the National Osteoporosis Foundation, in the United States, there are more than 2 million osteoporotic fractures annually with an associated health cost of $19 billion, and these numbers are expected to rise as the size of the aging population grows [1]. Fracture patients experience a decreased quality of life, often requiring long-term care, and one in four hip fracture patients over age 50 die within the year following fracture.

Osteoporosis can be treated with a variety of pharmaceuticals, however the biomechanical mechanisms through with these treatments work is not well understood. These treatments act by altering the bone remodeling process, either suppressing bone resorption to prevent further bone loss [2, 3] or increasing bone turnover to form new bone [2, 4, 5]. Drug therapy has been shown to reduce the incidence of osteoporotic fracture by about 50% (**Figure 1-1**) [6, 7], however, the associated small increase in areal BMD — 6-8% as measured by DXA — does not adequately explain this large reduction [8-10]. This observation has generated research interest in "bone quality" [11-17]. Bone quality is defined as the characteristics of a bone that influence its resistance to fracture, but are not accounted for with measures of bone quantity or density [12, 15, 18]. It has been suggested that drug treatments reduce fracture risk without large changes in bone density by improving bone quality. A better understanding of the mechanisms of fracture risk reduction should improve means of evaluating treatment efficacy and may even provide insight for new therapy development.

While many bone characteristics have been hypothesized as potential influences of bone strength and fracture efficacy [11-15], in practice, it is difficult to separate the biomechanical effects of bone mass, geometry, microstructure, and material properties because of the complex hierarchical nature of bone. As a result, many studies rely on correlation analysis between measures of various bone characteristics and bone strength [19-22]. However, because many characteristics are cross-correlated with measures of bone quantity [20], the actual mechanisms of strength and efficacy remain unknown.

In this context, the overall goals of this dissertation are to develop a better understanding of the effects of osteoporosis drug treatments on the biomechanical behavior of bone — a key determinant of fracture risk — using experimental and computational techniques. The initial focus of this dissertation is on biomechanical consequences of changes to the bone that directly result from altering the bone remodeling process. Then, the focus moves to the development of a systematic approach

[1] Areal bone mineral density (BMD) is not a true density measurement. It is calculated as the bone mineral content divided by the *area* of the scan, producing a measurement in units of g/cm^2.

for a comprehensive characterization of biomechanical bone quality, which may improve pre-clinical evaluation of drug therapies.

The remainder of this chapter provides a basic foundation in bone biology and biomechanics necessary to understand the material presented in this dissertation. First, the composition and structure of bone will be presented, followed by a description of the bone remodeling process and how it is affected by aging and osteoporosis. In the third section, an overview of the mechanical behavior of bone is provided. Then, the mechanisms of action of common osteoporosis drug treatments are discussed. This is followed by a description of current trends in computational modeling of bone, and finally an outline of the scope and objectives of this dissertation will be given.

1.1 Composition and Structure of Bone[2]

Bone is a composite material comprising inorganic and organic constituents. By weight, bone tissue is made of about 50-70% ceramic crystalline mineral, 20-40% organic material, and 5-10% water. The mineral is an impure form of hydroxyapatite ($Ca_{10}(PO_4)_6(OH)_2$); mineral crystals typically form as tiny plates 2-5 nm x 15 nm x 20-50 nm in size. The organic material is primarily Type I collagen (~90%), with small amounts of minor collagens and noncollageneous proteins. The triple-helix-shaped Type I collagen molecules arrange in parallel with gaps between each molecule. Mineralization is thought to begin in these gaps before spreading to form mineralized collagen fibrils (20-40 nm in diameter) — the basic building blocks of bone tissue.

The structure of bone is hierarchical in nature (**Figure 1-2**). At the submicron level, bone tissue is a composite of mineralized collagen fibrils. At the next level (~10 microns), these fibrils arrange either in thin sheets of unidirectional fibrils — called lamellae — which stack together with alternating fiber directions in each layer to form lamellar bone, or in random orientations to form woven bone, the latter being less common and typically occurring in situations of rapid growth or fracture healing. Lamellae organize into various forms on the next level (~500 microns). At the highest level (>1 mm), bone is composed of cortical and trabecular bone (**Figure 1-3**). Cortical bone is made of tightly packed lamellar, Haversian, laminar or woven bone. Haversian bone consists of 10-15 lamellae arranged in concentric cylinders about a central Haversian canal that contains blood vessel capillaries, nerves, and bone cells; this entire substructure is termed an osteon and represents the primary discrete unit of cortical bone. In contrast, trabecular bone is made of packets of less well-organized lamellae which form a highly porous network of plate-like and rod-like trabeculae surrounded by marrow space. The primary difference between cortical and trabecular bone is porosity. Where the porosity of cortical bone is less than 30%, and typically much less in healthy bone, the porosity of trabecular bone is greater than 60% and can be as much as 95% in an elderly vertebra.

[2] This section was adapted in part from [23].

1.2 Mechanical Behavior of Bone

The mechanical behavior of bone is determined by bone quantity, shape, cortical and trabecular microstructure, and mechanical properties of the bone tissue. Bone is a highly heterogeneous material which results in large variations in apparent-level strength and elastic modulus across anatomic sites, individuals, and species (the term "apparent" refers to properties of bone measured at the continuum level and thus accounts for both material properties and structure, as opposed to "tissue" properties measured on the scale of a individual trabeculae). Measures of bone mass or density, such as bone mineral density (BMD) or trabecular bone volume fraction, are very good predictors of bone strength [24-28] but are not able to completely describe variations in bone strength. Factors that contribute to bone strength but are not accounted for by bone mass or density are termed bone quality factors [15]. Two bones with the same bone density but different strengths would be considered to have different bone quality (**Figure 1-4**). As mentioned above, much research has been generated on the concept of bone quality to work toward a better understanding of the mechanisms through which osteoporosis drug treatments improve bone strength — thereby reducing fracture risk — beyond increasing bone density. A large number of potential bone characteristics at all hierarchical levels — from the molecular level to the whole bone level — have been proposed as potentially important bone quality factors [11-15] (**Table 1-1**); a selection of these will be addressed in detail in subsequent chapters of this dissertation.

The stress-strain behavior of bone is qualitatively similar for cortical and trabecular bone and across the range of densities and microarchitectures but magnitudes can vary substantially. Because of its composite nature and complex microstructure, bone is an anisotropic material. Cortical bone is approximately transversely isotropic, meaning that it is has a primary axis — the longitudinal direction, parallel to the osteons — and is isotropic in the plane perpendicular to that axis. The bone is stronger and stiffer along the primary axis. Trabecular bone is also anisotropic; it is stiffest and strongest in the direction of the primary trabecular orientation. Mechanical properties are typically reported for loading along the primary axis since this is the direction of habitual loading. In addition to anisotropy, bone also displays strength asymmetry. Bone is stronger and more ductile in compression than in tension.

Trabecular bone biomechanical properties depend on bone volume fraction and microarchitecture [29-32] and different mechanisms govern the failure of low- versus high-density trabecular bone [33, 34]. Trabecular bone with a high bone volume fraction (greater than about 20%) and with more a plate-like structure, such as that from the hip, is appreciably stiffer and stronger than trabecular bone with a low bone volume fraction and a more rod-like structure, such as that from the spine [23, 32]. Further, high-density bone fails due to wide-spread tissue damage while low-density bone tends to fail due to large deformations (e.g. bending and buckling) of a few trabeculae [34] such that less tissue overall is damaged at apparent failure [35]. These differences illustrate the heterogeneity within an individual and highlight that effects seen in one anatomic site may not extend to another anatomic site.

The mechanical properties of bone tissue depend on the constituents of the tissue, including the degree and distribution of mineralization [36-38], crystallinity [39],

characteristics of the collagen network [40, 41], and microdamage [42]. The degree of mineralization is directly related to the microhardness [43] and stiffness of bone tissue [36], while the collagen matrix provides tensile strength and viscoelasticity [40]. Meanwhile, microdamage accumulation decreases stiffness, strength [44] and fracture toughness [45]. Due to the complex hierarchical composite nature of bone tissue, the specific roles of each of these characteristics in bone mechanical properties remain unclear.

The relative roles of the cortical and trabecular compartments in bone strength and how these roles are affected by aging, disease, and treatment are also not well understood. Due to technical difficulty in removing the thin cortical shell (0.25-0.4 mm thick [46-49]), experiments have not been able to provide consistent results [50-52]. High-resolution (about 40-60 microns) micro-CT-based finite element analysis of human vertebral bodies which include geometric detail of the thin cortical shell and individual trabeculae showed that the cortical shell carries a substantial load during compression [53, 54]. At the mid-transverse plane of the vertebra, the fraction of the load carried by the cortical shell was maximum, being about 45% [54]. Importantly, the load fraction taken by the cortical shell did not depend on any densitometric or morphologic properties of the vertebra [54] indicating that the load-sharing mechanism between the cortical and trabecular compartments is complex and can not be determined by any single factor. In addition to an appreciable load-bearing role, the cortical shell also serves to maximize the load-carrying capacity of the trabecular compartment, particularly with the peripheral trabeculae, such that removal of the cortical shell decreases vertebral stiffness appreciably more than by the stiffness of the shell itself [55]. Previous studies of the cortical shell have focused on untreated elderly human vertebrae, thus it remains unclear how the role of the cortical shell is altered with osteoporosis and treatments.

1.3 Bone Remodeling

Bone is a remarkable material, able to adapt to a changing mechanical environment and replace old or damaged tissue through bone modeling and remodeling. Bone is continually renewing itself, though rate of remodeling depends on species, anatomic site, age, disease, and drug therapy [56]. Bone remodeling is a sequential action of osteoclastic bone cells and osteoblastic bone cells that is regulated by a network of embedded osteocyte cells that may sense strain or some other mechanical stimuli [57] — the exact process through which sites are selected for remodeling remains unclear (**Figure 1-5 A**). First, osteoclasts attach to bone surfaces and, over a period of a few weeks, produce an acid to dissolve existing collagen-mineral matrix, creating “Howships lacunae” or resorption cavities (**Figure 1-5 B**). Following resorption, osteoblasts synthesize new collageneous organic matrix — called osteoid — which experiences a rapid mineralization phase followed by a secondary mineralization phase over a period of about six months. The net result of each remodeling cycle is a new osteon. The process is essentially the same in cortical and trabecular bone, except that bone remodeling produces cylindrical tunnels through cortical bone while producing saucer-shaped cavities on the surfaces of trabecular bone [58]. Since there is more remodeling on the surfaces of trabecular bone than on internal surfaces of Haversian canals of cortical bone,

and newly formed bone is less mineralized than mature bone, trabecular bone tends to have a lower mean mineral density than cortical bone. Further, since remodeling is initiated at different sites at different times, and mineralization of the new tissue occurs over several months, there can be large intra-specimen spatial variation in mineral density within bone tissue, with surfaces having a lower mineral density than older, internal bone (**Figure 1-5 C**).

Osteoporosis results from an imbalance between bone resorption and bone formation [59]. The difference between the volume of bone removed and that that is replaced during the remodeling cycle is called bone balance. A negative bone balance results in a gradual thinning of cortices and trabeculae (**Figure 1-6**). A gradual thinning occurs with aging, but is accelerated by osteoporosis. To arrest this thinning, osteoporosis therapies act by altering the bone remodeling process. The mechanisms of action of various osteoporosis therapies and the consequent effects of altering remodeling on bone are discussed in the next section.

1.4 Mechanisms of Action of Osteoporosis Therapies

While there are a number of drug therapies approved for the treatment of osteoporosis, they can be classified into two basic categories: antiresorptive agents and anabolic agents [60]. These two classes of agents act through opposite effects on the bone remodeling process. Antiresorptive agents suppress bone remodeling thus stopping further bone loss and also preventing new bone formation; in contrast, anabolic agents stimulate bone remodeling to create new bone formation.

Antiresorptive agents, such as bisphosphonates, estrogen, and raloxifene, all inhibit osteoclast-mediated bone loss, thereby reducing bone turnover [12, 61-63]. Bone resorption is inhibited sooner than bone formation, improving the bone balance by providing a period in which bone volume is increased due to filling in of the resorption cavities [64, 65]. Further, since there are fewer skeletal remodeling sites, thus less new bone being formed, the secondary mineralization phase continues for the existing tissue [66] causing an increase in the degree of mineralization and decrease in tissue mineral heterogeneity [67-69]. This filling in of the remodeling space and increased mineralization associated with antiresorptive treatment lead to small increases in areal bone mineral density (BMD) [70-72] — the primary clinical metric for osteoporosis diagnosis and treatment evaluation.

Anabolic agents, such as parathyroid hormone (PTH, the only approved skeletal anabolic agent), stimulate bone formation earlier and to a greater extent than bone resorption to create a positive bone balance [7, 73, 74]. This increase in bone formation causes an increase in tissue mineral heterogeneity [75]. Further, bone geometry can be altered and trabecular microarchitectural reconstructed [5, 76]. Most notably, trabeculae are thickened and there is a conversion from a more rod-like structure to a more plate-like structure, typical of healthy bone [76]. It is thought that increases in trabecular bone volume may come at the expense of cortical bone through increased in cortical porosity [77-79]. However, effects of any increases in porosity could be offset by increases in cortical area and cortical thickness [77]. Increases in bone volume, particularly in the

trabecular compartment, associated with PTH treatment lead to relatively large increases in areal BMD, especially in the spine [7, 73].

Despite observed increases in areal BMD with treatment, it is difficult to make conclusions about the associated effects on the biomechanical properties of bone, and ultimately fracture risk, because of the poor relationship between increases in areal BMD and decreases in fracture incidence [8-10]. Mechanisms that may affect bone biomechanical properties disproportionately to changes in areal BMD can be classified into three categories: 1) alterations to tissue-level properties; 2) alterations to microarchitecture; and 3) alterations to the size or shape of the bone. This dissertation will address aspects of each of these categories.

Alterations to bone tissue characteristics including degree [67-69] and distribution [75] of mineral density, collagen cross-linking [80, 81], crystallinity [81, 82], and micro-damage [83, 84] may contribute to treatment efficacy through alteration of the mechanical properties of the bone tissue. While treatment-induced changes in these various tissue characteristics have been measured in clinical and animal studies, further research is necessary to determine the biomechanical effects of these observed changes and what, if any, net effects on whole bone properties exist.

Alterations to trabecular microarchitecture, including filling in of resorption cavities [85] and prevention of trabecular perforation [86] have been proposed as possible mechanisms through with antiresorptive therapies increase bone strength disproportionately to the changes in areal BMD. One theory suggests that the effect of antiresorptives is due primarily to the elimination of the disruptive effect of perforative resorption since there is theoretical evidence that trabecular discontinuity resulting from perforation accentuates reduction in bone biomechanical properties more than a uniform thinning of trabeculae [86]. A competing theory proposes that a resorption cavity acts as a “stress riser” and represents a focal weakness that puts the trabecula at greater risk of failure, particularly when supporting horizontally oriented trabeculae have been resorbed away, and that complete perforation is not necessary [85]. Since antiresorptives result in fewer and smaller resorption cavities [87, 88], this “stress riser” effect may be reduced with treatment. Simulations have shown that high stresses develop around observed resorption cavities [89] and that bone may be weakened disproportionately to the change in bone volume [90], however no stress rise effect was found in a canine study comparing control and antiresorptive-treated bone [91]. Thus, the stress riser theory remains poorly understood.

Alterations to the size or shape of a bone may also affect its biomechanical properties. One possibility is an increase in cortical thickness resulting from either a greater reduction in endocortical bone resorption than in periosteal formation, as might occur with antiresorptive therapy [92], or from increased periosteal bone formation from anabolic therapy [77]. Related, changes in the relative volume of cortical and trabecular bone may alter the load-transfer characteristics in a bone. These mechanisms have not been demonstrated, and pre-clinical studies should be used to test their validity.

Because of the complex hierarchical nature of bone, it is difficult to quantify the biomechanical effects associated with alterations to specific bone quality characteristics. Biomechanical experiments are well suited for assessing overall effects on whole bone

properties, but it is not possible to separate the effects of changes to geometry and microstructure from those of material properties. Thus, experiments alone have limited use in identifying specific mechanisms of treatment effects on bone strength. Computational modeling provides a method for isolating the biomechanical effects of individual bone quality characteristics through parameter studies.

1.5 High-resolution Finite Element Modeling of Bone

Computational modeling has become a valuable tool for studying various aspects of bone biomechanics. One type of computational modeling is high-resolution finite element modeling named because it is based on micro-scale images of bone at resolutions on the order of 5-60 microns generated from serial milling [93] or micro-imaging techniques (*e.g.* micro-computed tomography or magnetic resonance imaging). By building models from micro-scale images, they explicitly capture the microstructural detail of the bone. Image voxels are directly converted into 8-noded brick elements using a voxel-conversion technique to generate a finite element mesh [94]. Depending on the resolution of the images, these models can have a few million to hundreds of millions degrees of freedom. Due to the size of these models, typically linear finite element analysis is used to predict bone stiffness and provide initial tissue strains [29, 95, 96]. However, with the use of specialized hardware and software, materially and geometrically nonlinear high-resolution finite element analysis can be used to predict yield strength and tissue strains at failure [34].

The material properties of the bone tissue can be assigned to the elements in either a simplified fashion or in a way that more closely represents the true heterogeneity of bone tissue. Typically, material properties are approximated as isotropic and homogeneous, where the single value assigned to all elements may be constant across all specimens or may be specific to each specimen. Recent developments in micro-CT scanning technology has enabled mapping of grayscale values to mineral density through use of a calibration phantom [97, 98]. This enables the mineral density of each image voxel to be used to assign heterogeneous (isotropic) material properties based on an assumed modulus- or strength-density relationship for bone tissue [99, 100]. A chapter of this dissertation is dedicated to investigating whether inclusion of heterogeneous material properties is important for capturing differences in bone properties across individuals and for evaluating treatment effects.

Experimental testing remains the gold standard for measuring the biomechanical properties of bone, however, finite element analysis provides several advantages over experiments. First, finite element analysis is nondestructive; the same specimen can be tested in a number of configurations which can reduce the large number of specimens needed to account for biological heterogeneity [101]. Related, finite element analysis enables parametric variations to models such that the direct effect of individual parameters on bone properties can be evaluated in ways not possible with experiments alone [55, 90, 102-104]. Further, finite element analysis permits probing and quantification of tissue-level stress and strain distributions which can be useful for determining failure mechanisms and locations at highest risk of failure [96, 99, 105, 106].

High-resolution finite element models have been shown to predict apparent-level properties and tissue-level stress and strain distributions that are well correlated with those measured experimentally, providing some validation for this technique [34, 95, 107, 108]. Another benefit lies in combining finite element analysis with experimental testing to leverage the strengths of each technique to gain insight into such characteristics as tissue-level mechanical properties [109] and failure mechanisms [34].

The computational requirements for performing high-resolution finite element analysis are enormous, particularly when analyses include geometric and material nonlinearities. As such, specialized hardware and software is typically required. In this research, all analyses were conducted with a highly scalable, implicit finite element framework (Olympus [110]) implemented on parallel supercomputers. The computational cost of these analyses is offset by the benefit of studying bone micromechanics at a very high level of detail, critical for accounting for micro-scale effects such as changes to the remodeling space or intra-specimen variations in mineralization of bone tissue — two bone characteristics that were studied in this dissertation research.

1.6 Objectives and Scope

The overall goals of this dissertation research are to increase knowledge of the effects of osteoporosis drug therapies on the biomechanical behavior of bone and to identify mechanisms that may improve bone strength disproportionately to the increases in bone mass. The initial focus is on biomechanical consequences of changes to the bone that directly result from altering the bone remodeling process with pharmaceuticals. A second goal of this dissertation is to develop a framework for evaluating treatment effects on biomechanical bone quality. Apart from providing a basic science understanding of the mechanisms through which drug therapies improve bone strength, these studies will provide insight into potential improvements in evaluating treatment efficacy. A combination of biomechanical experiments and high-resolution micro-CT-based finite element modeling will be used on human and treated animal bone to accomplish these goals.

The first study presented (Chapter two) addresses the theory that suppression of resorption cavities is a mechanism of increasing trabecular bone strength without appreciably increasing bone mass by reducing the number of stress risers in the bone. Since it is possible that the stress-riser effect may be highly sensitive to bone volume fraction and microarchitecture, trabecular bone from multiple anatomic sites and species will be used to address this issue. Because of the technical difficulties in identifying resorption cavities — which are on the order of a few hundred microns wide and less than 50 microns deep — in an experimental setting, microcavities will be simulated and their biomechanical effects will be assessed with nonlinear high-resolution finite element analysis.

In Chapter three, the contribution of treatment-induced changes to the intra-specimen spatial variation in mineralization of bone tissue to the overall biomechanical effect of treatment will be addressed. In order to achieve a wide range of tissue mineralization phenotypes, vertebrae from rats from four distinct treatment groups — a

sham-operated control, an ovariectomized osteopenic control, and ovariectomized plus either an antiresorptive or anabolic treatment — will be examined. A repeated-measures study design of high-resolution finite element analysis of micro-CT images calibrated for mineral density measurements will enable (1) the separation of the biomechanical role of the spatial variation in mineralization from those of the mean degree of mineralization and microarchitecture; and (2) the determination of the biomechanical role of treatment-induced changes in mineralization in the trabecular compartment compared to the whole vertebra.

In Chapter four, a framework for characterizing the effects of disease and treatment on biomechanical bone quality is presented. The specific advantage of this approach is that it integrates treatment-induced effects at all hierarchical scales into a clinically-relevant result. The approach is applied to vertebra from three treatment groups to demonstrate its use and evaluate its performance.

Finally, Chapter five provides concluding remarks and suggests future directions for this research. The primary novelty of this work is its use of sophisticated high-resolution micro-CT-based finite element modeling, incorporating the latest advances in quantitative imaging technology, in a repeated-measures approach to address questions regarding biomechanical mechanisms of action of osteoporosis treatments. Identifying such mechanisms was previously intractable because the complex hierarchical nature of bone prevented the isolation of specific biomechanical effects of changes to individual bone quality characteristics.

Table 1-1: Some proposed characteristics of bone that may influence biomechanical bone quality, categorized by physical scale.

Scale (m)	Bone Characteristics
$>10^{-3}$	Whole bone size and shape Spatial distribution of bone density
10^{-6}-10^{-3}	Microarchitecture Porosity Cortical shell thickness Lacunar number and morphology Resorption cavity number, size, and distribution
10^{-9}-10^{-6}	Mineral and collagen distribution and alignment Microdamage type, amount, distribution
$>10^{-9}$	Collagen structure and cross-linking Mineral type and crystal alignment Collagen-mineral interfaces

Adapted from [15].

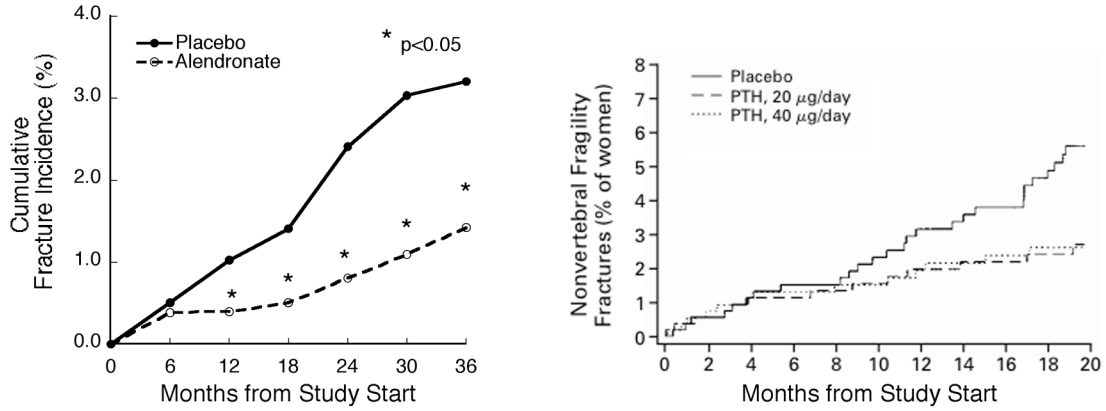

Figure 1-1: Compared to placebo, alendronate (left, data from the Fracture Intervention Trial involving 3658 osteoporotic women [6]) and recombinant PTH(1-34) (right, data for 1637 postmenopausal women [7]) therapies significant reduced the incidence of fracture in women. Data for alendronate study (left) reports incidence of fracture for the vertebra, hip, and wrist; data from the PTH study (right) reports incidence of *nonvertebral* fractures such as the hip, wrist, and ankle. **p*<0.05 alendronate vs. placebo. Statistics not available for PTH vs. placebo.

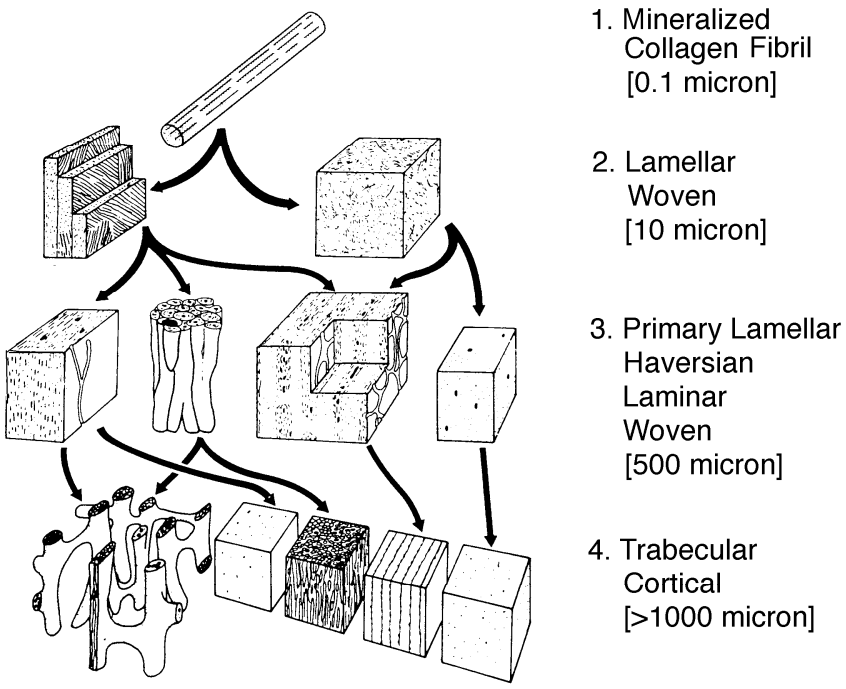

Figure 1-2: The hierarchical structures of bone from a submicron scale to several millimeters (adapted from [23]).

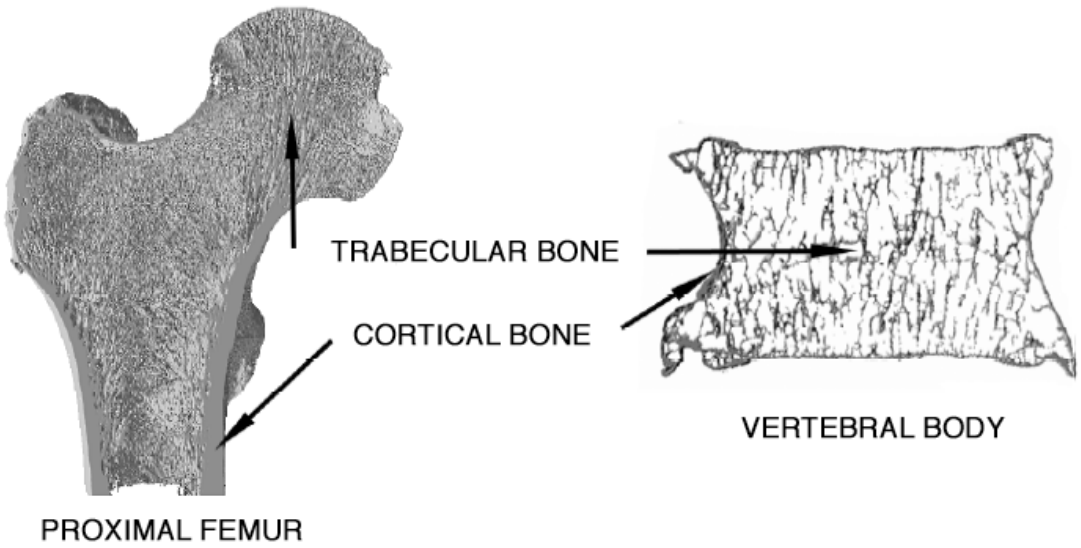

Figure 1-3: Cross-sections of a human proximal femur (hip) and a thoraric vertebral body (spine) show the typical arrangement of cortical and trabecular bone and illustrate the large variation in trabecular bone volume fraction and microarchitecture across anatomic sites.

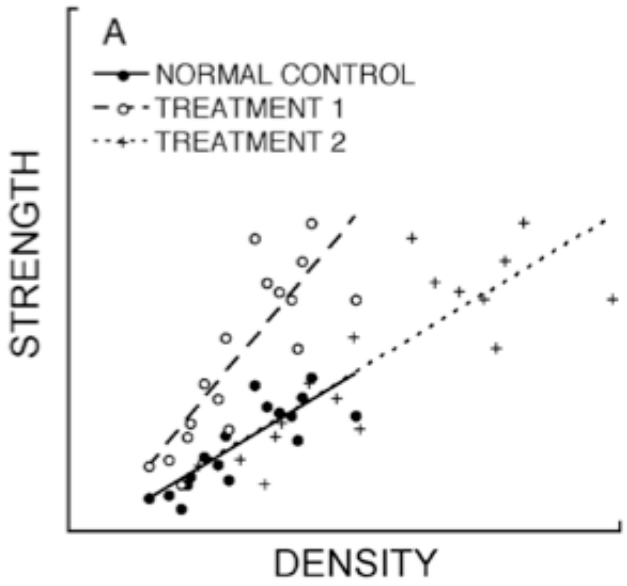

Figure 1-4: Hypothetical strength-density relationships for normal bone and bone from two different treatment group. Bone treatment groups show the same increase in strength. However the bone in treatment group 1 has the same density as the normal bone but the relationship between strength and density has an increased slope indicating improved bone quality; in contrast, the strength-density relationship for the bone in treatment group 2 is the same as for the control bone indicating that the increase in strength is due to the increase in density rather than improved bone quality (adapted from [15]).

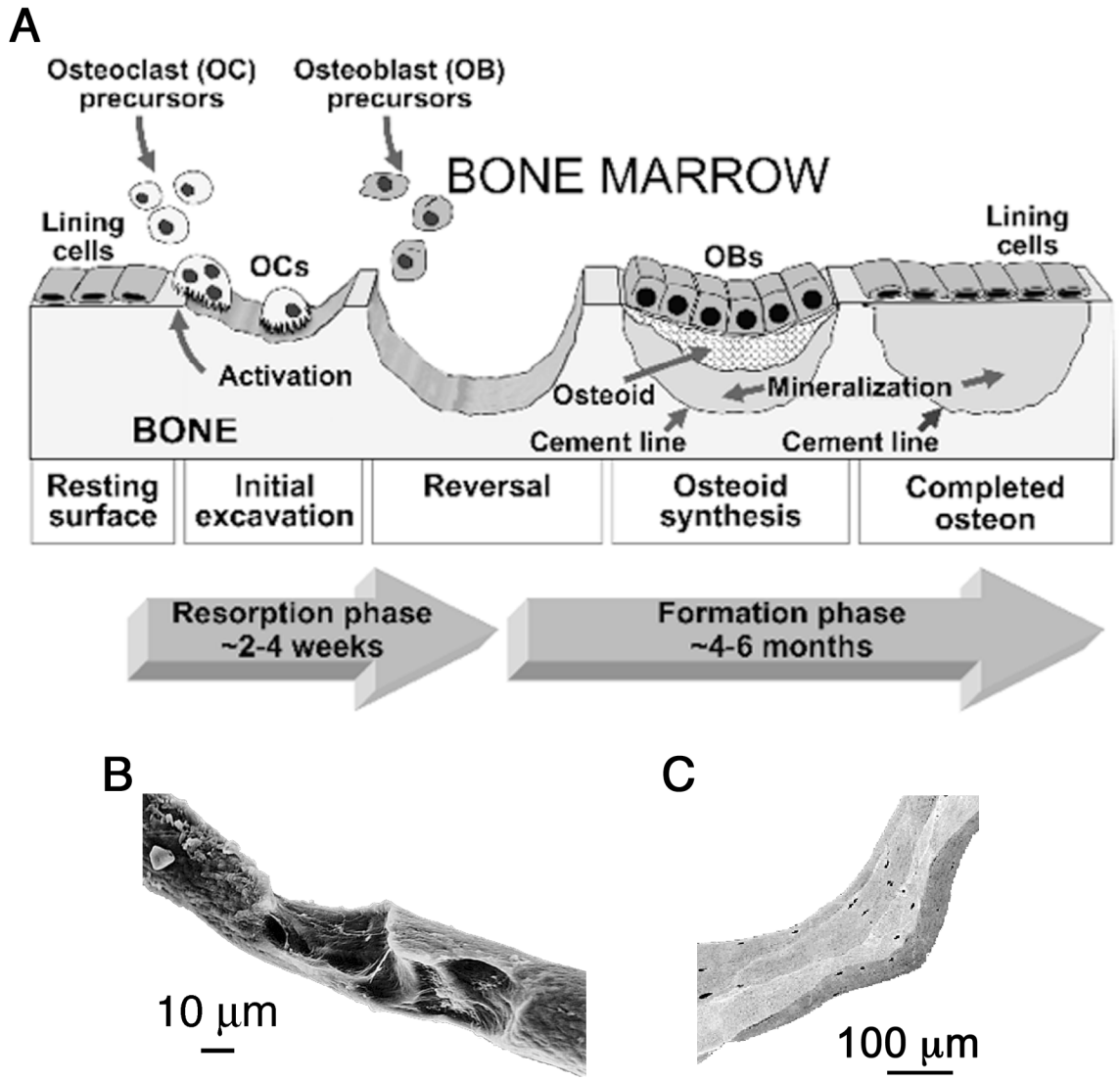

Figure 1-5: A cartoon representation of the timeline of the bone remodeling process in trabecular bone, shown in two-dimensions (A, adapted from [60]). An SEM image shows a cavity formed in a vertebral trabecula during remodeling (B, from [111]). Quantiative backscattered electron imaging shows the variation in mineralization within a trabecula resulting from bone packets (osteons) being deposited over time (C, [38]). Darker gray means lower mineral content — indicative of newer bone — while brighter gray means higher mineral content.

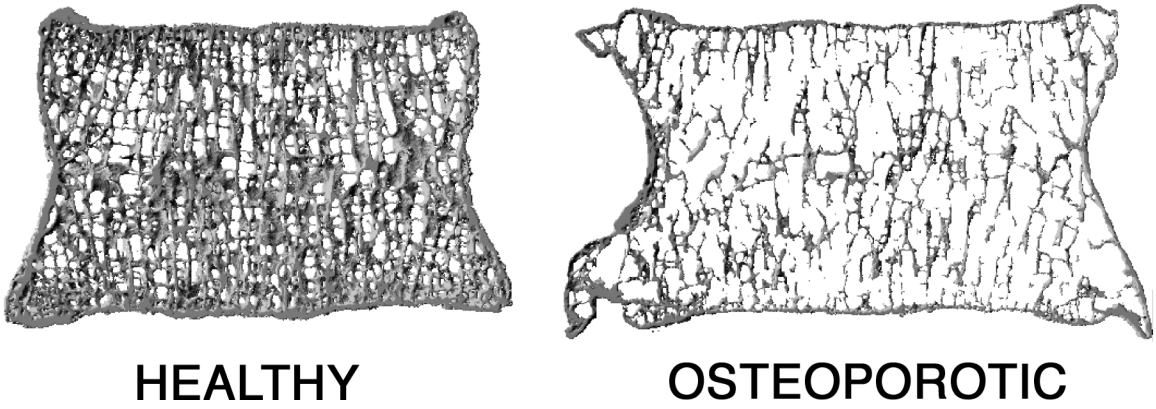

Figure 1-6: A comparison of frontal slices through the vertebra of a healthy individual and one from an elderly, osteoporotic individual illustrates the decrease in bone mass and deterioration in microarchitecture that occurs with osteoporosis.

2. BIOMECHANICAL EFFECTS OF SIMULATED RESORPTION CAVITIES IN TRABECULAR BONE ACROSS A WIDE RANGE OF BONE VOLUME FRACTION

2.1 Introduction

Despite the success of antiresorptive therapies in reducing osteoporotic fracture risk, there is an incomplete understanding of the underlying biomechanical mechanisms since fracture risk reductions are not commensurate with observed changes in areal bone mineral density (BMD) [8, 9]. One interesting theory is that suppression of resorption cavities, which occurs as a result of antiresorptive therapy, reduces "stress risers" in individual trabeculae, thus increasing bone strength without appreciably increasing bone mass [85]. However, this mechanism has never been demonstrated in real bone and remains poorly understood. Supporting the stress-riser effect, micro-CT-based finite element studies have shown high stresses around observed resorption cavities in individual trabeculae [89] and reductions in overall strength of cubes of low-density human trabecular bone in the presence of simulated microcavities [90]. However, refuting any stress-riser effect, a study on high-density trabecular bone from dogs treated with risedronate — a bisphosphonate expected to reduce the number or severity of stress risers — found no treatment effect on the relationship between strength and bone volume fraction [91]. One possible explanation for these conflicting findings is that the stress-riser effect may be highly sensitive to the bone volume fraction and microarchitecture of the trabecular bone, and thus may only have an appreciable biomechanical effect in low-density human bone. It is also possible that this effect may be mediated by the location of the microcavities within the trabecular bone [90]. Our goal in this simulation study was to test these hypotheses and in that way provide new insight into the stress riser theory as a mechanism for fracture efficacy of antiresorptive therapies.

2.2 Methods

Study design

We used micro-CT-based nonlinear finite element analysis, with and without simulated microcavities, to assess the strength behavior of excised cubes of canine vertebral trabecular bone (n=10) and elderly human vertebral (n=16) and proximal femoral (n=14) trabecular bone, which together spanned a wide range of microarchitecture and bone volume fraction (BV/TV). For each bone cube, three cavity scenarios were considered by repeated-measure parametric finite element analysis: 1) no cavities ("suppressed"), 2) cavities distributed randomly, and 3) cavities located in regions of most highly strained tissue. Each model was virtually compressed to failure to estimate the strength of the specimen for each of the three cavity scenarios. The effect of the microcavities on strength and strength-volume fraction relationships versus the model without cavities was then compared across the three groups.

Specimen preparation and imaging

Vertebrae were harvested from intact female beagle dogs (*n*=10 spines, T-10, age: 2-3 years) that belonged to the control group in a one-year antiresorptive treatment study [83]. Each canine vertebra was imaged with micro-CT (μCT 80, Scanco Medical AG) at 18-micron voxel size, and then this image was thresholded using an automated adaptive threshold algorithm (Scanco Medical AG) to separate bone tissue from the surrounding material. A cube (4 mm per side, BV/TV (mean ± SD): 22.6 ± 2.5%) was digitally removed from the vertebral body, avoiding the basivertebral foramen and the cortex.

Additionally, cylindrical cores (8 mm diameter) of cadaveric human trabecular bone from the vertebral body (*n*=16 spines, L4 or L5, 9 female/7 male, age range: 54-90 years, mean ± SD: 72.9 ± 11.7 years) and femoral neck (*n*=14 hips, 8 female/6 male, age range: 58-85 years, mean ± SD: 70.4 ± 10.1 years) were excised, each from separate donors with no documented history of metabolic bone disease (*e.g.* metastatic cancer, hyper- or hypothyroidism). Each bone specimen was imaged with micro-CT (μCT 40, Scanco Medical AG) at 22-micron voxel size. The resulting three-dimensional image was thresholded and then a cube (5 mm/side, BV/TV (mean ± SD) vertebral body: 11.2 ± 3.7%, femoral neck: 22.5 ± 5.9%) was digitally removed from the center of the cylinder. All cubes were aligned along the principal trabecular orientation. Using the original images, various trabecular microarchitectural parameters were measured (CTAn, SkyScan) for each specimen: trabecular thickness (Tb.Th), trabecular number (Tb.N), trabecular separation (Tb.Sp), and structure model index (SMI).

Resorption cavity models

Each image of the *n*=40 trabecular bone cubes was used to make three high-resolution finite element models by converting image voxels directly into 8-noded brick elements (18- or 22-micron edge length), resulting in a total of 120 finite element models (**Figure 2-1**). For each specimen, the first model was made from the original image to represent cavity suppression because, although some naturally-formed cavities likely exist, the cavities added to the other two models were not present (i.e. suppressed) in this original model. The second and third models were made from images in which microcavities were digitally added to the bone surfaces using a custom software [90]. In the second model, the microcavities were distributed randomly; in the third model, the microcavities were targeted to regions of greatest magnitude principal strain as determined with a preliminary linear elastic finite element analysis.

The size, shape, and number of the microcavities added to the bone images were based on measurements reported for human bone samples. Microcavities were saucer-shaped with a surface size of about 500 microns long by 200 microns wide [58, 112] and a maximum depth of 44 microns [113] — two finite elements at the resolution of these images (**Figure 2-1**). A total of 6% of the original volume of bone tissue was removed from each bone cube by the addition of these microcavities [87]. Cavities were allowed to overlap, but not completely disconnect any trabeculae.

Evaluation of bone strength

The 0.2% offset yield strength was estimated by virtually compressing each cube to failure in the direction of the principal trabecular orientation using nonlinear finite element analysis. In these analyses, both material and geometric nonlinearities were included to account for local tissue failure and large deformations of the trabeculae since these may be important mechanisms behind the effect of resorption cavities [85]. The bone tissue was modeled using a validated finite plasticity model that included tension-compression asymmetry [34, 114]. Each element in the models was assigned a tissue modulus reported previously for the respective anatomic site: 10 GPa for the human vertebral bone [104], and 18.5 GPa for the canine bone [91] and the human femoral bone [34, 104]. Poisson's ratio of 0.3 and tissue-level tensile and compressive yield strains of 0.33% and 0.81% [34], respectively, were assigned to all canine and human models. Each finite element model (n=120 total) contained between 0.6 and 4.3 million elements, depending on the volume fraction of each specimen, and was solved using a custom highly scalable, implicit finite element code [110] on a supercomputer (Datastar, San Diego, CA or Ranger, Austin, TX). Using 16-56 processors in parallel per analysis, the total time required for all analyses was approximately 550 hours.

Outcomes and statistics

To test our hypothesis, we compared the effect of microcavities on strength and the strength-volume fraction relationship across the three anatomic sites. Specifically, we tested for a relationship between the percent reduction in strength due to the simulated cavities and trabecular bone volume fraction, as well as the trabecular microarchitectural parameters. Then, we evaluated the effect of introducing microcavities on the relationship between yield strength and volume fraction for each anatomic site using repeated measures analysis of covariance in which bone volume fraction was the covariate (SPSS Statistics v18, SPSS Inc.). We also defined a normalized strength reduction metric to quantify the effect of microcavities on strength beyond the effect of reduced volume fraction ($\Delta S/\Delta S_{BV/TV}$, **Figure 2-2**). All tests were performed for both the random and high-strain cavity-placement schemes. Statistical significance is reported for $p<0.05$.

2.3 Results

Simulated microcavities reduced the yield strength of the trabecular bone for the three different anatomic sites ($p<0.0001$) although the magnitude of this effect depended on how the cavities were distributed within the bone and on bone volume fraction and trabecular microarchitecture (**Figure 2-3**). The effect for randomly-distributed microcavities was relatively constant (18.0 ± 2.7%; p=0.43 vs. BV/TV) across the range of volume fractions (5-36%) regardless of anatomic site; the small variation that did exist was associated with variation in trabecular thickness ($p<0.0001$). The effect for microcavities targeted to highly-strained tissue was always larger than that for random cavities, and was greater in more porous (BV/TV $p<0.0001$) and more rod-like bone (SMI $p<0.0001$). Thus, the difference in strength between specimens having microcavities placed in random locations compared to the same specimens having microcavities placed in regions of high-strain was greater in lower density bone.

The addition of microcavities also decreased the slope of the strength-volume fraction relationship — indicating reduced bone quality — in all cases ($p<0.001$), and this decrease was larger for cavities targeted to highly-strained tissue and for low-density bone (**Figure 2-4**, **Table 2-1**). When cavities were randomly distributed, the decrease in the slope of the strength-volume fraction relationship was constant (8%) regardless of anatomic site; the normalized strength reduction, $\Delta S/\Delta S_{BV/TV}$, indicated that the change in strength was about 70% larger than expected for the change in volume fraction and this also did not depend on anatomic site ($p=0.52$, **Figure 2-5**). In contrast, when cavities were targeted to highly-strained tissue, the slope of the strength-volume fraction relationship decreased by 21% and 19% in the high-density canine vertebral and human femoral neck bone, respectively, compared to 28% in the low-density human vertebral bone (**Table 2-1**). Importantly, the normalized strength reduction indicated the change in strength was 3-4 times larger than expected for the change in volume fraction and this also depended on anatomic site ($p=0.01$, **Figure 2-5**). These results indicate that there was an independent effect of the microcavities on strength in addition to the effect associated with removing 6% of the bone volume, and the size of this effect depended on the location of the simulated microcavities and on anatomic site.

2.4 Discussion

In our previous micro-CT-based finite element analysis of vertebral trabecular bone excised from dogs either treated or not treated with high doses of risedronate, we found no effect of treatment on the relationship between the predicted strength of the bone and bone volume fraction [91]. In that study, we used the same type of micro-CT-based finite element analysis as in this current study, but we did not simulate the placement of any microcavities — instead we relied on the actual morphology of the bone from the treated and untreated animals as observed from the micro-CT scans. On the basis of those findings, and our other prior study [90] in which we simulated microcavities in only low-density human vertebral bone we expected to find in this new study that stress riser effects caused by resorption cavities do not exist in high-density bone. However, our new results refute this. We infer from these collective findings that the type of simulation used in this study does not properly represent the morphology and/or micromechanics of resorption-induced cavities. At this juncture, however, the true biomechanical effects of stress risers are not known. It may be that appreciable stress risers exist in low-density bone, for example, if the microcavities occur in regions of high tissue strain; or, it may be that microcavities in fact have no appreciable biomechanical effect regardless of bone volume fraction, for example, if the microcavities are not targeted to regions of high tissue strain or if they occur in only very thin (and thus perhaps inconsequential) trabeculae. Thus, while our new results suggest that microcavities may have the greatest biomechanical effect when they occur in regions of high strain within low-density bone, the stress riser theory remains an enigma. Further research is therefore recommended to either support or refute this interesting theory.

In interpreting our results, one possible confounding issue is our assumption that the morphology and prevalence of resorption cavities are the same in canine and human bone. The size, shape, and number of cavities in all our simulations were based on

measurements reported for trabecular bone from postmenopausal women [58, 87, 112, 113] because such measurements have not been reported for canine trabecular bone. Histomorphometric analysis of canine trabecular bone suggests that the depth of cavities is similar to that in humans [88, 115, 116]. However, measurements in cortical bone — which are more straightforward to make than measurements in trabecular bone and therefore provide more reliable data [58] — found the diameter of Haversian remodeling sites were smaller in canine bone [117] than human bone [118]. If the cellular mechanisms associated with remodeling are largely the same on cortical and trabecular surfaces [58], then these measurements suggest that the depth of resorption cavities in trabecular bone may also be smaller in canine than human bone. If that is true, then the biomechanical effects of such different cavities would also differ since micro-CT-based finite element simulations have shown that shallower cavities reduced trabecular strength less than deeper cavities [119, 120]. Further, if there are fewer cavities in canine bone than in bone from postmenopausal women, then this too would reduce the magnitude of any stress riser effect. It is possible therefore that the stress riser effect does not exist in canine bone because cavities are smaller or fewer than assumed in our simulation study. If this can be confirmed, then our current results would suggest that an appreciable stress riser effect may exist in low-density postmenopausal bone, particularly if the stress risers are targeted to regions of high strain.

Another possibly confounding effect in interpreting these results relates to the fidelity of the finite element model, specifically in its ability to correctly model the stress field around any assumed microcavity. One important technical factor is the size of the finite elements relative to the size of the cavities and individual trabeculae. In this study, cavity depth (about 40-45 microns) corresponded to a depth of two cubic-shaped, 8-noded finite elements. Therefore, the geometric detail of the cavities was limited, as was the ability of such 8-noded brick elements to model complex stress fields. Recent work using very high resolution (0.7-microns in-plane) serial milling images of rat vertebrae found that resorption cavities could not be reliably identified when the images were coarsened to a voxel size greater than 1.4 *x* 1.4 *x* 5.0-microns. At such resolutions, finite element models of the specimen sizes used in this study would contain over a billion elements, which represents a challenging numerical problem. However, the findings in our previous canine bisphosphonate study [91], which used finite element models with the same element size as in this current study, were consistent with experimental results showing no effect on the relationship between compressive strength and areal BMD in canine vertebrae after treatment with the same bisphosphonate [121]. Thus, it remains unclear at this juncture if the element size in those finite element analyses was sufficient to capture any resorption cavities in the canine bone, or, if resorption cavities simply do not have an appreciable biomechanical effect in canine bone such that the resolution issue was not relevant in that (or this) study. Any future studies addressing stress risers should consider these factors related to morphology of microcavities and numerical convergence.

Despites these limitations, one major strength of the finite element-based cavity simulation technique is that it enables precise control over the size, number, and placement of microcavities and thus this study does provide unique insight into the effect of microcavities on trabecular strength. Another strength of this study was its use of a

repeated-measures study design to understand the importance of location of microcavities, *i.e.*, whether randomly placed or targeted to regions of high tissue strain. The statistical tests used with this type of study design are well powered to detect even subtle changes in bone strength and strength-volume fraction relationships. A further notable aspect of this study was its use of fully-nonlinear micro-CT-based finite element analysis, including both material and geometric nonlinearities. This technique has been well validated for assessment of strength in human trabecular bone [34, 95]. Regarding external validity, the bone samples included in this study spanned a wide range of densities, tissue morphologies, and donor ages indicating that any trends observed from this set should extend to a larger population.

Despite the remaining uncertainty of our overall understanding of stress risers as a mechanism by which antiresorptive treatments reduce fracture risk, our findings nevertheless provide new insight into the possible clinical relevance of stress risers. Based on our finding that microcavities have their greatest biomechanical effect when they occur in highly-strained bone tissue in low-density bone, it may be that antiresorptive therapies are most effective via stress-riser effect primarily in osteoporotic patients with a high rate of turnover and perhaps also in a subset of osteopenic patients who have high bone turnover and low bone volume fraction. High turnover would be associated presumably with a greater number of stress risers before treatment — and thus a higher risk of fracture due to compromised bone strength — and to a greater reduction in the number of stress risers as remodeling is suppressed by the antiresorptive. Consistent with this concept, high bone turnover is a known risk factor for fracture [122-126], and there is some evidence that patients with the highest levels of pretreatment turnover respond best to antiresorptive treatment [127-129], though further research is needed to determine the exact relationship between turnover, bone density, and treatment efficacy [130].

These simulations also provide insight into the mechanisms by which any stress riser effect may be greater in low-density bone. Our results indicate that any volume fraction- and anatomic site-dependent biomechanical effect of microcavities is likely due to a combination of factors. One factor is the difference in failure mechanisms between low- and high-density bone. Low-density bone is more likely to fail due to excessive bending and buckling of trabeculae [34] than high-density bone. Supporting this idea, we found that suppressing large deformations of trabeculae reduced the effect of microcavities in low-density bone but not in high-density bone, such that the effect of the cavities was more similar across the range of densities (**Appendix 7.1**). This indicates that the larger stress riser effect in low-density bone is due in part to the presence of microcavities increasing the susceptibility of trabeculae to fail by excessive bending. Another factor that likely contributes to the volume fraction- and site-dependent effect of microcavities is the relative difference between cavity size, which remains about the same, and typical trabecular morphology, which varies in low- versus high-density bone and across anatomic sites and species. This was supported by our finding that the effect of random cavities was slightly larger ($p<0.0001$) in the canine bone than the low-density human vertebral bone because the canine bone had thinner trabeculae (Tb.Th $p<0.0001$), even though the bone volume fraction was comparable to the high-density femoral neck bone.

In summary, our results suggest that if any stress riser effect exists due to resorption cavities in trabecular bone, that it is a relatively complicated effect that depends on a number of factors including species, anatomic site, bone volume fraction, and trabecular microarchitecture as well as the location of cavities within the tissue. However, whether or not stress risers play a role in fracture efficacy of antiresorptive treatments remains an enigma, and further research is recommended to address this interesting issue.

Table 2-1: Relationship between predicted strength and bone volume fraction for the three cavity-placement schemes per specimen.

	Canine vertebra (n=10)		*Human vertebra (n=16)*		*Human femoral neck (n=14)*	
	$S_y = m\,(BV/TV) + b$		$S_y = m\,(BV/TV) + b$		$S_y = m\,(BV/TV) + b$	
Cavity placement	*m*	*b*	*m*	*b*	*m*	*b*
None	117.1[a] (36.5)	-13.0 (8.3)	25.1[a] (6.8)	-0.97 (0.79)	100.9[a] (15.9)	-9.1 (3.7)
Random	107.8[a] (30.6)	-12.2 (6.5)	23.0[a] (6.1)	-0.89 (0.67)	92.6[a] (15.1)	-8.2 (3.3)
High-strain	92.8[a] (34.9)	-11.2 (7.5)	18.1[a] (5.9)	-0.77 (0.65)	81.7[a] (15.4)	-8.6 (3.4)

Data shows parameter estimate means (±95% CI). Strength has units of MPa. Multiple comparisons performed using the Bonferroni adjustment. *n* denotes the number of bone specimens per group; each specimen was analyzed assuming three different types of cavity placement.

[a] $p<0.01$ vs. both other cavity-placement schemes.

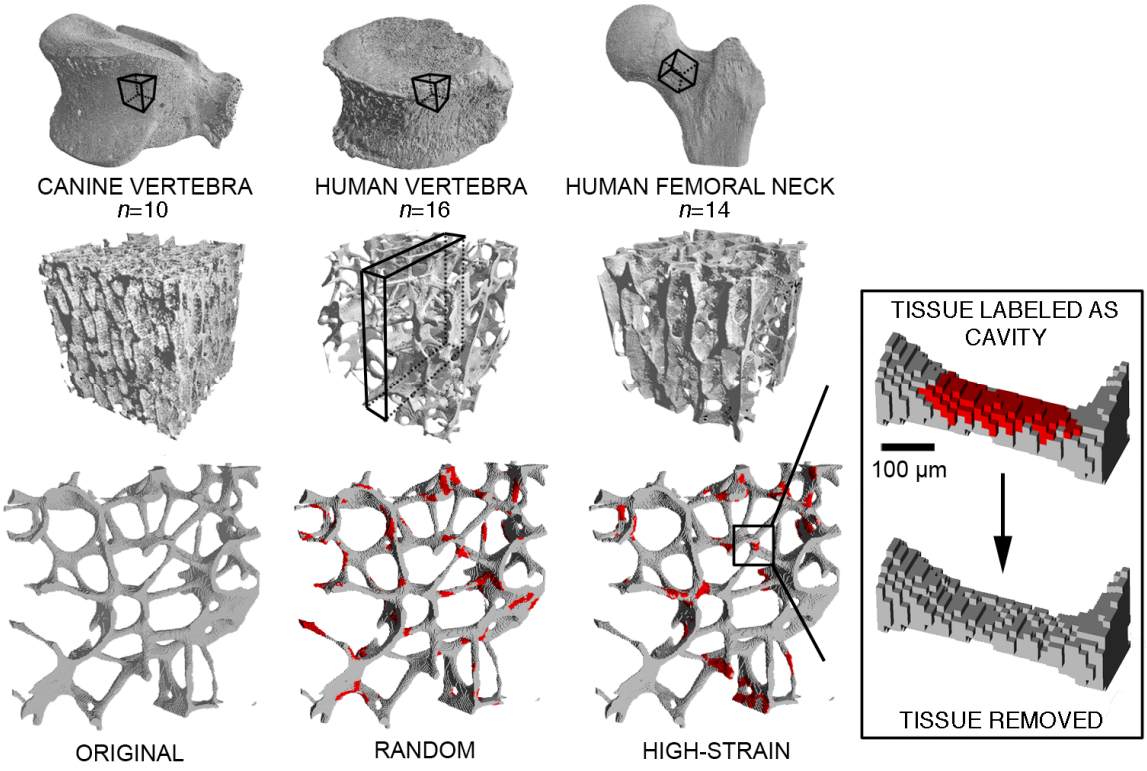

Figure 2-1: Micro-CT images of cubes of trabecular bone from canine vertebrae, human vertebrae, and human femoral necks were each converted into three finite element models containing simulated microcavities: 1) original model (no cavities added); 2) cavities distributed randomly; and 3) cavities targeted to regions of most highly-strained tissue.

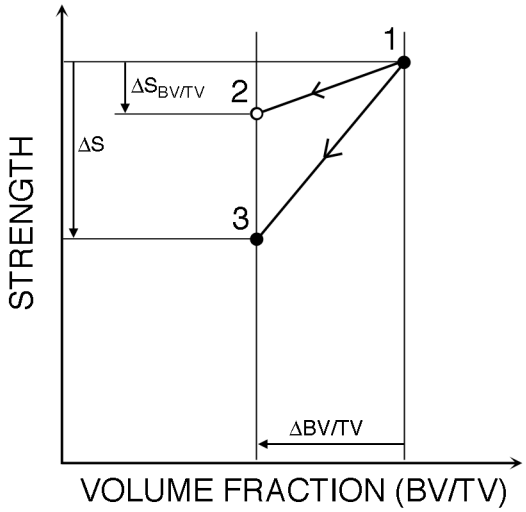

Figure 2-2: A normalized reduction in strength ($\Delta S/\Delta S_{BV/TV}$) was defined to quantify the effect of microcavities on strength beyond the effect of reduced volume fraction. First, the strength-volume fraction relationship (line 1-2) for each original model (point 1) was used to predict strength after a 6% reduction in volume fraction (point 2). Then the actual strength reduction computed for each cavity scheme (point 1 minus point 3) was normalized by this predicted strength reduction (point 1 minus point 2). A normalized strength reduction value of one indicates that the reduction is entirely due to the reduction in volume fraction, while a value greater than one indicates that there is some additional effect of the microcavities.

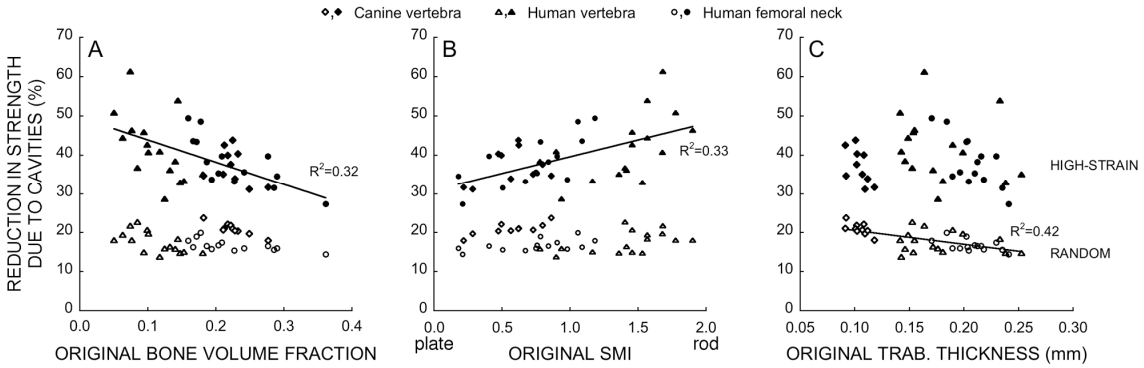

Figure 2-3: The percent reduction in yield strength associated with adding microcavities to trabecular bone, compared to the case without cavities, depended on bone volume fraction (A, $p<0.0001$, $n=40$) and SMI (B, $p<0.0001$) when microcavities were targeted to regions of highly-strained tissue but not when they were distributed randomly ($p>0.43$). When microcavities were distributed randomly, the percent reduction in yield strength associated with adding such cavities depended on mean trabecular thickness (C, $p<0.0001$).

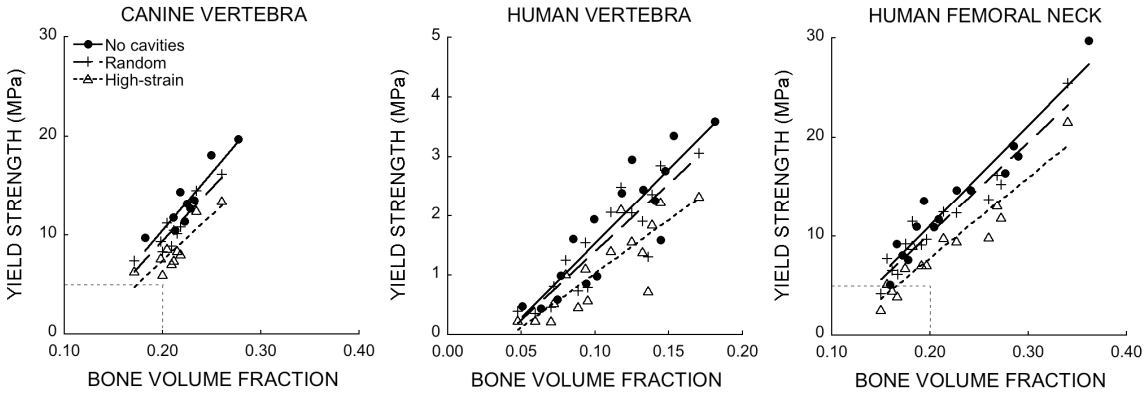

Figure 2-4: Strength-volume fraction relationships were altered by the addition of random and high-strain microcavities in trabecular bone from canine vertebrae, human vertebrae, and human femoral necks. All comparisons $p<0.001$. Dashed boxes in the left and right plots show the boundary of the center plot

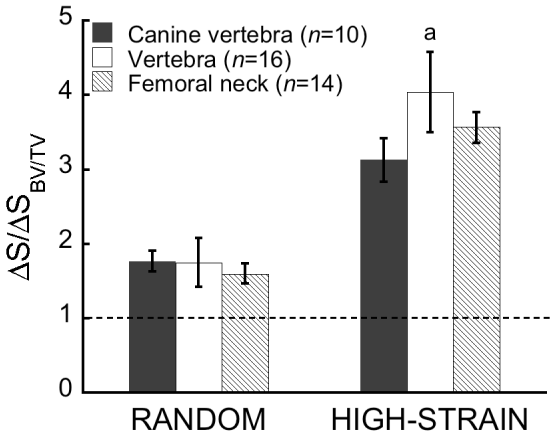

Figure 2-5: The reduction in strength after normalizing for the effect of the 6% decrease in volume fraction ($\Delta S/\Delta S_{BV/TV}$, see **Figure 2-2**) depended on anatomic site when microcavities were targeted to highly-strained tissue ([a] $p<0.05$ vs. canine vertebra) but not when they were distributed randomly. A value of one indicates the change in strength is due entirely to the change in volume fraction. Data given as mean ± 95% CI.

3. CONTRIBUTION OF THE INTRA-SPECIMEN VARIATIONS IN TISSUE MINERALIZATION TO THE PTH- AND RALOXIFENE-INDUCED CHANGES IN STIFFNESS OF RAT VERTEBRAE

3.1 Introduction

Whole-bone strength, a critical element of osteoporotic fracture risk, is determined by such factors as overall bone mass and 3D bone geometry, the cortical and trabecular microarchitecture, and the mechanical properties of the bone tissue. The mechanical properties of the bone tissue are influenced by the spatially non-uniform variations in mineralization within a bone [11, 13, 100, 131-134]. Such intra-specimen spatial variations in mineralization are the result of normal remodeling [135, 136] and can be altered by osteoporosis treatments [68, 75, 137, 138]. Since remodeling rates are generally greater in trabecular bone than in cortical bone [56], any treatment effects on the spatial variations in mineralization may also be greater in the trabecular bone. Understanding such treatment effects may have clinical significance if these effects account for an appreciable proportion of the overall treatment-induced changes in mechanical behavior at the whole-bone level.

Despite a number of studies that have addressed the role of the intra-specimen spatial variation in mineralization on the mechanical behavior of trabecular bone [100, 131-134], we are aware of no biomechanical studies that have addressed treatment effects. Addressing this issue, we sought in this study to determine how treatment-induced changes in the spatial variation in mineralization of rat vertebrae altered overall mechanical behavior of the vertebrae. We also sought to determine if the biomechanical role of treatment-induced changes in the spatial variation in mineralization was indeed greater for the trabecular compartment than for the whole vertebral body.

3.2 Methods

Study design

We used micro-CT imaging and micro-CT-based finite element analysis of excised L2 vertebrae from 40 rats that had been either sham-operated (n=10 rats) or ovariectomized, the latter treated with either vehicle, parathyroid hormone (PTH) or raloxifene (n=10 rats per group). The micro-CT imaging, at 6 micron voxel size, was used to characterize the intra-specimen spatial variation in mineralization (**Appendix 7.2**) and the micro-CT-based finite element modeling, also at 6 micron voxel size, was used to characterize mechanical behavior. Since the anabolic agent PTH stimulates bone remodeling and increases the percentage of newly formed bone with lower mineral density [75], this treatment was anticipated to increase the heterogeneity of the tissue mineralization. Conversely, since the selective estrogen receptor modulator raloxifene suppresses bone remodeling, it was anticipated to increase the mean mineralization and decrease the heterogeneity of mineralization [139]. Compared to other antiresorptives, raloxifene was chosen because it was found in a dog study to increase strength more than

it increased areal BMD [140], which may have resulted from alterations to the tissue mineralization (among other factors).

A critical component of the study design was its ability to separate any biomechanical effects associated with treatment-induced changes in the spatial variation in mineralization — *i.e.* the intra-specimen variation in mineral density at the 5–10 micron scale as measured by micro-CT — from those effects associated with changes in the mean degree of mineralization or whole-bone geometry or microstructure. Since separating out such effects using a traditional statistical analysis of results from biomechanical testing of excised animal bones would require a prohibitively large sample size, we instead relied on virtual biomechanical testing based on finite element analysis of the micro-CT scans. The use of a relatively small sample size (40 rats total) was made possible by our ability to vary the finite element model of each vertebra in a systematic way in order to either virtually include or exclude the micro-CT-observed spatial variation in mineralization (**Figure 3-1**). This strategy resulted in multiple, repeated measures of overall bone stiffness for each bone analyzed in which the only difference between the repeated measures was the presence or absence of the micro-CT-observed mineral variations.

To separate out spatial variation versus mean mineralization effects, we considered three virtually-altered mineralization cases per vertebra: 1) spatially varying mineralization throughout the bone as measured directly with the quantitative micro-CT; 2) homogeneous mineralization assigned to all bone tissue in a given vertebra, using the specimen-specific mean value of mineralization determined from the quantitative micro-CT analysis for that vertebra; and 3) homogeneous mineralization using a constant reference mineralization value for all bone tissue in all vertebrae (**Figure 3-1**). To determine if the contribution of mineralization to treatment-induced changes in stiffness differed in the trabecular compartment compared to the whole vertebral body, these three mineralization cases were evaluated for both the whole vertebral body and the virtually isolated trabecular compartment (**Figure 3-1**). This resulted in six simulations for each of the 40 vertebral specimens (240 simulations total). All micro-CT and finite element analyses were performed blinded to treatment code.

Animals and treatments

The 40 female Sprague Dawley rats were sham-operated (n=10) or ovariectomized (OVX, n=30) at 16 weeks of age. After surgery, all rats were left untreated for eight weeks to allow any OVX-induced bone loss to occur. For eight weeks thereafter, the sham group was treated with vehicle (placebo) and the OVX groups were treated with either vehicle (n=10), hPTH(l-34) (n=10, 40 μg/kg by subcutaneous injection 5 days/week), or raloxifene (n=10, 3 mg/kg by oral gavage 5 days/week). The treatment dosages administered for PTH and raloxifene were selected based on optimal efficacy demonstrated in previous OVX rat model studies for osteopenic restoration [141] and osteopenic prevention [142], respectively. All animals were sacrificed at 32 weeks.

Specimen preparation

After sacrifice, the L2 vertebra was excised from each animal and the discs and soft tissue were removed. To isolate the vertebral bodies and facilitate virtual compression testing, the posterior elements and endplates were also removed, following common protocols used in experimental and finite element preclinical studies [55, 140, 143-146]. First, the posterior elements were removed with bone clippers. Then, the caudal end of each isolated vertebral body was embedded in epoxy and mounted in a custom holder of a diamond blade precision saw (IsoMet 1000, Buehler, Lake Bluff, IL, USA). Cranial and caudal endplates were removed by cutting segments of approximately 1 mm from both ends of the vertebral bodies, producing specimens with heights of 3.8 ± 0.4 mm (mean ± SD) and plano-parallel end surfaces.

Quantitative micro-CT imaging

All specimens were imaged with quantitative micro-CT (μCT 40, Scanco Medical AG, Brüttisellen, Switzerland) to non-destructively measure tissue mineral density and characterize cortical and trabecular microstructure. Imaging was done using a 55 kVp source potential and 145 mA current. Projection images were reconstructed across a 2048*x*2048 matrix spanning a 12.3 mm field-of-view, resulting in an isotropic voxel size of 6 microns. Attenuation values were converted to hydroxyapatite (HA) density using a calibrated linear relationship and beam hardening correction algorithms, based on a HA-resin wedge phantom of 200 mg HA/cm^3, that minimize the influence of specimen geometry on reconstructed linear attenuation values. Details of the calibration process and its validation have been reported previously [97, 98].

The reconstructed 3D grayscale images of the vertebra were masked to remove the background from the bone (IPL v5.01c-ucsf, Scanco Medical AG). The mask was a binary image of the bone generated using a fixed thresholding scheme [97] where the cortical and trabecular threshold values were determined manually as those that produced the best delineation of bone surfaces and voids when visually compared to the original images. These masked grayscale images were used to calculate mineralization parameters for each vertebra, specifically, the mean mineral density and the coefficient of variation of mineral density. The coefficient of variation of mineral density provides an indication of heterogeneity and was defined as the standard deviation of mineral density within a vertebra normalized by its mean. To calculate these mineralization parameters, the outer two voxel layers (about 15% of the total bone volume) were temporarily eroded from the bone surfaces (IDL v6.2, ITT) to minimize any effects of volume averaging. Using the original binary images, the manufacturer's software was used to compute various microstructural indices: cortical thickness (Ct.Th), trabecular bone volume fraction (BV/TV), bone surface-to-volume ratio (BS/BV), trabecular number (Tb.N), trabecular separation (Tb.Sp), trabecular thickness (Tb.Th), connectivity density (Conn.D), degree of anisotropy (DA), and structure model index (SMI).

Finite element analyses

As noted above, six high-resolution finite element models were generated per vertebra to separate the contributions of the intra-specimen spatial variation in mineralization, mean mineralization, and geometry and microstructure to the stiffness of the whole vertebral body and the trabecular compartment (**Figure 3-1**). Finite element models were constructed from each micro-CT scan using 6-micron-sided cube-shaped elements. The models had from 28-71 million elements, reflecting the large variation in overall bone mass that resulted after the various treatments. The cortical and trabecular compartments were identified by manually tracing the endosteal surface of the cortex in every 40 slices (0.24 mm) of each scan and then extrapolating between the slices using the manufacturer's software (IPL v5.01c-ucsf, Scanco Medical AG).

We considered three cases of mineralization for each whole vertebral body and its trabecular compartment, for which the cortex had been digitally removed. In the first case, we applied the voxel-specific mineral density directly obtained from the quantitative micro-CT scan to each element in each vertebra to calculate stiffness K. This stiffness measure includes all effects of mineral density variations within and across specimens. In the second case, we applied the specimen-specific mean mineral density uniformly to all elements in each vertebra to calculate stiffness K_{MEAN}. This stiffness measure includes effects of only the mean mineral density across specimens and did not include any intra-specimen variation in mineralization. In the third case, we applied a reference mineral density — chosen to be the average mineral density of all specimens (1133 mg HA/cm^3, n=40 rat vertebrae) — uniformly to all elements in all vertebrae to calculate stiffness K_{REF}. This stiffness measure does not include effects of differences in either the spatial variation in mineralization within a specimen or the mean mineralization across specimens. By eliminating such effects, it accounts for how overall vertebral stiffness is influenced only by the geometry and microstructure of the bone, *e.g*. cortical morphology and trabecular microarchitecture.

High-resolution, linearly elastic, finite element analysis was used to simulate a uniform compression test. Each element was assigned a Young's modulus based on its mineral density, using a power-law relationship, as previously suggested [36], between mineral density and tissue modulus from a fit to a compilation of data from the literature [147-152] (**Figure 3-2**)

$$E_{tissue} = 1.127 \cdot 10^{-4} TMD^{1.746}$$

in which tissue modulus (E_{tissue}) is in GPa and tissue mineral density (TMD) is in mg HA/cm^3. All elements were assigned a Poisson's ratio of 0.3. Uniaxial compression loading was applied with the cranial and caudal end surfaces fixed in-plane. The overall stiffness was calculated as the ratio of the total reaction force at the inferior surface to the applied displacement. Stiffness was computed in this way for each of the six models per bone for all 40 bones.

Contribution of Intra-Specimen Variation in Mineralization to Treatment-Induced Changes in Stiffness

To quantify the contribution of the intra-specimen mineral variations to treatment-induced changes in stiffness, we defined additional outcomes based on our primary measures of bone stiffness. To adjust for the effects of geometry and microstructure, we computed a first normalized stiffness K/K_{REF}. To adjust for the effects of the mean degree of mineralization in addition to geometry and microstructure, we computed a second normalized stiffness K/K_{MEAN}. These adjustments were made for both the whole vertebra and trabecular compartment models.

Statistical analysis

Following finite element analysis, the data were unblinded. To determine the effect of treatment on the various outcomes, we used a one-factor ANOVA with Dunnett's *post hoc* test. Despite the small sample size per group, parametric tests were used because the data did not violate the normality assumption ($p>0.09$, Shapiro-Wilk test). The independent associations between the contribution of the intra-specimen mineral variations to stiffness and mean mineralization, coefficient of variation of mineralization, cortical thickness, and trabecular microarchitecture were quantified by the Pearson correlation coefficient. All statistical analyses were done using JMP (Version 7.0, SAS Institute Inc., Cary, NC). For all tests, $p<0.05$ was considered statistically significant.

3.3 Results

As expected, ovariectomy and treatments had an appreciable effect on overall stiffness, as estimated by the finite element analyses (**Figure 3-3**). For example, compared to sham, the stiffness of the trabecular compartment was reduced by 52% ($p<0.0001$) and 40% ($p=0.001$) in the OVX and raloxifene groups, respectively, but was unchanged for the PTH group ($p=0.063$). The treatment effects on stiffness were relatively larger for the trabecular compartment than for the whole vertebral body, just missing statistical significance for the latter ($p=0.055$). The OVX surgery itself reduced overall bone mass, trabecular bone volume fraction, and trabecular number and resulted in a more rod-like structure (**Table 3-1**). Unlike treatment with raloxifene, treatment with PTH after OVX restored bone mass and bone volume fraction to sham levels and thickened remaining trabeculae. Cortical thickness was not altered by any treatment.

Although the analysis of the quantitative micro-CT data revealed small but significant effects of treatment on the intra-specimen spatial variation in mineral density (**Table 3-2**), the finite element analyses indicated that these treatment-induced changes in mineral variations had a negligible biomechanical role in terms of treatment-induced changes in stiffness (**Figure 3-4**). The coefficient of variation in mineral density only varied from 10.8–11.2% in the whole vertebral body ($p=0.004$ overall treatment effect) and from 11.1–11.6% in the trabecular compartment ($p=0.02$ overall treatment effect), and the mean mineral density was unchanged across groups ($p>0.13$). After adjusting in a specimen-specific manner for the treatment-induced changes in geometry and microstructure by calculation of the K/K_{REF} parameter, there were no treatment effects on normalized stiffness for either the whole vertebra ($p=0.23$, **Figure 3-4 A**) or the

trabecular compartment (p=0.15, **Figure 3-4 B**). After additionally adjusting for any changes in intra-specimen mean mineralization by calculation of the K/K_{MEAN} parameter, statistically significant effects on normalized stiffness were detected (p<0.02) — but these effects were on the order of only 1–2%. These tiny effects were statistically detectable because of the very tight confidence intervals for the mean measures of normalized stiffness for each treatment group. The confidence intervals were so small because the stiffness measures obtained for each of the variant finite element models (K, K_{MEAN}, K_{REF}) were very highly correlated with each other (r^2>0.99). These high correlations indicate that the biomechanical role of the intra-specimen mineral variations was almost constant across specimens for any given treatment.

Comparison of the stiffness measures obtained for each of the variant finite element models (K, K_{MEAN}, K_{REF}) with each other also revealed that the intra-specimen spatial variations in mineralization accounted for up to about 12% of the overall stiffness of the bone (**Table 3-3**). As noted above, this contribution depended on treatment in a statistically significant but minor way, but this contribution was about two-fold greater in the trabecular compartment than in the whole vertebra. Removing the spatial variations in mineralization from the finite element models always resulted in higher bone stiffness than in either of the homogenized mineralization models, *i.e.* K was always higher than either K_{MEAN} or K_{REF}. Correlation analysis indicated that the size of this effect increased with decreasing coefficient of variation in mineralization, cortical thickness, and various measures of trabecular microarchitecture, most notably the trabecular thickness (Tb.Th), and increased with increasing bone-surface-to-bone-volume ratio (BS/BV; **Table 3-4**).

3.4 Discussion

These results demonstrate that any treatment-induced changes in the intra-specimen spatial variations in mineral density — at the 5–10 micron scale as detected by quantitative micro-CT — had a negligible biomechanical effect in these rat vertebrae at the whole bone level and in the isolated trabecular compartment. While the biomechanical role of the mineral distribution reduces overall stiffness compared to what it would be if such intra-specimen variations did not exist, that role was remarkably uniform across specimens within any treatment group and was only altered by treatment in a minor way. At least for the rats studied here, all biomechanical treatment effects as estimated by the finite element modeling were dominated by the treatment-induced changes in trabecular microstructure and were negligibly influenced by the subtle changes in intra-specimen mineral variations.

Despite the minor role of intra-specimen mineral variations observed here, our results do signal an advance in terms of quantitatively assessing the biomechanical role of intra-specimen mineral variations for other treatments or disease states. One unexpected finding was our ability to detect the very small (<2%) treatment effects on the biomechanical role of intra-specimen mineral variations on overall bone stiffness. This was due to two factors. The first was the nearly constant biomechanical role of intra-specimen mineral variations that we observed within each group. This was manifested by the very narrow confidence intervals in the normalized stiffness data and the high

correlations between K, K_{MEAN} and K_{REF}. The second factor was the highly sensitive repeated-measures study design, in which the finite element models were varied in a systematic manner for each specimen. That study design enabled us to normalize the overall stiffness outcome, on a specimen-specific basis, for effects of bone geometry, microstructure, and even mean mineralization. Because of both these factors, this study design could be useful in evaluating or detecting disease states in which large changes in the mineral distribution can occur, for example with osteomalacia [153]. In such disease states, the ratio of K/K_{MEAN} or K/K_{REF} may differ substantially from that observed in this study, or, the correlations between K, K_{MEAN} and K_{REF} may be relatively weak.

From a biomechanical computational modeling perspective, the results of this study suggest that, under some conditions, it may be important to include the intra-specimen variations in mineral density in finite element analyses of bone. Most high-resolution micro-CT-based finite element studies of human cadaver and animal bone assume a pre-assigned homogeneous bone tissue modulus, such as in our K_{REF} models. Homogeneous finite element models which exclude the mineral variations overestimate mechanical behavior of bone; this finding was consistent with previous work on cubes of trabecular bone [100, 132-134]. The amount by which homogeneous models overestimated mechanical properties was relatively constant in these rats, even across treatment groups. If this trend persists in human bone and for other treatments, then the assumption of tissue homogeneity would have little impact on conclusions from studies that make relative comparisons of finite element outcomes. However, this assumption may have a less trivial effect on studies in which absolute magnitudes of the finite element predictions are important. For example, effective properties of bone tissue that are determined by calibrating finite element predictions with experiments [104, 109] may be slightly underestimated by neglecting the mineral variations within a bone.

While we used treatments that spanned the range of possible tissue mineralization and microarchitecture phenotypes of most current anti-fracture treatments, our results do not apply directly to human studies. The various treatments explored here did produce statistically significant differences in the coefficient of variation in mineral density that were consistent with the literature [75, 139]. Bone mass and microarchitecture were also appreciably different across the groups. The large reduction (~30%) in bone volume fraction in the OVX group was consistent with findings from other studies in which rats were young — 4 months old in this current study — at the time of ovariectomy [144, 154, 155]. However, it is difficult to determine the clinical relevance of the dosages administered, which were higher than approved for human clinical use, because of differences in pharmacokinetics, pharmocodynamics, and metabolism in rats versus humans. Further, it is not clear if the effects of treatment on the biomechanical role of intra-specimen mineral variations would differ in elderly human trabecular bone, which generally has a much lower bone volume fraction than the bone in this study, and which may have different spatial variations in mineralization. Extension of the techniques used in this study to human biopsies represents an interesting future study.

One technical caveat of this study is that we used linear elastic finite element analyses which enabled us to compute stiffness, but not strength, as an outcome. For finite element analysis of bone, estimates of stiffness and strength are both highly correlated with experimentally measured values of strength [34, 95, 108]. Thus it is

unlikely that we would have reached any different conclusions had we performed the much more computationally expensive nonlinear modeling for estimation of strength. That said, it is possible that the actual strength of treated bone may be affected differently than any finite element-calculated strength value if small-scale effects not included in the micro-CT scans or our finite element models actually play an appreciable role in treatment-induced changes in strength. Such effects might include mineral crystal characteristics, collagen cross-linking, micro-damage accumulation, or stress-risers associated with the remodeling space [11, 13, 90, 156, 157]. While none of these effects have yet been shown to have any appreciable influence on treatment-induced changes of strength in any animal models [15], these factors may have more relevance in elderly human bone and thus this unresolved issue remains an area of ongoing research.

Another technical issue is that the relationship between elastic modulus and bone mineral density at the voxel level has not been well established, requiring us to make assumptions regarding its nature. Rather than use any single relation from the literature, our approach was to use one based on a compilation of all available literature studies. Although there was appreciable scatter for that assumed relationship (R^2=0.48), our preliminary work found that the use of linear versus nonlinear (up to third order power law, **Figure 3-2**) modulus-density relationships in one specimen altered vertebral stiffness by less than 10%. This modest level of sensitivity to the assumed relationship, and our finding that the biomechanical treatment effects for intra-specimen mineral variations were so small, suggests that use of an alternate relationship between density and modulus at the voxel level would not have altered our main findings.

We also emphasize that our model effects here were based on mineral measurements taken using micro-CT, and thus there are inherent resolution issues that should be considered when interpreting our results. First, because the voxel size of the micro-CT scans was 6 microns, the resulting mineralization measurements do not reflect any possible treatment-induced changes at smaller scales or to the mineral crystals themselves [156-158]. Second, measurements of mineral density at the bone surfaces are confounded by volume averaging and beam hardening artifacts [97, 98, 159-163]. To mitigate these artifacts, we used beam hardening correction algorithms known to appreciably improve the accuracy of micro-CT measurements of mineral density [98, 161] and we excluded the outer two layers of voxels affected by volume averaging in the calculations of mineralization parameters. Micro-CT measurements of mineral density using such corrections have been shown to be underestimated but are well correlated with synchrotron radiation micro-CT and measured ash densities, particularly for specimens of similar geometries [97, 162], as in this study. Any remaining beam hardening artifacts are expected to occur randomly, and thus should not impact relative comparisons between treatment groups. The effect of volume averaging depends on the amount of newly formed bone present in the surface voxels, and could result in underestimates of group differences in mineralization parameters and overestimates of the contribution of the intra-specimen mineral variations to stiffness. Higher resolution studies are required to confirm such bias did not exist in this study, although given the small treatment effects observed, it is unlikely that any such bias would have an appreciable biomechanical effect.

In summary, despite a role in the general biomechanical behavior of bone, the intra-specimen spatial variations in tissue mineralization, as measured by quantitative micro-CT, did not appreciably contribute to ovariectomy-, PTH-, or raloxifene-induced changes in stiffness of the whole bone or the trabecular compartment in these rat vertebrae.

Table 3-1: Effect of treatments on mass, cortical thickness, and trabecular microarchitecture.

Measure	*Sham + Vehicle*	*OVX + Vehicle*	*OVX + PTH*	*OVX + Raloxifene*
Mass (mg/mm)	7.1 ± 1.1^{b}	5.7 ± 1.1^{a}	6.6 ± 0.7	5.6 ± 1.3^{a}
Ct.Th (mm)	0.24 ± 0.02	0.22 ± 0.03	0.23 ± 0.02	0.22 ± 0.03
BV/TV	0.31 ± 0.04^{b}	0.21 ± 0.04^{a}	0.29 ± 0.06^{b}	0.24 ± 0.04^{a}
BS/BV	0.32 ± 0.03^{b}	0.35 ± 0.03^{a}	$0.28 \pm 0.03^{a,b}$	0.33 ± 0.03
Tb.N (mm^{-1})	4.18 ± 0.35^{b}	3.07 ± 0.46^{a}	3.43 ± 0.45^{a}	3.30 ± 0.37^{a}
Tb.Sp (mm)	0.24 ± 0.02^{b}	0.33 ± 0.06^{a}	0.31 ± 0.05^{a}	0.31 ± 0.03^{a}
Tb.Th (mm)	0.078 ± 0.006	0.075 ± 0.006	$0.097 \pm 0.011^{a,b}$	0.077 ± 0.005
DA	1.77 ± 0.06	1.82 ± 0.07	1.80 ± 0.10	1.81 ± 0.07
Conn.D (mm^{-3})	108 ± 21^{b}	85 ± 22^{a}	93 ± 22	75 ± 14^{a}
SMI	0.05 ± 0.32^{b}	0.93 ± 0.17^{a}	0.63 ± 0.41^{a}	0.64 ± 0.37^{a}

Data are means ± SD for 10 rats per treatment group.
[a] $p < 0.05$ vs. sham + vehicle.
[b] $p < 0.05$ vs. OVX + vehicle.

Table 3-2: Effect of treatments on the mean mineral density and the coefficient of variation in mineral density.

Mineralization	*Sham + Vehicle*	*OVX + Vehicle*	*OVX + PTH*	*OVX + Raloxifene*
Whole Vertebra				
Mean mineral density (mg HA/cm^3)	1134 ± 10	1141 ± 9	1140 ± 12	1145 ± 11
CV in mineral density (%)	11.2 ± 0.3^{b}	10.8 ± 0.3^{a}	11.2 ± 0.3^{b}	10.9 ± 0.3^{a}
Trabecular Compartment				
Mean mineral density (mg HA/cm^3)	1081 ± 11	1084 ± 10	1084 ± 13	1089 ± 8
CV in mineral density (%)	11.6 ± 0.4^{b}	11.1 ± 0.4^{a}	11.6 ± 0.4^{b}	11.2 ± 0.4

Data are means ± SD for 10 rats per treatment group. Mineralization parameters measured from quantitative micro-CT scans with two voxel layers removed from the surfaces. CV: coefficient of variation (SD/mean, in %) of the mineral density within a specimen.
[a] $p < 0.05$ vs. sham + vehicle.
[b] $p < 0.05$ vs. OVX + vehicle.

Table 3-3: Effect of treatments on the contribution of the intra-specimen mineral variations to stiffness.

	Sham + Vehicle	*OVX + Vehicle*	*OVX + PTH*	*OVX + Raloxifene*
Whole Vertebra				
Contribution to *K* (%)	-5.4 ± 0.6	-6.0 ± 0.8	-5.2 ± 0.6 [b]	-5.6 ± 0.3
Trabecular Compartment				
Contribution to *K* (%)	-10.9 ± 0.7 [b]	-11.9 ± 0.8 [a]	-9.8 ± 1.1 [a,b]	-11.0 ± 0.8

Data are means ± SD for 10 rats per treatment group. Negative sign indicates that stiffness decreases when the intra-specimen mineral variations are included. The contribution of the intra-specimen variation in mineralization to stiffness was defined as the percent change in stiffness when only the mean mineralization was included compared to when the intra-specimen variation in mineralization was included in the model.
[a] $p < 0.05$ vs. sham + vehicle.
[b] $p < 0.05$ vs. OVX + vehicle.

Table 3-4: Independent correlations (r) between the contribution of intra-specimen mineral variations to stiffness and the mineralization and microstructural parameters.

	Mean mineral[c]	CV in mineral[c]	Ct.Th	BV/TV	BS/BV	Tb.N	Tb.Sp	Tb.Th	SMI
Whole Vertebra									
K/K_{MEAN}	-0.01	-0.48[b]	-0.50[b]	-0.33[a]	0.45[b]	-0.22	0.18	-0.43[b]	0.15
Trabecular Compartment									
K/K_{MEAN}	-0.19	-0.40[b]	-0.16	-0.59[b]	0.77[b]	-0.31[a]	0.30	-0.71[b]	0.28

Values are Pearson's correlation coefficient (r) for 40 rats, all treatment groups pooled. CV: coefficient of variation (SD/mean) of the mineral density within a specimen.
[a] $p < 0.05$.
[b] $p < 0.01$.
[c] measures made separately for the whole vertebra and the trabecular compartment.

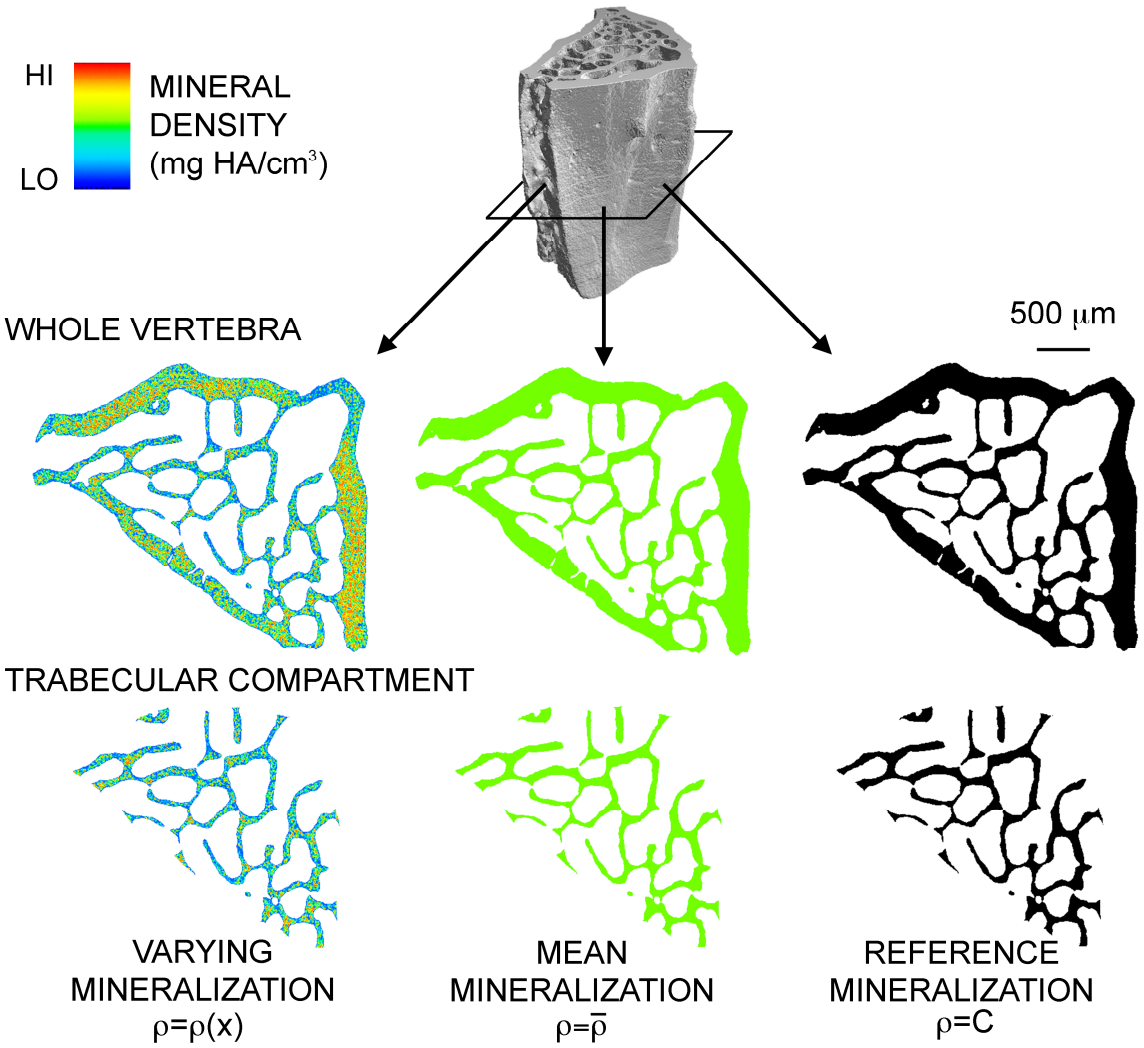

Figure 3-1: Each micro-CT scan was used to generate six finite element models per rat vertebra: three mineralization cases for the whole vertebral body and three for its isolated trabecular compartment. The first case included the spatial variation in mineral density within a specimen measured directly from the micro-CT scan. The second case included only the mean mineral density measured for that specimen. The third case included a constant reference mineral density for all specimens. This was done for 40 vertebrae from 40 treated rats (10 rats per group). Transverse sections are shown.

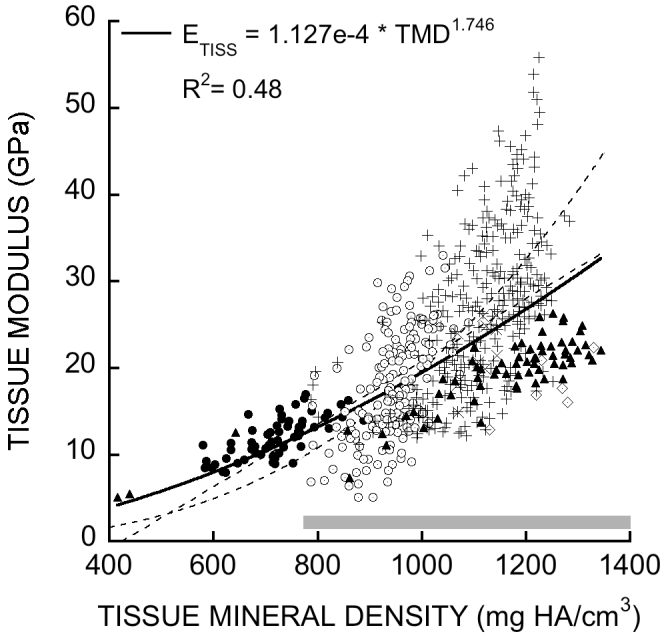

Figure 3-2: A relationship between bone tissue elastic modulus (E_{TISS}) and tissue mineral density (TMD) was fitted to a compilation of data from studies encompassing a range of species, anatomic sites and techniques for measuring modulus and mineral density: (●) nanoindentation and micro-CT of sagittal sections from 8 porcine mandibular condyles [152]; (○) tensile tests and colorimetric measures of calcium concentration of 249 cortical specimens from 22 various species [149]; (▲) compression tests and QCT density of 80 cortical specimens from 9 human femora [148]; (×,◇) scanning acoustic microscopy and synchrotron micro-CT of transverse sections from 10 human radii [150] and 10 murine femora [151]; and (+) tensile tests and ash content of 10 cortical specimens from bovine tibia and femora [147]. The horizontal bar shows the typical range of densities in these vertebrae. The dashed lines show alternate modulus-density relationships considered in a sensitivity study.

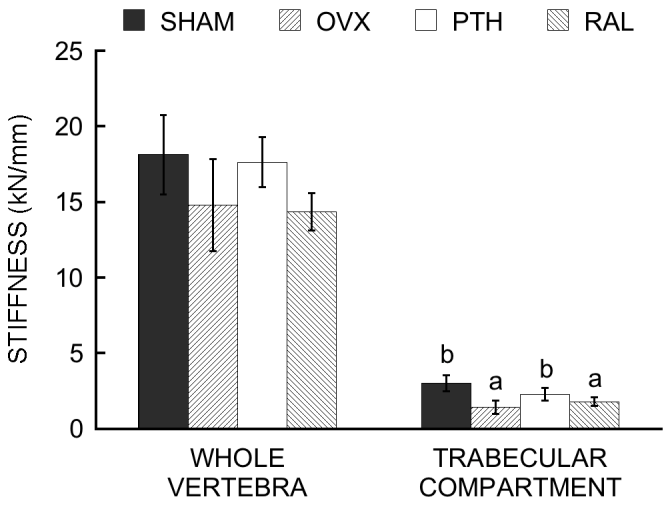

Figure 3-3: Effect of treatment on finite element-predicted stiffness of the whole vertebral body and trabecular compartment. Bars show mean ± 95% confidence intervals for 10 rats per group. [a] $p < 0.05$ vs. sham + vehicle, [b] $p < 0.05$ vs. OVX + vehicle.

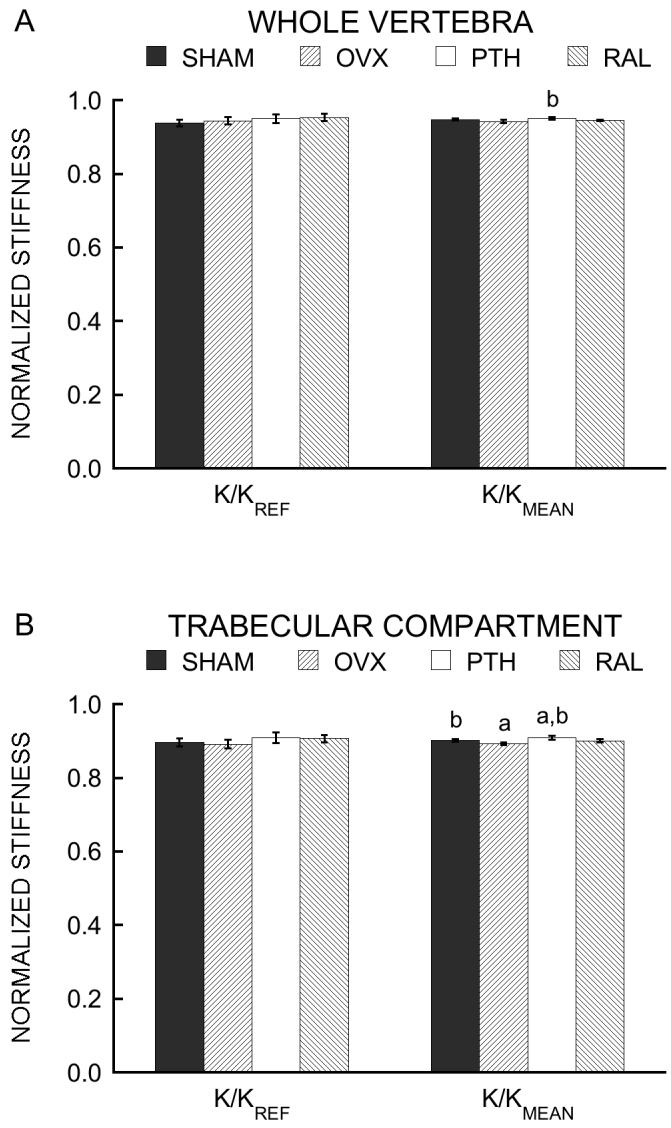

Figure 3-4: Effect of treatment on stiffness of the whole vertebral body (A) and trabecular compartment (B) after adjusting for only geometry and microstructure (K/K_{REF}) and geometry and microstructure and the specimen-specific mean mineral density (K/K_{MEAN}). Bars show mean ± 95% confidence intervals for 10 rats per group. [a] $p < 0.05$ vs. sham + vehicle, [b] $p < 0.05$ vs. OVX + vehicle.

4. BIOMECHANICAL CHARACTERIZATION OF BONE QUALITY

4.1 Introduction

Bone quality is defined as the characteristics of a bone that influence biomechanical behavior and resistance to fracture, but are not accounted for with measures of bone quantity or density [12, 15, 18]. Since increases in clinical measures of areal bone mineral density (BMD) do not adequately explain reductions in osteoporotic fracture incidence with drug treatment [8-10], much interest has been generated in understanding the effects of treatments on biomechanical bone quality characteristics to better evaluate treatment efficacy [11-17]. A number of structural and material characteristics at hierarchical physical scales — from the whole bone level to the molecular level — have been suggested as potentially important components of biomechanical bone quality [11-17]. Currently, the typical approach used in pre-clinical studies is to focus on evaluating treatment effects on a limited number of bone quality characteristics [83, 91, 121, 146, 164]. However, changes at a smaller scale do not necessarily translate to changes at a larger scale, so by measuring bone quality characteristics in relative isolation from other characteristics, potentially important treatment effects on bone quality may be missed. Thus, there remains a need for a systematic approach to integrating treatment effects at all scales into a clinically relevant characterization of biomechanical bone quality. To address this need, we present an approach that combines experimental and computational techniques to characterize structural and material bone quality — including strength-density relationships, the strength-to-stiffness ratio, cortical thickness and trabecular microarchitecture, the contribution of the cortical and trabecular compartments to whole bone biomechanical behavior, and elastic modulus of the bone tissue — and the associated effects on biomechanical behavior of human or animal bone.

4.2 Methods

Overview of approach

Herein we present a framework for integrating disease- and treatment-induced effects at all hierarchical scales into a clinically-relevant characterization of biomechanical bone quality. We applied this approach to excised L2 vertebrae from 30 rats that had been sham-operated or ovariectomized, the latter treated with either vehicle or PTH (n=10/group), to test its effectiveness.

This approach combines experimental and computational techniques. First, each bone is micro-CT imaged at high resolution — on the order of 5-20 microns — to measure cortical thickness and trabecular microarchitecture and provide geometry for subsequent finite element modeling. Then, vertebral strength and stiffness is measured during biomechanical compression tests following protocols (**Appendices 7.3 and 7.4**) designed to minimize the effects of machine compliance and other testing artifacts [165]. Micro-CT-based finite element analysis of the same bones that were imaged and tested are used to predict vertebral stiffness and then the elastic modulus of the bone tissue is

calibrated for each specimen such that the finite element-predicted stiffness matches the measured stiffness [109]. Finally, two additional finite element analyses per bone — the isolated cortex and the isolated trabecular compartment — are performed to determine the contribution of each of these compartments to mechanical behavior of the whole bone. Relationships between strength and bone mass or density is used to evaluate net effects on bone quality [15]; the subsequent analyses are used to isolate the source of any net effects.

We compared the various outcomes across the three groups of rat vertebrae to determine the effects of OVX and PTH on biomechanical bone quality. We also performed a statistical power analysis to guide future use of this approach.

Animals and treatments

The 30 female Sprague Dawley rats were sham-operated (n=10) or ovariectomized (OVX, n=20) at 16 weeks of age. After surgery, all rats were left untreated for eight weeks to allow OVX-induced bone loss to occur. For 12 weeks thereafter, the sham group was treated with vehicle (placebo) and the OVX groups were treated with either vehicle (n=10) or hPTH(l-34) (n=10, 20 μg/kg by subcutaneous injection 5 days/week). The treatment dosage administered for PTH was selected based on optimal efficacy demonstrated in a previous OVX rat model study for osteopenic restoration [141]. Animals were sacrificed at 36 weeks. All experiments and analyses were performed blinded to treatment code.

Specimen preparation

After sacrifice, the L2 vertebra was excised from each animal and prepared for subsequent analysis. Since the precision of subsequent calculations of effective tissue modulus depend on the precision of the measurements of vertebral stiffness — a measure that is particularly sensitive to any misalignments or compliance in the biomechanical testing set-up — it was critical to prepare the specimens such that they were uniform and had plano-parallel ends. After removing the discs and soft tissue, the posterior elements and endplates were removed, following a specialized protocol, similar to those used in other experimental and finite element preclinical studies [55, 140, 143-146]. Specifically, the posterior elements were embedded in bone cement (polymethylmethacrylate) and this cement block was used to mount the vertebra in a custom holder of a diamond blade precision saw (IsoMet 1000, Buehler, Lake Bluff, IL, USA). Cranial and caudal endplates were removed such that the mid-50% of the original height remained. Then, the posterior elements were cut with bone clippers, isolating vertebral body specimens with heights of 3.7 ± 0.2 mm (mean ± SD) and plano-parallel end surfaces.

Micro-CT imaging

All prepared specimens were imaged using quantitative micro-CT (μCT 40, Scanco Medical AG, Brüttisellen, Switzerland) at an isotropic voxel size of 6 microns to characterize cortical and trabecular microstructure and to create image datasets for subsequent finite element analysis. To segment bone tissue from marrow space, each image was binarized using a fixed thresholding scheme [97] where the cortical and trabecular threshold values were determined manually as those that produced the best delineation of bone surfaces and voids when visually compared to the original images. Using these binary images, the manufacturer's software was used to compute various microstructural indices: cortical thickness (Ct.Th), trabecular bone volume fraction (BV/TV), trabecular number (Tb.N), trabecular separation (Tb.Sp), trabecular thickness (Tb.Th), structure model index (SMI), connectivity density (Conn.D), and degree of anisotropy (DA). Bone mineral content (BMC) was estimated based on the bone volume as measured from the images and assuming a constant tissue density of 2.05 g/cm^3 [166].

Biomechanical testing

After imaging, uniaxial compression tests were conducted using a servohydraulic load frame (858 Mini-Bionix, MTS, Eden Prairie, MN) to measure strength, stiffness, and the strength-to-stiffness ratio. Each vertebral body was compressed between platens that had been lubricated so that boundary conditions could be more accurately reproduced in the subsequent finite element analyses. To minimized any effects of machine compliance, apparent strain was measured using a 25 mm gage length extensometer (632.11F-20, MTS, Eden Prairie, MN) attached directly to the platens. Tests included 5 preconditioning cycles to 0.3% strain followed by a final ramp to 8% strain at a rate of 0.5% strain/sec. To further reduce any testing artifacts that might introduce artifactual compliance, stiffness was defined as the maximum slope of the force-displacement curve; strength was defined as the maximum force sustained during the test. The strength-to-stiffness ratio was subsequently calculated to quantify any treatment effects that altered strength beyond any effects on stiffness.

Tissue modulus calculations

These experimental data were used in combination with finite element analysis to estimate the elastic modulus of the bone tissue for each vertebra [104, 109]. As defined in detail elsewhere [94], finite element models were built from the binary micro-CT images of each vertebral body by converting each voxel into an 8-noded brick element with 6-micron edge-length, producing models with an average of 46 ± 11 million elements per model, depending the bone volume. Assuming homogeneous tissue properties within each bone, each element was assigned a reference tissue modulus of 1 GPa and a Poisson's ratio of 0.3. Linear elastic analyses using roller boundary conditions to simulate the compression experiments were performed using a custom code on an IBM Power4 supercomputer (DataStar, San Diego, CA). Then, the finite element-predicted vertebral stiffness was calibrated to the experimentally-measured vertebral stiffness to provide an averaged measure of tissue modulus for each vertebra, termed "effective tissue modulus"

[167]. This calculation assumes that the cortical and trabecular tissue have the same specimen-specific tissue modulus.

Contribution of cortical and trabecular compartments to bone stiffness

To determine the contribution of the cortical and trabecular compartments to whole bone stiffness, two additional finite element models were generated for each specimen. First, the cortical and trabecular compartments were identified in each image by manually tracing the endosteal surface of the cortex in every 40 slices (0.24 mm) and then extrapolating between the slices using the manufacturer's software (IPL v5.01c-ucsf, Scanco Medical AG). Then, each compartment was digitally isolated using image processing software (IDL v6.2, ITT) to create a model of the cortex alone and a model of the trabecular compartment alone (**Figure 4-1**). The same finite element analysis parameters used on the whole bones were applied to each isolated compartment to calculate cortical stiffness (K_{CORT}) and trabecular stiffness (K_{TRAB}), and the ratio of each of these to whole vertebral stiffness (K_{CORT}/K_{VB}, K_{TRAB}/K_{VB}).

Statistical analysis

Following all finite element analyses, the data were unblinded and analyzed to determine the effect of treatment on vertebral strength, strength-to-stiffness ratio, effective tissue modulus, microstructural parameters, and biomechanical contributions of the cortical and trabecular compartments. One-factor ANOVA with the Tukey-Kramer *post hoc* test was used for these purposes. The combined roles of BMC, tissue modulus, and cortical and trabecular microstructure in vertebral strength were quantified with stepwise multiple linear regression analysis. Since effective tissue modulus calculations are more sensitive to experimental noise than the other measurements, we performed a power analysis to determine the minimum detectable difference given the variation in the data for a power of 0.9; we provide sample sizes necessary for future studies given a desired minimum detectable difference. To assess net treatment effects on biomechanical bone quality, we tested for group differences in the relationship between strength and bone mineral content (BMC) and between trabecular stiffness and trabecular bone volume fraction (BV/TV). All statistical analyses were done using JMP (Version 7.0, SAS Institute Inc., Cary, NC). For all tests, $p<0.05$ was considered statistically significant.

4.3 Results

As expected, compared to sham, vertebral strength and stiffness (**Figure 4-2**) as well as bone mass, cortical thickness and trabecular microstructure (**Figure 4-3**) were altered by OVX and OVX+PTH treatment. OVX reduced vertebral strength and stiffness by 32% and this was accompanied by reduced bone mass, cortical thickness, and trabecular bone volume fraction, with fewer, thinner, and more rod-like trabeculae that had fewer interconnections. OVX+PTH treatment increased vertebral strength by 24%

and stiffness by 21% compared to sham, and this was accompanied by increased bone mass and bone volume fraction and restored or increased trabecular microarchitecture, where the primary effect was a 41% increase in trabecular thickness (**Figure 4-3**). The ratio of vertebral strength to stiffness (mean ± SD: 0.043 ± 0.007 mm) did not depend on treatment (p=0.98, **Figure 4-2 C**) indicating that there were no treatment effects on vertebral strength beyond those that occurred for vertebral stiffness.

Despite changes in overall mechanical behavior of the vertebrae with OVX and PTH treatment, the material properties of the bone tissue were remarkably uniform across the three groups (**Figure 4-4**). Effective tissue modulus (mean ± SD: 13.0 ± 2.5 GPa) did not depend on treatment (p=0.90) and was not correlated with mass or any microstructure parameter measured (p>0.13). Here, with 10 animals per group, the minimum detectable difference for effective tissue modulus was 3.8 GPa for a power of 0.9; larger sample sizes would be needed to detect more subtle changes in tissue modulus (**Figure 4-5**). Multiple regression analysis showed that variations in effective tissue modulus across all animals explained 3% variability in vertebral strength after accounting for bone mass and volume fraction (**Table 4-1**). This indicates that, as expected, variations in the elastic modulus of the tissue did have a role in between-specimen variations in vertebral strength, though this role was minor relative to that of mass and volume fraction.

Separating the cortical and trabecular compartments revealed that treatments affected these compartments differently (**Figure 4-6**). As expected, regardless of treatment, the stiffness of the trabecular compartment and its contribution to vertebral stiffness was much lower than that of the cortex because the trabecular bone makes up only about 30% of the total volume of bone tissue in these rat L2 vertebrae. Compared to sham, OVX decreased the stiffness of the trabecular compartment by 78% and its contribution to vertebral stiffness by 67% — consistent with the deteriorated trabecular bone volume fraction and microarchitecture — such that the cortex had a larger role in vertebral stiffness than in the sham or OVX+PTH groups. The OVX+PTH treatment resulted in a 29% stiffer cortex but the relative biomechanical roles of each compartment were not different than the sham group. It should be noted that the contributions of each compartment to vertebral stiffness do not sum to one because the interaction between the peripheral trabeculae and the cortex is lost when the compartments are separated.

Although a number of bone characteristics were altered by OVX or OVX+PTH treatment, or both, the relationship between measured vertebral strength and bone mass (BMC) was not altered by either treatment (p=0.9, **Figure 4-7 A**). Similarly, at the trabecular level, the relationship between finite element-predicted trabecular compartment stiffness and trabecular bone volume fraction was not altered by treatment (p=0.5, **Figure 4-7 B**). Thus, overall biomechanical bone quality was not affected by these treatments in these animals, indicating that changes observed in individual characteristics had little independent biomechanical effect after accounting for changes in bone mass and bone volume fraction.

4.4 Discussion

We have presented and tested a systematic approach for evaluating a range of structural and material bone quality characteristics and their biomechanical effects. This approach combines experimental, imaging, and computational techniques to efficiently measure strength, stiffness, strength-to-stiffness ratio, cortical thickness, trabecular microarchitecture, effective tissue elastic modulus, and the contributions of the cortical and trabecular compartments to whole bone behavior. Relationships between bone biomechanics and bone quantity are used to assess group differences in overall bone quality, while group differences in individual characteristics elucidate the mechanisms of biomechanical effects. The primary benefit of this approach is that it uses efficient, established techniques to provide a framework for consistent, comprehensive evaluation of biomechanical bone quality. It takes advantage of the fact that bone is a hierarchical structure by evaluating the most biomechanically relevant characteristics at each physical scale; depending on the goals of the study, post-hoc analysis can be performed to further isolate the source of the bone quality changes. The approach presented here is well suited for use in a variety of applications from determining the mechanisms of treatment efficacy to studying mechanisms of biomechanical effects of various bone diseases.

The results of our approach when applied to vertebrae from ovariectomized and PTH-treated rats were consistent with results from previous studies [168-171], providing some level of validation to our methods. The biomechanical testing and micro-CT-based microarchitectural analysis are well-established techniques, but the methods for estimating tissue material properties and the biomechanical contributions of the cortical and trabecular compartments are less common and have not been previously used to evaluate treatment effects. We found that despite treatment-induced changes to apparent mechanical properties, there were no differences in effective tissue modulus and strength-to-stiffness ratio, indicating that ovariectomy or PTH treatment did not alter the elastic and failure material properties of the bone tissue of these rat vertebrae. This finding was consistent with reports from a previous study using nanoindentation found no difference in tissue modulus of cortical bone from rat vertebrae between sham, OVX, and OVX+PTH treated groups [168]; further, the values reported for cortical modulus were very similar to those calculated in this current study (13.4-14.5 GPa). Interestingly, in that study, nanoindentation of trabecular bone found that PTH treatment decreased tissue modulus compared to sham and OVX controls, however, since our measurement is an average for the bulk tissue, and cortical bone composes about 70% of the total bone, the properties of the cortical bone dominate the behavior of these rat vertebrae. Effects of treatments on load sharing between the cortical and trabecular compartments has not been previously reported, but our findings were consistent with expectations based on cortical thickness and trabecular microarchitectural effects.

There are a number of advantages of this approach that make it an ideal method for pre-clinical evaluation of the effect of drug therapies on bone quality. It provides a systematic approach to characterizing biomechanical bone quality from the whole bone level down to the tissue level and by compartment. By taking advantage of relatively common micro-CT imaging analysis and biomechanical testing techniques and previously-validated high-resolution finite element methodology [34, 95, 107, 108], the method is both robust and efficient. It utilizes novel biomechanical analysis techniques

that enable measurement of tissue material properties and the load distribution between the cortical and trabecular compartments which are difficult to obtain experimentally. Further, the approach can easily be updated to include additional measurements for specific applications.

A few limitations of this approach should be mentioned. First, it does not provide a direct measurement of bone tissue properties. Nanoindentation can be used to make direct measurements on localized areas of exposed bone surfaces [172], but requires specialized equipment, is destructive, and is very time consuming. Nanoindentation is well suited for mapping properties on a spatially-resolved basis [168, 173], but it is not clear how these localized measures translate to mechanical properties of the bulk tissue. Also, the effective tissue modulus is a volume-averaged value and does not account for any intra-specimen variation in tissue properties; however, intra-specimen variation in modulus was shown to have a relatively constant biomechanical role across control and treated groups in rat vertebrae [174] and thus is not expected to be an important mechanism in fracture risk reduction. Further, the amount of variation in tissue modulus — whether due to natural biological heterogeneity or to noise in the experiments — may necessitate larger sample sizes if subtle treatment effects are to be detected; for example, about 30 specimens per group would be required to detect a difference of 2 GPa in tissue modulus. It is always important to consider expected variations in data when designing an experiment, but typically, the other characteristics measured here have less variation relative to the size of treatment effects and thus differences can be detected with smaller sample sizes.

It should also be noted that measurements of nanoscopic and molecular-level characteristics [175] are not included in this approach, primarily because they are typically more time consuming to make, require specialized equipment, or are destructive in nature. However, if biomechanically relevant changes occur at this level, there should be a net effect at a higher physical scale [15], such as in tissue properties or bone strength. The approach presented here prescribes the use of the relationship between measures of bone strength and bone density to assess whether net bone quality effects exist. If a net effect is found and there is evidence that molecular-level changes exist, additional analysis can be performed post-hoc on the yielded samples or adjacent bones, depending on the tests, to determine the source. If there is no net effect, then such small scale changes are likely not important mechanisms of biomechanical behavior and subsequent tests can be neglected.

In summary, we have presented a systematic approach for characterizing biomechanical bone quality that integrates changes at all physical scales into a clinically relevant result which may help elucidate the mechanisms of biomechanical alterations by diseases and treatments.

Table 4-1: Multiple regression analysis on biomechanically measured vertebral strength.

Model[a]	$\mathbf{r^2}$	***p*-value**
Mass	0.87	<0.0001
Mass+BV/TV	0.89	0.013
Mass+BV/TV+E_{tiss}	0.92	0.013

[a] Groups pooled for analysis (*n*=30 rats).

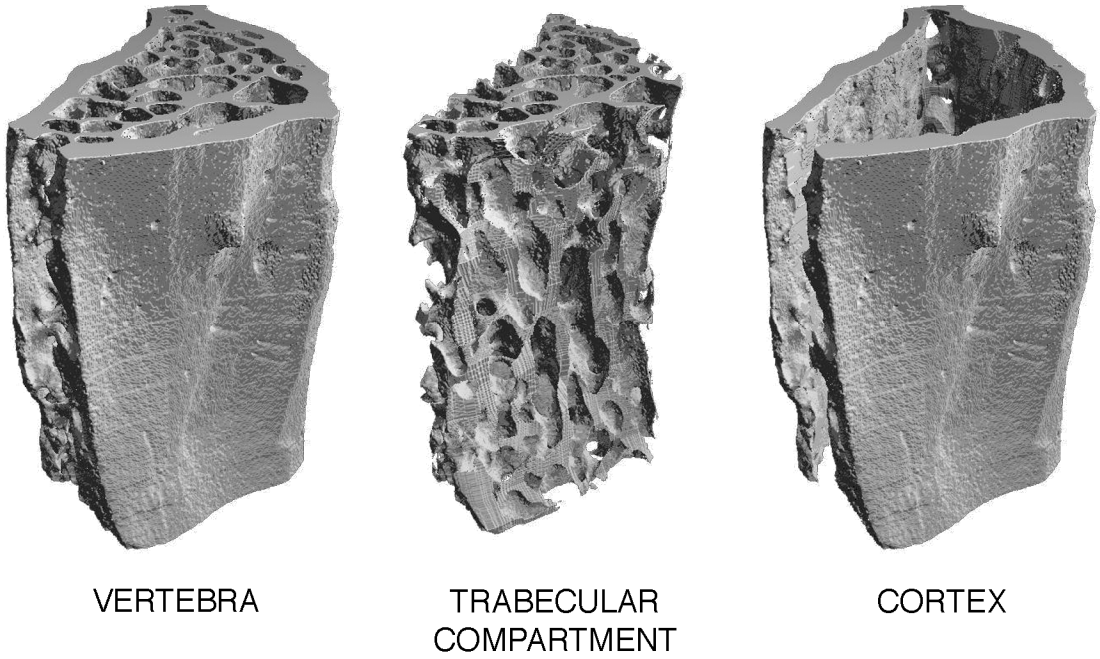

Figure 4-1: Three finite element models were built from the micro-CT image of each bone: the whole vertebra, the isolated trabecular compartment, and the isolated cortex.

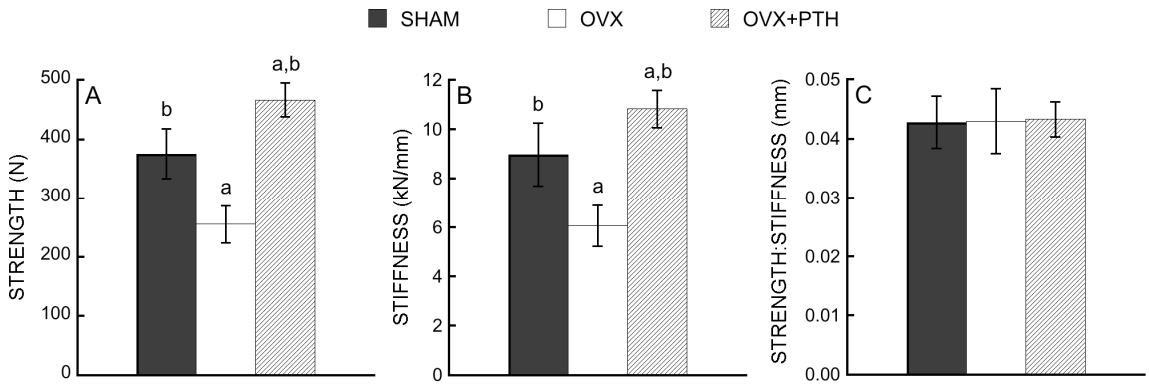

Figure 4-2: Results from biomechanical testing. Compared to sham, vertebral strength (A) and stiffness (B) were decreased by OVX and increased by OVX+PTH treatment. The strength-to-stiffness ratio (C) was not altered by either treatment indicating that there were no effects of treatment on vertebral strength beyond those for vertebral stiffness. Data shows mean ± 95% CI for n=10 rats per group. [a] p<0.05 vs. sham, [b] p<0.05 vs. OVX.

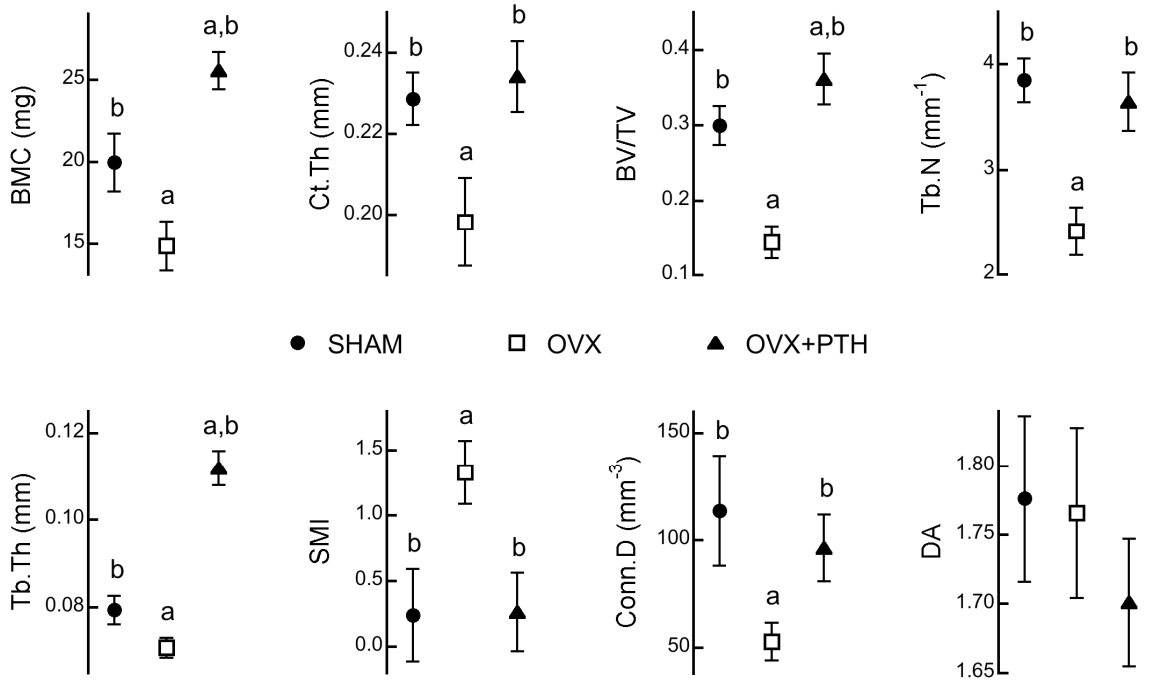

Figure 4-3: Effect of OVX+PTH treatment, compared to sham and OVX, on vertebral body BMC, cortical thickness, and trabecular microarchitecture. Data shows mean ± 95% CI for n=10 rats per group. [a] $p<0.05$ vs. sham, [b] $p<0.05$ vs. OVX.

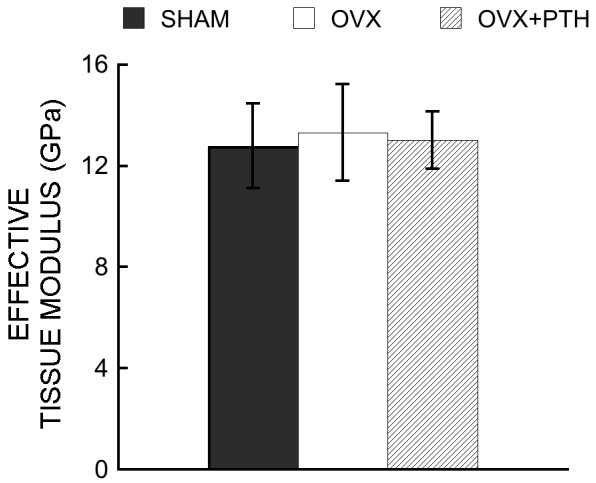

Figure 4-4: Compared to sham, the effective elastic modulus of the bone tissue was not altered by OVX or OVX+PTH treatment (p=0.9). Data shows mean ± 95% CI for n=10 rats per group.

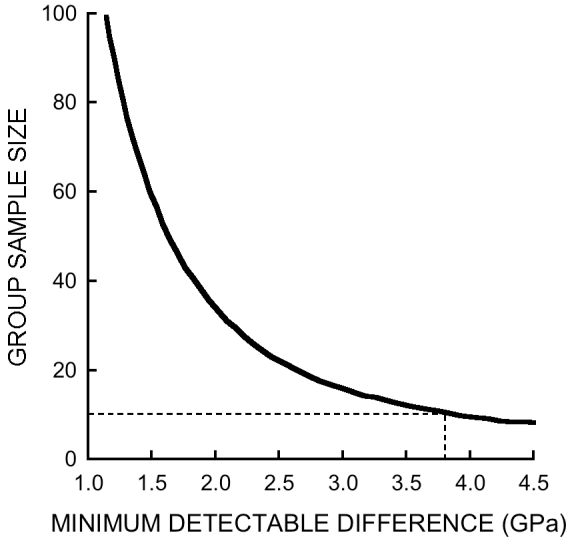

Figure 4-5: Power analysis calculations of the sample size per group necessary for a desired minimum detectable difference in tissue modulus, for a power of 0.9, assuming similar variation in the data as in this study (SD = 2.5 GPa). Dashed line shows configuration used in this study.

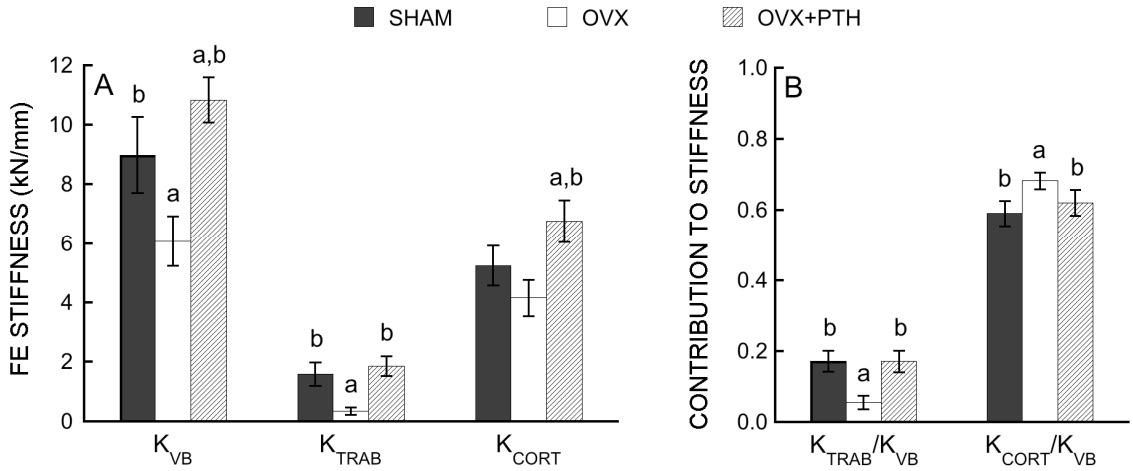

Figure 4-6: Finite element-predicted stiffness of the whole vertebra (K_{VB}), the trabecular compartment (K_{TRAB}) with cortex removed, and the cortex alone (K_{CORT}, A), and the ratio of the stiffness of each compartment to the stiffness of the whole vertebra (B), by group. Data shows mean ± 95% CI for n=10 rats per group. [a] $p<0.05$ vs. sham, [b] $p<0.05$ vs. OVX.

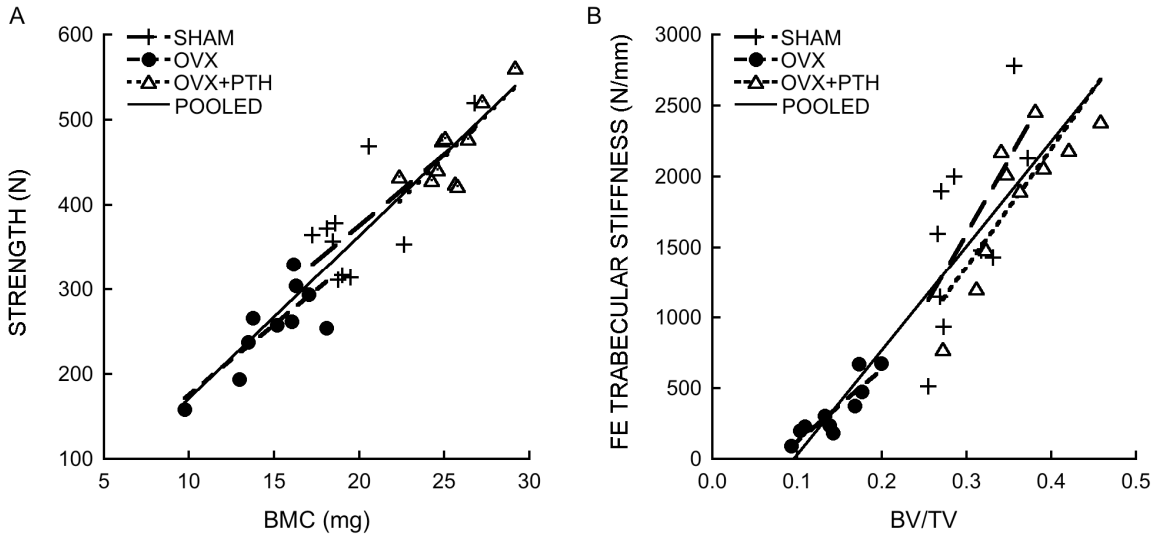

Figure 4-7: Biomechanically measured strength versus estimated bone mineral content (BMC, A) and finite element-predicted trabecular stiffness versus trabecular bone volume fraction (BV/TV, B). Neither relationship was altered by OVX or OVX+PTH ($p>0.5$). All relationships shown are significant ($p<0.026$).

5. CONCLUSIONS

The overall goals of this research were to improve understanding of the effects of osteoporosis therapies on the biomechanical behavior of bone. Substantial insight was gained into the mechanisms through which drug therapies might increase bone stiffness and strength, particularly with regards to alterations of the remodeling space and bone tissue mechanical properties. From a clinical perspective, the results of this dissertation have provided new pre-clinical approaches for evaluating disease and treatment effects on various aspects of bone quality.

The theory that suppression of resorption cavities with antiresorptive therapy improves bone strength by reducing stress risers has been a popular theory in the literature [85, 176] but previous studies have produced inconsistent results [90, 91], due in part to the limited representation of specimen heterogeneity in those studies. Hypothesizing that stress risers primarily affect low-density bone, we simulated microcavities in trabecular bone with a wide range of bone volume fraction and microarchitecture. We found that strength and the relationship between strength and bone volume fraction were both altered by the addition of microcavities. While this effect was indeed greater in low-density bone and also when the microcavities were targeted to regions of high tissue strain, an appreciable biomechanical effect persisted in all types of bone. Since this was not consistent with our expectations based on previous work on bisphosphonate-treated canine bone which showed no stress riser effect for this high-density bone [91], we conclude that this type of simulation does not properly represent the morphology or micromechanics of resorption-induced cavities and the stress riser theory remains an enigma. Thus, future work should focus on analyzing human trabeculae with and without resorption-induced cavities to determine the circumstances — if any — under which stress risers have an appreciable biomechanical effect. A combination of biomechanical tests and image-based finite element modeling of individual trabeculae is recommended to confirm if these types of voxel-based models sufficiently represent the micromechanics of the stress risers. Despite these remaining uncertainties, our findings nevertheless provide new insight into the possible clinical relevance of stress risers suggesting that antiresorptive therapies may be most effective via stress riser-suppression in patients with low bone volume fraction and high bone turnover.

Using the latest advances in micro-CT imaging, the biomechanical role of intra-specimen spatial variations in mineralization was quantitatively assessed in vertebra from rats from four different treatment groups. We found that any treatment-induced changes in the intra-specimen variations in mineralization had a negligible biomechanical effect in these rat vertebrae at the whole bone level and in the isolated trabecular compartment. Variations in mineralization did have a role in overall bone stiffness — being about 5% in the whole vertebra and 10% in the trabecular compartment — but this role was remarkably uniform across all specimens in all treatment groups considered. Thus, we conclude that biomechanical treatment effects are dominated by treatment-induced changes in trabecular microstructure and are negligibly influenced by the subtle changes in intra-specimen mineral variations. These findings imply that osteoporosis treatments — at least those analyzed here — act primarily through alteration of bone geometry and microstructure; it would be interesting to extend this study to include a bisphosphonate

because this class of pharmaceuticals has a stronger suppression effect on bone remodeling which may result in larger increases in degree of mineralization and tissue uniformity [38, 67]. If the findings of this study extend to human bone, then neglecting intra-specimen tissue heterogeneity in finite element analysis of bone from human biopsies should not obscure any biomechanical effects when comparing various treatments.

A secondary but important finding in this mineralization study was that our approach — using high-resolution micro-CT-based finite element analysis in a repeated measures study design — provided the ability to detect very small (<2%) treatment effects on the biomechanical role of intra-specimen mineral variations on overall bone stiffness. This approach could be useful in evaluating or detecting skeletal disease states in which large changes in the mineral distribution can occur [38], for example with osteomalacia [153], in either a research setting or on bone biopsies from patients in a clinical setting.

Chapter four focused on establishing and testing a framework for characterizing bone quality that integrated disease or treatment effects at all physical scales into a clinically relevant result. Using a combined experimental-computational approach, the results of this approach enable a systematic approach to evaluating the complex hierarchical structure of bone. This “road map” represents an efficient pre-clinical approach that seeks to reduce time and efforts by providing a series of ordered tests whose outcomes dictate subsequent steps. For example, if the first test finds that there is no effect on the relationship between strength and bone mass (or analogous measures), it can be concluded that there is no net bone quality effect, and subsequent tests are not necessary. If a net bone quality effect is found, then the “road map” directs further tests to isolate the source. By applying this approach to treated rat vertebrae, we found that, compared to the control, neither ovariectomy nor parathyroid hormone treatment altered bone quality despite changes in bone strength during compression loading. There may be loading scenarios, such as shearing, multiaxial or cyclic loading, in which biomechanical bone quality is altered by these treatments since there is evidence that failure mechanisms of trabecular bone depends on loading mode [103]. Using the same approach, additional loading modes, such as torsion, can be modeled for the same bones in a repeated-measures analysis [91] to determine the sensitivity to loading mode. The models used do not include microdamage and therefore would not be appropriate for a fatigue analysis without adaptation. This framework is suitable for a number of pre-clinical applications ranging from aging and skeletal diseases, to pharmaceutical and genetic therapies and could be readily adapted for analysis of human biopsies from patients before and after treatment.

There are a number of strengths of this research. First, we exploited the capabilities of finite element modeling to implement repeated measures study designs, which provided statistical detection of very small biomechanical effects, and to perform parametric perturbations, which provided direct effects of changes in individual characteristics. Related, the use of finite element models of vertebrae with and without the cortical shell — a unique advantage of micro-CT-based modeling — enabled us to determine the biomechanical role of each compartment and if treatments preferentially affected trabecular bone versus the cortex. Second, we studied the effects of both

antiresorptive and anabolic therapies since each class of treatment alters bone strength through different mechanisms of action on bone remodeling. Third, we incorporated the latest advances in micro-CT imaging into high-resolution (6-micron voxel size) finite element modeling to spatially resolve actual mineral density variations onto the detailed microstructure of each specimen through the use of a calibration phantom and sophisticated artifact-correction algorithms [97, 98]. Fourth, we developed a protocol for precise preparation and biomechanical testing of rat vertebrae to minimize machine compliance and end artifacts [165] in measurements of stiffness — a metric that is particularly sensitive to such experimental artifacts. Finally, we used relatively large sample sizes with specimens that spanned a wide range of bone volume fractions, microarchitectures, and mineralization phenotypes to account for natural biological heterogeneity and provide a reasonable degree of external validity to the results.

The study on the effects of resorption cavities raised important questions about the suitability of using a non-ovariectomized canine model for studies of bone turnover suppression, highlighting the need for the development of an animal model with remodeling characteristics more similar to osteoporotic human bone. Based on our results showing that the stress riser effect depends on bone density, a critical aspect of an ideal animal model would be a baseline bone volume fraction similar to elderly human bone, as well as having resorption cavities of a similar size and prevalence to human bone. Nevertheless, existing canine models, as well as other large animal models, can still be used to study other aspects of treatment effects — such as tissue-level material properties and microdamage — and represent an important part of pre-clinical pharmaceutical evaluation.

Future research is recommended to address remaining questions and further extend the relevance of the results presented in this dissertation. One important area will be determining the circumstances under which suppression of resorption cavities improves bone strength beyond any changes in bone mass. Since simulated microcavities as prescribed in this work do not appear to represent the morphology or micromechanics of actual resorption-induced cavities, a more accurate representation of resorption cavities and their variation across anatomic sites and species is needed. Biomechanical testing combined with finite element modeling based on nano-scale imaging (*e.g.* 500-1000 nm voxel size) of excised individual trabeculae with and without observed resorption cavities should provide substantial closure to this issue. The first step will be to validate the finite element models against the experiments and to make any modifications to capture the physics of the stress risers. Then the validated models can be used to compare stress riser effects across trabeculae from human biopsies before and after various treatments. Additionally, characterizing the size, depth, and prevalence of resorption cavities in common animal models, such as dog and rat, using three-dimensional imaging techniques [177] and comparing such measures to those known for postmenopausal women [58, 112, 113] should help interpret pre-clinical study results.

Another area of future research is regarding the role of mineralization in treatment efficacy. The clinical relevance of the current results is limited since the rat model used may be more homogeneous than the general population. A natural extension of this work will be to apply the techniques described in this dissertation to biopsies of bone from patients before and after antiresorptive or anabolic drug therapy. Further, nonlinear finite

element models with heterogeneous tissue properties should be implemented to confirm the role of mineralization variations in yield behavior.

Future research is also recommended to apply the framework for bone quality characterization to bone from animals or human biopsies from a variety of treatments. Compared to PTH, other treatments, such as bisphosphonates, can have larger effects on bone tissue [67] and have the opposite effect on bone remodeling. Thus, comparing bone quality effects and the sources of any changes across treatments should provide insight into the differences in their biomechanical mechanisms of action and may guide treatment-specific evaluation of efficacy in patients.

In closure, this dissertation research has increased knowledge regarding the mechanisms through which osteoporosis therapies improve bone strength without appreciably increasing bone mass. In particular, it appears that suppression of resorption cavities may substantially increase bone strength by mitigating stress risers, but only in a subset of patients with low bone volume fraction and high bone turnover. The studies on treated rat bone revealed that biomechanical effects of treatments are dominated by geometric and microarchitectural changes and that tissue mineralization changes had only a subtle biomechanical effect. This research also produced an efficient pre-clinical framework for characterizing bone quality which should produce considerable insight into the mechanisms of biomechanical effects in a broad range of bone research applications. Using this framework, we found that neither ovariectomy nor PTH treatment had a net effect on bone quality of rat vertebrae during compressive loading. This dissertation also outlines areas of research to further advance this field of study.

6. REFERENCES

[1] National Osteoporosis Foundation. http://www.nof.org/. Washington, D.C.; 2010.

[2] McClung MR, San Martin J, Miller PD, Civitelli R, Bandeira F, Omizo M, Donley DW, Dalsky GP, Eriksen EF. Opposite bone remodeling effects of teriparatide and alendronate in increasing bone mass. Arch Intern Med 2005;165: 1762-8.

[3] Russell RG, Rogers MJ. Bisphosphonates: from the laboratory to the clinic and back again. Bone 1999;25: 97-106.

[4] Dempster DW, Cosman F, Kurland ES, Zhou H, Nieves J, Woelfert L, Shane E, Plavetic K, Muller R, Bilezikian J, Lindsay R. Effects of daily treatment with parathyroid hormone on bone microarchitecture and turnover in patients with osteoporosis: a paired biopsy study. J Bone Miner Res 2001;16: 1846-53.

[5] Rubin MR, Bilezikian JP. Parathyroid hormone as an anabolic skeletal therapy. Drugs 2005;65: 2481-98.

[6] Black DM, Thompson DE, Bauer DC, Ensrud K, Musliner T, Hochberg MC, Nevitt MC, Suryawanshi S, Cummings SR. Fracture risk reduction with alendronate in women with osteoporosis: the Fracture Intervention Trial. FIT Research Group. J Clin Endocrinol Metab 2000;85: 4118-24.

[7] Neer RM, Arnaud CD, Zanchetta JR, Prince R, Gaich GA, Reginster JY, Hodsman AB, Eriksen EF, Ish-Shalom S, Genant HK, Wang O, Mitlak BH. Effect of parathyroid hormone (1-34) on fractures and bone mineral density in postmenopausal women with osteoporosis. N Engl J Med 2001;344: 1434-41.

[8] Cummings SR, Karpf DB, Harris F, Genant HK, Ensrud K, LaCroix AZ, Black DM. Improvement in spine bone density and reduction in risk of vertebral fractures during treatment with antiresorptive drugs. Am J Med 2002;112: 281-289.

[9] Delmas PD, Seeman E. Changes in bone mineral density explain little of the reduction in vertebral or nonvertebral fracture risk with anti-resorptive therapy. Bone 2004;34: 599-604.

[10] Watts NB, Geusens P, Barton IP, Felsenberg D. Relationship between changes in BMD and nonvertebral fracture incidence associated with risedronate: reduction in risk of nonvertebral fracture is not related to change in BMD. J Bone Miner Res 2005;20: 2097-104.

[11] Bouxsein ML. Bone quality: where do we go from here? Osteoporos Int 2003;14 Suppl 5: S118-27.

[12] Chesnut CH, 3rd, Rosen CJ. Reconsidering the effects of antiresorptive therapies in reducing osteoporotic fracture. J Bone Miner Res 2001;16: 2163-72.

[13] Burr DB. Bone quality: understanding what matters. J Musculoskelet Neuronal Interact 2004;4: 184-6.

[14] Felsenberg D, Boonen S. The bone quality framework: determinants of bone strength and their interrelationships, and implications for osteoporosis management. Clin Ther 2005;27: 1-11.

[15] Hernandez CJ, Keaveny TM. A biomechanical perspective on bone quality. Bone 2006;39: 1173-81.

[16] Seeman E. Bone quality: the material and structural basis of bone strength. J Bone Miner Metab 2008;26: 1-8.

[17] Benhamou CL. Effects of osteoporosis medications on bone quality. Joint Bone Spine 2007;74: 39-47.
[18] Watts NB. Bone quality: getting closer to a definition. J Bone Miner Res 2002;17: 1148-50.
[19] Hulme PA, Boyd SK, Ferguson SJ. Regional variation in vertebral bone morphology and its contribution to vertebral fracture strength. Bone 2007;41: 946-57.
[20] Fields AJ, Eswaran SK, Jekir MG, M KT. Role of trabecular microarchitecture in whole-verterbal body biomechanical behavior. J Bone Miner Res 2009;24: 1523-30.
[21] Müller R, Hannan M, Smith SY, Bauss F. Intermittent ibandronate preserves bone quality and bone strength in the lumbar spine after 16 months of treatment in the ovariectomized cynomolgus monkey. J Bone Miner Res 2004;19: 1787-96.
[22] Fox J, Miller MA, Newman MK, Recker RR, Turner CH, Smith SY. Effects of daily treatment with parathyroid hormone 1-84 for 16 months on density, architecture and biomechanical properties of cortical bone in adult ovariectomized rhesus monkeys. Bone 2007;41: 321-30.
[23] Bartel DL, Davy DT, Keaveny TM. Orthopaedic biomechanics: Mechanics and design in musculoskeletal systems. Upper Saddle River, NJ: Pearson Prentice Hall; 2006, p. 71-120.
[24] Brinckmann P, Biggemann M, Hilweg D. Prediction of the compressive strength of human lumbar vertebrae. Spine 1989;14: 606-10.
[25] Lang SM, Moyle DD, Berg EW, Detorie N, Gilpin AT, Pappas NJ, Reynolds JC, Tkackik M, Waldron RL. Correlation of mechanical properties of vertebral trabecular bone with equivalent mineral density as measured by computed tomography. Journal of Bone and Joint Surgery 1988;70-A: 1531-1538.
[26] Hvid I, Bentzen SM, Linde F, Mosekilde L, Pongsoipetch B. X-ray quantitative computed tomography: the relations to physical properties of proximal tibial trabecular bone specimens. J Biomech 1989;22: 837-44.
[27] Lotz JC, Gerhart TN, Hayes WC. Mechanical properties of trabecular bone from the proximal femur: a quantitative CT study. J Comput Assist Tomogr 1990;14: 107-14.
[28] Kopperdahl DL, Keaveny TM. Yield strain behavior of trabecular bone. J Biomech 1998;31: 601-8.
[29] Homminga J, McCreadie BR, Weinans H, Huiskes R. The dependence of the elastic properties of osteoporotic cancellous bone on volume fraction and fabric. J Biomech 2003;36: 1461-7.
[30] Newitt DC, Majumdar S, van Rietbergen B, von Ingersleben G, Harris ST, Genant HK, Chesnut C, Garnero P, MacDonald B. In vivo assessment of architecture and micro-finite element analysis derived indices of mechanical properties of trabecular bone in the radius. Osteoporos Int 2002;13: 6-17.
[31] Ulrich D, van Rietbergen B, Laib A, Ruegsegger P. The ability of three-dimensional structural indices to reflect mechanical aspects of trabecular bone. Bone 1999;25: 55-60.
[32] Bevill G, Farhamand F, Keaveny TM. Heterogeneity of yield strain in low-density versus high-density human trabecular bone. J Biomech 2009;42: 2165-70.
[33] Snyder BD, Piazza S, Edwards WT, Hayes WC. Role of trabecular morphology in the etiology of age-related vertebral fractures. Calcif Tissue Int 1993;53S: S14-S22.

[34] Bevill G, Eswaran SK, Gupta A, Papadopoulos P, Keaveny TM. Influence of bone volume fraction and architecture on computed large-deformation failure mechanisms in human trabecular bone. Bone 2006;39: 1218-25.
[35] Morgan EF, Bayraktar HH, Yeh OC, Majumdar S, Burghardt A, Keaveny TM. Contribution of inter-site variations in architecture to trabecular bone apparent yield strains. J Biomech 2004;37: 1413-20.
[36] Currey JD. The effect of porosity and mineral content on the Young's modulus of elasticity of compact bone. J Biomech 1988;21: 131-9.
[37] Boivin G, Meunier PJ. The mineralization of bone tissue: a forgotten dimension in osteoporosis research. Osteoporos Int 2003;14 Suppl 3: S19-24.
[38] Roschger P, Paschalis EP, Fratzl P, Klaushofer K. Bone mineralization density distribution in health and disease. Bone 2008;42: 456-66.
[39] Paschalis EP, Betts F, DiCarlo E, Mendelsohn R, Boskey AL. FTIR microspectroscopic analysis of human iliac crest biopsies from untreated osteoporotic bone. Calcif Tissue Int 1997;61: 487-92.
[40] Paschalis EP, Shane E, Lyritis G, Skarantavos G, Mendelsohn R, Boskey AL. Bone fragility and collagen cross-links. J Bone Miner Res 2004;19: 2000-4.
[41] Boskey AL, Wright TM, Blank RD. Collagen and bone strength. J Bone Miner Res 1999;14: 330-5.
[42] Burr D. Microdamage and bone strength. Osteoporos Int 2003;14 Suppl 5: S67-72.
[43] Boivin G, Bala Y, Doublier A, Farlay D, Ste-Marie LG, Meunier PJ, Delmas PD. The role of mineralization and organic matrix in the microhardness of bone tissue from controls and osteoporotic patients. Bone 2008;43: 532-8.
[44] Burr DB, Forwood MR, Fyhrie DP, Martin RB, Schaffler MB, Turner CH. Bone microdamage and skeletal fragility in osteoporotic and stress fractures. J Bone Miner Res 1997;12: 6-15.
[45] Norman TL, Yeni YN, Brown CU, Wang Z. Influence of microdamage on fracture toughness of the human femur and tibia. Bone 1998;23: 303-6.
[46] Silva MJ, Wang C, Keaveny TM, Hayes WC. Direct and Computed-Tomography Thickness Measurements of the Human, Lumbar Vertebral Shell and End-Plate. Bone 1994;15: 409-414.
[47] Edwards WT, Zheng YG, Ferrara LA, Yuan HA. Structural features and thickness of the vertebral cortex in the thoracolumbar spine. Spine 2001;26: 218-225.
[48] Ritzel H, Amling M, Posl M, Hahn M, Delling G. The thickness of human vertebral cortical bone and its changes in aging and osteoporosis: A histomorphometric analysis of the complete spinal column from thirty-seven autopsy specimens. J Bone Miner Res 1997;12: 89-95.
[49] Vesterby A, Mosekilde L, Gundersen HJG, Melsen F, Mosekilde L, Holem K, Sorensen S. Biologically meaningful determinants of the in vitro strength of lumbar vertebrae. Bone 1991;12: 219-224.
[50] Rockoff SD, Sweet E, Bleustein J. The relative contribution of trabecular and cortical bone to the strength of human lumbar vertebrae. Calcif Tiss Res 1969;3: 163-175.

[51] Mcbroom RJ, Hayes WC, Edwards WT, Goldberg RP, White AA. Prediction of Vertebral Body Compressive Fracture Using Quantitative Computed-Tomography. J Bone Joint Surg Am 1985;67A: 1206-1214.
[52] Yoganandan N, Myklebust JB, Cusick JF, Wilson CR, Sances A. Functional biomechanics of the thoracolumbar vertebral cortex. Clin Biomech 1988;3: 11-18.
[53] Homminga J, Van-Rietbergen B, Lochmuller EM, Weinans H, Eckstein F, Huiskes R. The osteoporotic vertebral structure is well adapted to the loads of daily life, but not to infrequent "error" loads. Bone 2004;34: 510-6.
[54] Eswaran SK, Gupta A, Adams MF, Keaveny TM. Cortical and trabecular load sharing in the human vertebral body. J Bone Miner Res 2006;21: 307-14.
[55] Eswaran SK, Bayraktar HH, Adams MF, Gupta A, Hoffman PF, Lee DC, Papadopoulos P, Keaveny TM. The micromechanics of cortical shell removal in the human vertebral body. Comput Method Appl M 2007;196: 3025-32.
[56] Parfitt AM. Misconceptions (2): turnover is always higher in cancellous than in cortical bone. Bone 2002;30: 807-9.
[57] Taylor AF, Saunders MM, Shingle DL, Cimbala JM, Zhou Z, Donahue HJ. Mechanically stimulated osteocytes regulate osteoblastic activity via gap junctions. Am J Physiol Cell Physiol 2007;292: C545-52.
[58] Parfitt AM. Osteonal and hemi-osteonal remodeling: the spatial and temporal framework for signal traffic in adult human bone. J Cell Biochem 1994;55: 273-86.
[59] Riggs BL, Melton LJ. Involutional osteoporosis. New Engl J Med 1986;314: 1676-1686.
[60] Riggs BL, Parfitt AM. Drugs used to treat osteoporosis: the critical need for a uniform nomenclature based on their action on bone remodeling. J Bone Miner Res 2005;20: 177-84.
[61] Rodan GA. Mechanisms of action of bisphosphonates. Annu Rev Pharmacol Toxicol 1998;38: 375-88.
[62] Greenspan SL, Parker RA, Ferguson L, Rosen HN, Maitland-Ramsey L, Karpf DB. Early changes in biochemical markers of bone turnover predict the long-term response to alendronate therapy in representative elderly women: a randomized clinical trial. J Bone Miner Res 1998;13: 1431-8.
[63] Russell RG, Rogers MJ, Frith JC, Luckman SP, Coxon FP, Benford HL, Croucher PI, Shipman C, Fleisch HA. The pharmacology of bisphosphonates and new insights into their mechanisms of action. J Bone Miner Res 1999;14 Suppl 2: 53-65.
[64] Storm T, Steiniche T, Thamsborg G, Melsen F. Changes in bone histomorphometry after long-term treatment with intermittent, cyclic etidronate for postmenopausal osteoporosis. J Bone Miner Res 1993;8: 199-208.
[65] Chavassieux PM, Arlot ME, Reda C, Wei L, Yates AJ, Meunier PJ. Histomorphometric assessment of the long-term effects of alendronate on bone quality and remodeling in patients with osteoporosis. J Clin Invest 1997;100: 1475-80.
[66] Meunier PJ, Boivin G. Bone mineral density reflects bone mass but also the degree of mineralization of bone: therapeutic implications. Bone 1997;21: 373-7.
[67] Boivin GY, Chavassieux PM, Santora AC, Yates J, Meunier PJ. Alendronate increases bone strength by increasing the mean degree of mineralization of bone tissue in osteoporotic women. Bone 2000;27: 687-694.

[68] Roschger P, Rinnerthaler S, Yates J, Rodan GA, Fratzl P, Klaushofer K. Alendronate increases degree and uniformity of mineralization in cancellous bone and decreases the porosity in cortical bone of osteoporotic women. Bone 2001;29: 185-91.
[69] Borah B, Ritman EL, Dufresne TE, Jorgensen SM, Liu S, Sacha J, Phipps RJ, Turner RT. The effect of risedronate on bone mineralization as measured by micro-computed tomography with synchrotron radiation: correlation to histomorphometric indices of turnover. Bone 2005;37: 1-9.
[70] Black DM, Cummings SR, Karpf DB, Cauley JA, Thompson DE, Nevitt MC, Bauer DC, Genant HK, Haskell WL, Marcus R, Ott SM, Torner JC, Quandt SA, Reiss TF, Ensrud KE. Randomised trial of effect of alendronate on risk of fracture in women with existing vertebral fractures. Fracture Intervention Trial Research Group [see comments]. Lancet 1996;348: 1535-41.
[71] Ettinger B, Black DM, Mitlak BH, Knickerbocker RK, Nickelsen T, Genant HK, Christiansen C, Delmas PD, Zanchetta JR, Stakkestad J, Gluer CC, Krueger K, Cohen FJ, Eckert S, Ensrud KE, Avioli LV, Lips P, Cummings SR. Reduction of vertebral fracture risk in postmenopausal women with osteoporosis treated with raloxifene: results from a 3-year randomized clinical trial. Multiple Outcomes of Raloxifene Evaluation (MORE) Investigators. Jama 1999;282: 637-45.
[72] Storm T, Thamsborg G, Steiniche T, Genant HK, Sorensen OH. Effect of intermittent cyclical etidronate therapy on bone mass and fracture rate in women with postmenopausal osteoporosis [see comments]. New Engl J Med 1990;322: 1265-71.
[73] Lindsay R, Nieves J, Formica C, Henneman E, Woelfert L, Shen V, Dempster D, Cosman F. Randomised controlled study of effect of parathyroid hormone on vertebral-bone mass and fracture incidence among postmenopausal women on oestrogen with osteoporosis. Lancet 1997;350: 550-5.
[74] Zhou H, Iida-Klein A, Lu SS, Ducayen-Knowles M, Levine LR, Dempster DW, Lindsay R. Anabolic action of parathyroid hormone on cortical and cancellous bone differs between axial and appendicular skeletal sites in mice. Bone 2003;32: 513-20.
[75] Misof BM, Roschger P, Cosman F, Kurland ES, Tesch W, Messmer P, Dempster DW, Nieves J, Shane E, Fratzl P, Klaushofer K, Bilezikian J, Lindsay R. Effects of intermittent parathyroid hormone administration on bone mineralization density in iliac crest biopsies from patients with osteoporosis: a paired study before and after treatment. J Clin Endocrinol Metab 2003;88: 1150-6.
[76] Jiang Y, Zhao JJ, Mitlak BH, Wang O, Genant HK, Eriksen EF. Recombinant human parathyroid hormone (1-34) [teriparatide] improves both cortical and cancellous bone structure. J Bone Miner Res 2003;18: 1932-41.
[77] Burr DB, Hirano T, Turner CH, Hotchkiss C, Brommage R, Hock JM. Intermittently administered human parathyroid hormone(1-34) treatment increases intracortical bone turnover and porosity without reducing bone strength in the humerus of ovariectomized cynomolgus monkeys. J Bone Miner Res 2001;16: 157-65.
[78] Neer M, Slovik DM, Daly M, Potts T, Jr., Nussbaum SR. Treatment of postmenopausal osteoporosis with daily parathyroid hormone plus calcitriol. Osteoporos Int 1993;3 Suppl 1: 204-5.
[79] Macdonald HM, Nishiyama KK, Hanley DA, Boyd SK. Changes in trabecular and cortical bone microarchitecture at peripheral sites associated with 18 months of teriparatide therapy in postmenopausal women with osteoporosis. Osteoporos Int 2010.

[80] Allen MR, Gineyts E, Leeming DJ, Burr DB, Delmas PD. Bisphosphonates alter trabecular bone collagen cross-linking and isomerization in beagle dog vertebra. Osteoporos Int 2008;19: 329-37.
[81] Paschalis EP, Glass EV, Donley DW, Eriksen EF. Bone mineral and collagen quality in iliac crest biopsies of patients given teriparatide: new results from the fracture prevention trial. J Clin Endocrinol Metab 2005;90: 4644-9.
[82] Gamsjaeger S, Buchinger B, Zwettler E, Recker R, Black D, Gasser JA, Eriksen EF, Klaushofer K, Paschalis EP. Bone material properties in actively bone-forming trabeculae in postmenopausal women with osteoporosis after three years of treatment with once-yearly zoledronic acid. J Bone Miner Res 2010.
[83] Allen MR, Iwata K, Phipps R, Burr DB. Alterations in canine vertebral bone turnover, microdamage accumulation, and biomechanical properties following 1-year treatment with clinical treatment doses of risedronate or alendronate. Bone 2006;39: 872-9.
[84] Mashiba T, Turner CH, Hirano T, Forwood MR, Johnston CC, Burr DB. Effects of suppressed bone turnover by bisphosphonates on microdamage accumulation and biomechanical properties in clinically relevant skeletal sites in beagles. Bone 2001;28: 524-31.
[85] Parfitt AM. High bone turnover is intrinsically harmful: two paths to a similar conclusion. The Parfitt view. J Bone Miner Res 2002;17: 1558-9; author reply 1560.
[86] Riggs BL, Melton LJ, 3rd. Bone turnover matters: the raloxifene treatment paradox of dramatic decreases in vertebral fractures without commensurate increases in bone density. J Bone Miner Res 2002;17: 11-4.
[87] Heaney RP. The bone-remodeling transient: implications for the interpretation of clinical studies of bone mass change. J Bone Miner Res 1994;9: 1515-23.
[88] Allen MR, Erickson AM, Wang X, Burr DB, Martin RB, Hazelwood SJ. Morphological assessment of basic multicellular unit resorption parameters in dogs shows additional mechanisms of bisphosphonate effects on bone. Calcif Tissue Int 2010;86: 67-71.
[89] McNamara LM, Van der Linden JC, Weinans H, Prendergast PJ. Stress-concentrating effect of resorption lacunae in trabecular bone. J Biomech 2006;39: 734-41.
[90] Hernandez CJ, Gupta A, Keaveny TM. A biomechanical analysis of the effects of resorption cavities on cancellous bone strength. J Bone Miner Res 2006;21: 1248-55.
[91] Eswaran SK, Allen MR, Burr DB, Keaveny TM. A computational assessment of the independent contribution of changes in canine trabecular bone volume fraction and microarchitecture to increased bone strength with suppression of bone turnover. J Biomech 2007;40: 3424-31.
[92] Delmas PD. How does antiresorptive therapy decrease the risk of fracture in women with osteoporosis? Bone 2000;27: 1-3.
[93] Beck JD, Canfield BL, Haddock SM, Chen TJ, Kothari M, Keaveny TM. Three-dimensional imaging of trabecular bone using the computer numerically controlled milling technique. Bone 1997;21: 281-7.
[94] Hollister SJ, Brennan JM, Kikuchi N. A homogenization sampling procedure for calculating trabecular bone effective stiffness and tissue level stress. J Biomech 1994;27: 433-444.

[95] Hou FJ, Lang SM, Hoshaw SJ, Reimann DA, Fyhrie DP. Human vertebral body apparent and hard tissue stiffness. Journal of Biomechanics 1998;31: 1009-15.
[96] Eswaran SK, Gupta A, Keaveny TM. Locations of bone tissue at high risk of initial failure during compressive loading of the human vertebral body. Bone 2007;41: 733-9.
[97] Kazakia GJ, Burghardt AJ, Cheung S, Majumdar S. Assessment of bone tissue mineralization by conventional x-ray microcomputed tomography: comparison with synchrotron radiation microcomputed tomography and ash measurements. Med Phys 2008;35: 3170-9.
[98] Burghardt AJ, Kazakia GJ, Laib A, Majumdar S. Quantitative assessment of bone tissue mineralization with polychromatic micro-computed tomography. Calcif Tissue Int 2008;83: 129-38.
[99] van Ruijven LJ, Mulder L, van Eijden TM. Variations in mineralization affect the stress and strain distributions in cortical and trabecular bone. J Biomech 2007;40: 1211-8.
[100] Bourne BC, van der Meulen MC. Finite element models predict cancellous apparent modulus when tissue modulus is scaled from specimen CT-attenuation. J Biomech 2004;37: 613-21.
[101] Bayraktar HH, Gupta A, Kwon RY, Papadopoulos P, Keaveny TM. The modified super-ellipsoid yield criterion for human trabecular bone. J Biomech Eng 2004;126: 677-84.
[102] Pistoia W, van Rietbergen B, Ruegsegger P. Mechanical consequences of different scenarios for simulated bone atrophy and recovery in the distal radius. Bone 2003;33: 937-45.
[103] Niebur GL, Feldstein MJ, Keaveny TM. Biaxial failure behavior of bovine tibial trabecular bone. Journal of Biomechanical Engineering 2002;124: 699-705.
[104] Bevill G, Eswaran SK, Farahmand F, Keaveny TM. The influence of boundary conditions and loading mode on high-resolution finite element-computed trabecular tissue properties. Bone 2009;44: 573-8.
[105] Nagaraja S, Couse TL, Guldberg RE. Trabecular bone microdamage and microstructural stresses under uniaxial compression. J Biomech 2005;38: 707-16.
[106] Eswaran SK, Fields AJ, Nagarathnam P, Keaveny TM. Multi-scale modeling of the human vertebral body: comparison of micro-CT based high-resolution and continuum-level models. Pac Symp Biocomput 2009: 293-303.
[107] Niebur GL, Feldstein MJ, Yuen JC, Chen TJ, Keaveny TM. High-resolution finite element models with tissue strength asymmetry accurately predict failure of trabecular bone. J Biomech 2000;33: 1575-1583.
[108] Ito M, Nishida A, Koga A, Ikeda S, Shiraishi A, Uetani M, Hayashi K, Nakamura T. Contribution of trabecular and cortical components to the mechanical properties of bone and their regulating parameters. Bone 2002;31: 351-8.
[109] Van Rietbergen B, Weinans H, Huiskes R, Odgaard A. A new method to determine trabecular bone elastic properties and loading using micromechanical finite element models. J Biomech 1995;28: 69-81.
[110] Adams MF, Bayraktar HH, Keaveny TM, Papadopoulos P. Ultrascalable implicit finite element analyses in solid mechanics with over a half a billion degrees of freedom. In: ACM/IEEE Proceedings of SC2004: High Performance Networking and Computing; 2004.

[111] Mosekilde L. Age-related changes in bone mass, structure, and strength--effects of loading. Z Rheumatol 2000;59 Suppl 1: 1-9.
[112] Mosekilde L. Consequences of the remodelling process for vertebral trabecular bone structure: a scanning electron microscopy study (uncoupling of unloaded structures). Bone Miner 1990;10: 13-35.
[113] Eriksen EF, Hodgson SF, Eastell R, Cedel SL, O'Fallon WM, Riggs BL. Cancellous bone remodeling in type I (postmenopausal) osteoporosis: quantitative assessment of rates of formation, resorption, and bone loss at tissue and cellular levels. J Bone Miner Res 1990;5: 311-9.
[114] Papadopoulos P, Lu J. On the formulation and numerical solution of problems in anisotropic finite plasticity. Comput Method Appl M 2001;190: 4889-4910.
[115] Wang X, Erickson AM, Allen MR, Burr DB, Martin RB, Hazelwood SJ. Theoretical analysis of alendronate and risedronate effects on canine vertebral remodeling and microdamage. J Biomech 2009;42: 938-44.
[116] Boyce RW, Paddock CL, Gleason JR, Sletsema WK, Eriksen EF. The effects of risedronate on canine cancellous bone remodeling: three-dimensional kinetic reconstruction of the remodeling site. J Bone Miner Res 1995;10: 211-21.
[117] Jaworski ZF, Lok E. The rate of osteoclastic bone erosion in Haversian remodeling sites of adult dog's rib. Calcif Tissue Res 1972;10: 103-12.
[118] Jaworski ZF, Meunier P, Frost HM. Observations on two types of resorption cavities in human lamellar cortical bone. Clin Orthop Relat Res 1972;83: 279-85.
[119] van der Linden JC, Verhaar JA, Weinans H. A three-dimensional simulation of age-related remodeling in trabecular bone. J Bone Miner Res 2001;16: 688-96.
[120] Hernandez CJ, Gupta A, M KT. Remodeling cavities and stress risers: A biomechanical study on cancellous bone strength. In: 27th Annual Meeting of the American Society for Bone and Mineral Research. Nashville, TN, USA; 2005.
[121] Allen MR, Burr DB. Changes in vertebral strength-density and energy absorption-density relationships following bisphosphonate treatment in beagle dogs. Osteoporos Int 2008;19: 95-9.
[122] Garnero P, Hausherr E, Chapuy MC, Marcelli C, Grandjean H, Muller C, Cormier C, Breart G, Meunier PJ, Delmas PD. Markers of bone resorption predict hip fracture in elderly women: the EPIDOS Prospective Study. J Bone Miner Res 1996;11: 1531-8.
[123] Garnero P, Sornay-Rendu E, Claustrat B, Delmas PD. Biochemical markers of bone turnover, endogenous hormones and the risk of fractures in postmenopausal women: the OFELY study. J Bone Miner Res 2000;15: 1526-36.
[124] Melton LJ, 3rd, Khosla S, Atkinson EJ, O'Fallon WM, Riggs BL. Relationship of bone turnover to bone density and fractures. J Bone Miner Res 1997;12: 1083-91.
[125] Chapurlat RD, Garnero P, Breart G, Meunier PJ, Delmas PD. Serum type I collagen breakdown product (serum CTX) predicts hip fracture risk in elderly women: the EPIDOS study. Bone 2000;27: 283-6.
[126] Ross PD, Kress BC, Parson RE, Wasnich RD, Armour KA, Mizrahi IA. Serum bone alkaline phosphatase and calcaneus bone density predict fractures: a prospective study. Osteoporos Int 2000;11: 76-82.
[127] Chesnut CH, 3rd, Bell NH, Clark GS, Drinkwater BL, English SC, Johnson CC, Jr., Notelovitz M, Rosen C, Cain DF, Flessland KA, Mallinak NJ. Hormone replacement therapy in postmenopausal women: urinary N-telopeptide of type I collagen monitors

therapeutic effect and predicts response of bone mineral density. Am J Med 1997;102: 29-37.
[128] Bjarnason NH, Sarkar S, Duong T, Mitlak B, Delmas PD, Christiansen C. Six and twelve month changes in bone turnover are related to reduction in vertebral fracture risk during 3 years of raloxifene treatment in postmenopausal osteoporosis. Osteoporos Int 2001;12: 922-30.
[129] Bauer DC, Garnero P, Hochberg MC, Santora A, Delmas P, Ewing SK, Black DM. Pretreatment levels of bone turnover and the antifracture efficacy of alendronate: the fracture intervention trial. J Bone Miner Res 2006;21: 292-9.
[130] Unnanuntana A, Gladnick BP, Donnelly E, Lane JM. The assessment of fracture risk. J Bone Joint Surg Am 2010;92: 743-53.
[131] van der Linden JC, Birkenhager-Frenkel DH, Verhaar JA, Weinans H. Trabecular bone's mechanical properties are affected by its non-uniform mineral distribution. J Biomech 2001;34: 1573-80.
[132] Jaasma MJ, Bayraktar HH, Niebur GL, Keaveny TM. Biomechanical effects of intraspecimen variations in tissue modulus for trabecular bone. J Biomech 2002;35: 237-246.
[133] Mulder L, van Ruijven LJ, Koolstra JH, van Eijden TM. Biomechanical consequences of developmental changes in trabecular architecture and mineralization of the pig mandibular condyle. J Biomech 2007;40: 1575-82.
[134] Renders GA, Mulder L, Langenbach GE, van Ruijven LJ, van Eijden TM. Biomechanical effect of mineral heterogeneity in trabecular bone. J Biomech 2008;41: 2793-8.
[135] Paschalis EP, Betts F, DiCarlo E, Mendelsohn R, Boskey AL. FTIR microspectroscopic analysis of normal human cortical and trabecular bone. Calcif Tissue Int 1997;61: 480-6.
[136] Boivin G, Meunier PJ. Changes in bone remodeling rate influence the degree of mineralization of bone. Connect Tissue Res 2002;43: 535-7.
[137] Yao W, Cheng Z, Koester KJ, Ager JW, Balooch M, Pham A, Chefo S, Busse C, Ritchie RO, Lane NE. The degree of bone mineralization is maintained with single intravenous bisphosphonates in aged estrogen-deficient rats and is a strong predictor of bone strength. Bone 2007;41: 804-12.
[138] Boivin G, Meunier PJ. Effects of bisphosphonates on matrix mineralization. J Musculoskelet Neuronal Interact 2002;2: 538-43.
[139] Boivin G, Lips P, Ott SM, Harper KD, Sarkar S, Pinette KV, Meunier PJ. Contribution of raloxifene and calcium and vitamin D3 supplementation to the increase of the degree of mineralization of bone in postmenopausal women. J Clin Endocrinol Metab 2003;88: 4199-205.
[140] Allen MR, Iwata K, Sato M, Burr DB. Raloxifene enhances vertebral mechanical properties independent of bone density. Bone 2006;39: 1130-5.
[141] Kimmel DB, Bozzato RP, Kronis KA, Coble T, Sindrey D, Kwong P, Recker RR. The effect of recombinant human (1-84) or synthetic human (1-34) parathyroid hormone on the skeleton of adult osteopenic ovariectomized rats. Endocrinology 1993;132: 1577-84.
[142] Black LJ, Sato M, Rowley ER, Magee DE, Bekele A, Williams DC, Cullinan GJ, Bendele R, Kauffman RF, Bensch WR, et al. Raloxifene (LY139481 HCI) prevents bone

loss and reduces serum cholesterol without causing uterine hypertrophy in ovariectomized rats. J Clin Invest 1994;93: 63-9.
[143] Mosekilde L, Thomsen JS, McOsker JE. No loss of biomechanical effects after withdrawal of short-term PTH treatment in an aged, osteopenic, ovariectomized rat model. Bone 1997;20: 429-37.
[144] Ohnishi H, Nakamura T, Narusawa K, Murakami H, Abe M, Barbier A, Suzuki K. Bisphosphonate tiludronate increases bone strength by improving mass and structure in established osteopenia after ovariectomy in rats. Bone 1997;21: 335-43.
[145] Okimoto N, Tsurukami H, Okazaki Y, Nishida S, Sakai A, Ohnishi H, Hori M, Yasukawa K, Nakamura T. Effects of a weekly injection of human parathyroid hormone (1-34) and withdrawal on bone mass, strength, and turnover in mature ovariectomized rats. Bone 1998;22: 523-31.
[146] Fox J, Miller MA, Newman MK, Turner CH, Recker RR, Smith SY. Treatment of skeletally mature ovariectomized rhesus monkeys with PTH(1-84) for 16 months increases bone formation and density and improves trabecular architecture and biomechanical properties at the lumbar spine. J Bone Miner Res 2007;22: 260-73.
[147] Schaffler MB, Burr DB. Stiffness of compact bone: effects of porosity and density. J Biomech 1988;21: 13-16.
[148] Kaneko TS, Pejcic MR, Tehranzadeh J, Keyak JH. Relationships between material properties and CT scan data of cortical bone with and without metastatic lesions. Med Eng Phys 2003;25: 445-54.
[149] Currey JD. Tensile yield in compact bone is determined by strain, post-yield behaviour by mineral content. J Biomech 2004;37: 549-56.
[150] Raum K, Cleveland RO, Peyrin F, Laugier P. Derivation of elastic stiffness from site-matched mineral density and acoustic impedance maps. Phys Med Biol 2006;51: 747-58.
[151] Raum K, Hofmann T, Leguerney I, Saied A, Peyrin F, Vico L, Laugier P. Variations of microstructure, mineral density and tissue elasticity in B6/C3H mice. Bone 2007;41: 1017-24.
[152] Mulder L, Koolstra JH, den Toonder JM, van Eijden TM. Relationship between tissue stiffness and degree of mineralization of developing trabecular bone. J Biomed Mater Res A 2008;84: 508-15.
[153] Roschger P, Gupta HS, Berzlanovich A, Ittner G, Dempster DW, Fratzl P, Cosman F, Parisien M, Lindsay R, Nieves JW, Klaushofer K. Constant mineralization density distribution in cancellous human bone. Bone 2003;32: 316-23.
[154] Thompson DD, Simmons HA, Pirie CM, Ke HZ. FDA Guidelines and animal models for osteoporosis. Bone 1995;17: 125S-133S.
[155] Mosekilde L, Danielsen CC, Knudsen UB. The effect of aging and ovariectomy on the vertebral bone mass and biomechanical properties of mature rats. Bone 1993;14: 1-6.
[156] Faibish D, Ott SM, Boskey AL. Mineral changes in osteoporosis: a review. Clin Orthop Relat Res 2006;443: 28-38.
[157] Fratzl P, Gupta HS, Paschalis EP, Roschger P. Structure and mechanical quality of the collagen-mineral nano-composite in bone. J Mater Chem 2004;14: 2115-2123.
[158] Boskey AL. Variations in bone mineral properties with age and disease. J Musculoskelet Neuronal Interact 2002;2: 532-4.

[159] Goodenough D, Weaver K, Davis D, LaFalce S. Volume averaging limitations of computed tomography. Am J Roentgenology 1982;138: 313-316.
[160] Nuzzo S, Peyrin F, Cloetens P, Baruchel J. Quantification of the degree of mineralization of bone in three dimensions using synchrotron radiation microtomography. Medical Physics 2002;29: 2672-2681.
[161] Mulder L, Koolstra JH, Van Euden TMGJ. Accuracy of MicroCT in the quantitative determination of the degree and distribution of mineralization in developing bone. Acta Radiologica 2004;45: 769-777.
[162] Nazarian A, Snyder BD, Zurakowski D, Muller R. Quantitative micro-computed tomography: a non-invasive method to assess equivalent bone mineral density. Bone 2008;43: 302-11.
[163] Fajardo RJ, Cory E, Patel ND, Nazarian A, Laib A, Manoharan RK, Schmitz JE, DeSilva JM, MacLatchy LM, Snyder BD, Bouxsein ML. Specimen size and porosity can introduce error into microCT-based tissue mineral density measurements. Bone 2009;44: 176-84.
[164] Gourion-Arsiquaud S, Allen MR, Burr DB, Vashishth D, Tang SY, Boskey AL. Bisphosphonate treatment modifies canine bone mineral and matrix properties and their heterogeneity. Bone 2010;46: 666-72.
[165] Keaveny TM, Pinilla TP, Crawford RP, Kopperdahl DL, Lou A. Systematic and random errors in compression testing of trabecular bone. J Orthop Res 1997;15: 101-110.
[166] Morgan EF, Bayraktar HH, Keaveny TM. Trabecular bone modulus-density relationships depend on anatomic site. J Biomech 2003;36: 897-904.
[167] Kabel J, van Rietbergen B, Dalstra M, Odgaard A, Huiskes R. The role of an effective isotropic tissue modulus in the elastic properties of cancellous bone. J Biomech 1999;32: 673-80.
[168] Brennan TC, Rizzoli R, Ammann P. Selective modification of bone quality by PTH, pamidronate, or raloxifene. J Bone Miner Res 2009;24: 800-8.
[169] Fox J, Newman MK, Turner CH, Guldberg RE, Varela A, Smith SY. Effects of treatment with parathyroid hormone 1-84 on quantity and biomechanical properties of thoracic vertebral trabecular bone in ovariectomized rhesus monkeys. Calcif Tissue Int 2008;82: 212-20.
[170] Cheng Z, Yao W, Zimmermann EA, Busse C, Ritchie RO, Lane NE. Prolonged treatments with antiresorptive agents and PTH have different effects on bone strength and the degree of mineralization in old estrogen-deficient osteoporotic rats. J Bone Miner Res 2009;24: 209-20.
[171] Arita S, Ikeda S, Sakai A, Okimoto N, Akahoshi S, Nagashima M, Nishida A, Ito M, Nakamura T. Human parathyroid hormone (1-34) increases mass and structure of the cortical shell, with resultant increase in lumbar bone strength, in ovariectomized rats. J Bone Miner Metab 2004;22: 530-40.
[172] Rho JY, Tsui TY, Pharr GM. Elastic properties of human cortical and trabecular lamellar bone measured by nanoindentation. Biomaterials 1997;18: 1325-30.
[173] Rho JY, Zioupos P, Currey JD, Pharr GM. Microstructural elasticity and regional heterogeneity in human femoral bone of various ages examined by nano-indentation. J Biomech 2002;35: 189-98.

[174] Easley SK, Jekir MG, Burghardt AJ, Li M, Keaveny TM. Contribution of the intra-specimen variations in tissue mineralization to PTH- and raloxifene-induced changes in stiffness of rat vertebrae. Bone 2010;46: 1162-9.
[175] Ruppel ME, Miller LM, Burr DB. The effect of the microscopic and nanoscale structure on bone fragility. Osteoporos Int 2008;19: 1251-65.
[176] Hernandez CJ. How can bone turnover modify bone strength independent of bone mass? Bone 2008;42: 1014-20.
[177] Tkachenko EV, Slyfield CR, Tomlinson RE, Daggett JR, Wilson DL, Hernandez CJ. Voxel size and measures of individual resorption cavities in three-dimensional images of cancellous bone. Bone 2009;45: 487-92.

7. APPENDIX

7.1 The Role of Large Deformations in the Effect of Microcavities on Bone Strength

To determine the role of large deformations in the effect of microcavities on bone strength, we analyzed a subset of human trabecular bone specimens spanning a range of bone volume fractions (VB: *n*=3, BV/TV=0.05, 0.07, and 0.08; FN: *n*=2, BV/TV=0.28 and 0.36). We used the same procedure as described in the Methods section (**2.2**) except that we did not include geometric nonlinearities in the finite element analysis, thereby suppressing large deformations of the trabeculae. We found that the effect of the simulated cavities on strength was reduced by 1.4-18% in the low-density specimens, and there did not appear to be any clear pattern in the size of this effect (**Figure 7-1**). In contrast, in the high-density specimens, suppressing large deformations did not appreciably alter the effect of simulated cavities on strength (<2.6%). We conclude that the increased susceptibility of trabeculae to large deformations is one mechanism through which microcavities weaken low-density bone, and since large deformations have little effect in high-density bone, this contributes to the density-dependent effect of microcavities on bone strength.

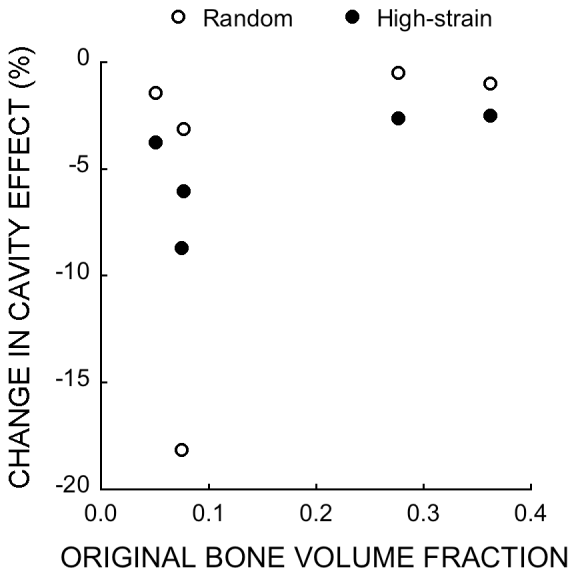

Figure 7-1: Percent change in effect of simulated microcavities on bone strength due to suppressing large deformations in the analyses of a subset of human trabecular bone from the vertebra and femoral neck.

7.2 Standard Operating Procedure for Preparing Micro-CT Images for Finite Element Analysis of Bone using Heterogeneous Tissue Modulus

University of California Berkeley
Orthopaedic Biomechanics Laboratory
Standard Operating Procedure

Preparing Micro-CT Images for Finite Element Analysis of Bone using Heterogeneous Tissue Modulus

SOP #, Version 1
Date: August 13, 2010

Authors: Sarah Easley and Narges Kaynia
Principle Investigator: Tony M. Keaveny

Summary: The following SOP explains the necessary steps and procedures for preparing a calibrated micro-CT image for a finite element analysis of bone using a heterogeneous tissue modulus. IDL is the program used for image processing. The SOP covers the preprocessing of the image including using a mask that is fitted on the image to filter out the background and removing ring artifacts from the image. Then the steps of converting the final edited image into the finite element input file is covered. Some basic understanding of IDL and conducting homogeneous FE analyses with Olympus is assumed. This procedure was developed from Sarah Easley's lab notebook "Pfizer Rat II".

Key Words: Image processing, Heterogeneous tissue modulus, IDL, Mask fitting, Ring artifacts, Converting into FE-file

---

I. PREPROCESSING IMAGE

1. Get/move the image file and unzipping

The file sent from UCSF (or other scanning facility) will likely be in the format XXXX.aim.gz where XXXX is the file name given to the specimen by the scanner.

1.1 Example of moving the files to folder "GeneralTesting":

```
[kaynia@biomech8 ~]$ ls
bin             C0004839_CONCAT_SEG.AIM.gz  Desktop
learnunixstuff
```

```
C0004839.aim.gz  connect                    idl      Tutorial
[kaynia@biomech8 ~]$ mkdir GeneralTesting
[kaynia@biomech8 ~]$ mv C0004839* GeneralTesting
[kaynia@biomech8 ~]$ ls
bin  connect  Desktop  GeneralTesting  idl  learnunixstuff
Tutorial
[kaynia@biomech8 ~]$ cd GeneralTesting/
[kaynia@biomech8 GeneralTesting]$ ls
C0004839.aim.gz  C0004839_CONCAT_SEG.AIM.gz
```

1.2 Example of unzipping the files:

```
[kaynia@biomech8 GeneralTesting]$ gunzip C0004839*
[kaynia@biomech8 GeneralTesting]$ ls
C0004839.aim  C0004839_CONCAT_SEG.AIM
```

2. Converting the file into IDL-format

Open IDL from the folder the file is in and convert it into IDL-format. Use IDL function "*read_aim*" (at least v020) which prints a log containing micro-CT scanning information and then loads the images into an IDL variable, for example "*vol*" which can then be saved into a file with extension ".*vol*".

2.1 Example of converting the image file using the IDL function "read_aim":

```
IDL> read_aim,vol,/log
Volume filename [image.aim]:C0004839.aim
```

2.2 Important information from the log file printed out during AIM-file conversion (see example below):

- Section 4: Provides grayscale-to-density calibration information. Gives the slope and intercept of the linear relationship between the grayscale value (x-value) and the density (y-value). Also gives mu_scaling needed in conversion. Specifically, to convert grayscale values into tissue mineral density:

  linear_attenuation = 16-bit_grayscale_value / mu_scaling
  density = m * linear_attenuation + b

- Section 6: Gives the size and position of the image in voxels (x, y, z values) and the size (resolution) of each voxel in mm.

```
Reading AIM v020...
!
! Processing Log
!
!-------------------------------------------------------------------
Created by                    ISQ_TO_AIM (IPL)
Time                          22-MAY-2007 11:01:27.35
Original file
dk0:[microct.data.00003227.00004956]c0004839.isq
!-------------------------------------------------------------------
Patient Name                  Keaveny Rat Spines; LV-2 101
Index Patient                                    3227
```

```
Index Measurement                                4956
!-----------------------------------------------------------------
Site                                               4
Scanner ID                                      4009
Scanner type                                      10
Position Slice 1 [um]                          61753
No. samples                                     4096
No. projections per 180                         1023
Scan Distance [um]                             12288
Integration time [us]                         200000
Reference line [um]                                0
Reconstruction-Alg.                                3
Energy [V]                                     55000
Intensity [uA]                                   144
Angle-Offset [mdeg]                                0
Default-Eval                                       0
!-----------------------------------------------------------------
Mu_Scaling                                      4096
Calibration Data             55 kVp, BH: 200 mg HA/ccm, Scaling
4096
Calib. default unit type     2 (Density)
Density: unit                mg HA/ccm
Density: slope                        2.62261993e+02
Density: intercept                   -1.54682999e+02
HU: mu water                                  0.54710
!-----------------------------------------------------------------
Parameter name               Linear Attenuation
Parameter units              [1/cm]
Minimum value                               -4.11035
Maximum value                                7.99976
Average value                                1.60516
Standard deviation                           1.68210
Scaled by factor                                4096
Minimum data value                       -16836.00000
Maximum data value                       32767.00000
Average data value                        6574.72363
Standard data deviation                   6889.86475
!-----------------------------------------------------------------
Input volume dimensions:         730         612         491
Input volume position:          707         886          59
Input volume offset:            0           0           0
Input volume element size:   0.00600000   0.00600000   0.00600000
Reading 16bit image data...
```

3. Making/Saving the image as a 16-bit file.

Use "*scanvol,vol*" to view the image volume. Note that the image will be in 16-bit format which contains more grayscale values than the computer monitor can display, so you have to use "*bytscl(vol)*" to temporarily convert it into an 8-bit image so that it can be viewed. Use "*write_intdat,'file_name',vol*" to save the file in a 16-bit format. When defining the new file name, specify: the name of the specimen, 16bit, and the volume's voxel dimensions.

3.1 Example of making the image stored in variable "*vol*" into a 16-bit image:

```
IDL> scanvol,vol
IDL> scanvol, bytscl(vol)
IDL> write_intdat,'C0004839.16b.730.612.491.vol',vol
```

II. PREPROCESSING MASK

4. Opening and saving the mask.

We will put a mask on top of the 16-bit picture to separate out the grayscale bone from the background of the picture which is made black. In general, this mask is the typical segmented (*i.e.* thresholded) image, which may be created locally with IDL by either choosing a threshold value to match the bone volume fraction of the image to an experimental measure (preferred) or by visually matching the details of the bone geometry in the segmented image to those in the original grayscale image, or with the Scanco software at UCSF (as was the case in this example, because experimental volume measurements were not available; here, the segmented image contained two grayscale values — one for the cortex and the other for the trabecular compartment — and was named "XXXX_CONCAT_SEG.AIM").

4.1 Example of opening a mask created with Scanco software and giving it the arbitrary IDL variable name *"vol2"*. The scanner log file follows; again, the volume voxel dimensions and resolution are given near end of log file. Note: if mask is created from segmented image created locally, you can skip this step.

```
IDL> read_aim,vol2, /log
% Compiled module: READ_AIMV16.
Volume filename [C000XXXX.AIM]:C0004839_CONCAT_SEG.AIM
Reading AIM v020...
 Processing Log
!-------------------------------------------------------------------
Created by                    ISQ_TO_AIM (IPL)
Time                          22-MAY-2007 11:01:27.35
Original file
dk0:[microct.data.00003227.00004956]c0004839.isq
!-------------------------------------------------------------------
Patient Name                  Keaveny Rat Spines; LV-2 101
Index Patient                                    3227
Index Measurement                                4956
!-------------------------------------------------------------------
Site                                                4
Scanner ID                                       4009
Scanner type                                       10
Position Slice 1 [um]                           61753
No. samples                                      4096
No. projections per 180                          1023
Scan Distance [um]                              12288
Integration time [us]                          200000
Reference line [um]                                 0
Reconstruction-Alg.                                 3
Energy [V]                                      55000
Intensity [uA]                                    144
Angle-Offset [mdeg]                                 0
```

```
Default-Eval                                          0
!-------------------------------------------------------------------
Mu_Scaling                                         4096
Calibration Data              55 kVp, BH: 200 mg HA/ccm, Scaling
4096
Calib. default unit type      2 (Density)
Density: unit                 mg HA/ccm
Density: slope                         2.62261993e+02
Density: intercept                    -1.54682999e+02
HU: mu water                                  0.54710
!-------------------------------------------------------------------
Parameter (before) name       Linear Attenuation
Parameter units               [1/cm]
Minimum value                               -4.11035
Maximum value                                7.99976
Average value                                1.60516
Standard deviation                           1.68210
Scaled by factor                                4096
Minimum data value                       -16836.00000
Maximum data value                       32767.00000
Average data value                        6574.72363
Standard data deviation                   6889.86475
!-------------------------------------------------------------------
Procedure:                    D3P_SupGaussThres()
sigma                                        1.20000
support                                            2
Wished Unit of thresholds                          6
low_th_input                              450.00000
low corresponds to data value                 14745
and low to mu value (if mu)                 3.59985
and low to dens value                     789.42175
           dens in units      mg HA/ccm
and low to HU value                      5579.88232
upp_th_input                             1000.00000
upp corresponds to data value                 32767
and upp to mu value (if mu)                 7.99976
and upp to dens value                    1943.34900
and upp to HU value                     13622.10938
in_range_value                                  127
Parameter (before) name             Segmented Objects
Parameter units                             [object]
Minimum value                                0.00000
Maximum value                              127.00000
Average value                               24.04918
Standard deviation                          49.75824
Scaled by factor                                   1
Minimum data value                           0.00000
Maximum data value                         127.00000
Average data value                          24.04918
Standard data deviation                     49.75824
!-------------------------------------------------------------------
Procedure:                    D3P_GobjOrAimMaskAimPeel_OW()
Gobj File:
dk0:[microct.data.00003227.00004956]c0004839.gobj
Cutborder                     False
Peel Iterations                                    0
Gobj: Rel. Vol. of set AIM                0.16693395
```

```
Gobj: of Set Vol(dim-2*off) of AIM           724        608
487
Parameter (before) name             Segmented Objects
Parameter units                              [object]
Minimum value                                 0.00000
Maximum value                               127.00000
Average value                                47.02511
Standard deviation                           61.32559
Scaled by factor                              1.00000
Minimum data value                            0.00000
Maximum data value                          127.00000
Average data value                           47.02511
Standard data deviation                      61.32559
!-------------------------------------------------------------------
Procedure:                    D3P_Multiply_Constant_OW()
Multiplication with                          -1.00000
Parameter (before) name              Segmented Objects
Parameter units                               [object]
Minimum value                               127.00000
Maximum value                                 0.00000
Average value                                47.02511
Standard deviation                          -61.32559
Scaled by factor                             -1.00000
Minimum data value                         -127.00000
Maximum data value                            0.00000
Average data value                          -47.02511
Standard data deviation                      61.32559
!-------------------------------------------------------------------
Procedure:                    D3P_Multiply_Constant_OW()
Multiplication with                          -1.00000
Parameter (before) name              Segmented Objects
Parameter units                               [object]
Minimum value                                 0.00000
Maximum value                               127.00000
Average value                                47.02511
Standard deviation                           61.32559
Scaled by factor                              1.00000
Minimum data value                            0.00000
Maximum data value                          127.00000
Average data value                           47.02511
Standard data deviation                      61.32559
!-------------------------------------------------------------------
Procedure:                    D3P_Concatenate()
Add (False = Overlay)         False
Common Region only            False
Shift of in2                        0          0          0
Turn Angle of in2                   0.00000
Turnpoint (global) of in2           0          0
!
Parameter name                       Segmented Objects
Parameter units                               [object]
Minimum value                                -1.00000
Maximum value                               127.00000
Average value                                46.26103
Standard deviation                           61.91018
Scaled by factor                              1.00000
Minimum data value                           -1.00000
```

```
Maximum data value                          127.00000
Average data value                           46.26103
Standard data deviation                      61.91018
!-------------------------------------------------------------------
Input volume dimensions:       724         608         487
Input volume position:         710         888          61
Input volume offset:           0           0           0
Input volume element size:   0.00600000   0.00600000   0.00600000
```

4.2 View the mask *"vol2"* with "*scanvol,vol2*", and save it using "*write_bindat*":

```
IDL> scanvol,vol2
IDL> write_bindat,'C0004839.8b.724.608.487.vol',vol2
```

5. Apply the mask to the grayscale image.

We will fit the mask so that it is placed on top of the 16-bit image to produce a filtered grayscale image of the bone in which the background is made black (**Figure 7-2**); note that it is important that the two images are positioned such that they exactly overlap. This may involve cropping and/or shifting one image, depending on how the mask was developed. For example, if the mask was created with the Scanco software, as in this example, position information is given in the *read_aim* log files that can be used to align the two images. Use IDL custom function "*gray_filter2*"; the command is given in the following way:

gray_filter2, 'name of 16b image file', size, position, 'name of mask file', size, position, m,b

where *position* indicates those given in each of the the *read_aim* log files, *m* is the slope and *b* is the intercept of the density-grayscale relationship given in the scanner log file printed from *read_aim* of the grayscale image. The *gray_filter2* function automatically shifts the images to align their positions. If the mask image was created locally, such that the positions are equivalent, just enter *0,0,0* as the position for both images. The *gray_filter2* function prints out summary statistics for the 16-bit grayscale values in the filtered image, and calculates the mean tissue mineral density (with no voxels eroded).

5.1 Example of fitting the mask on the image:

```
IDL>
gray_filter2,'C0004839.16b.730.612.491.vol',730,612,491,707,886,
59,'C0004839.8b.724.608.487.vol',724,608,487,710,888,61,'assembl
edvol',2.62261993e+02,-1.54682999e+02
          3         724         608         487           2
214373504
          3         724         608         487           1
214373504
fraction of negative voxels:   3.45266e-08
voxels: 40594530, max: 32767.0, mean: 19973.4, min: 67.000
, sd:      2427.55
density:      1124.19
```

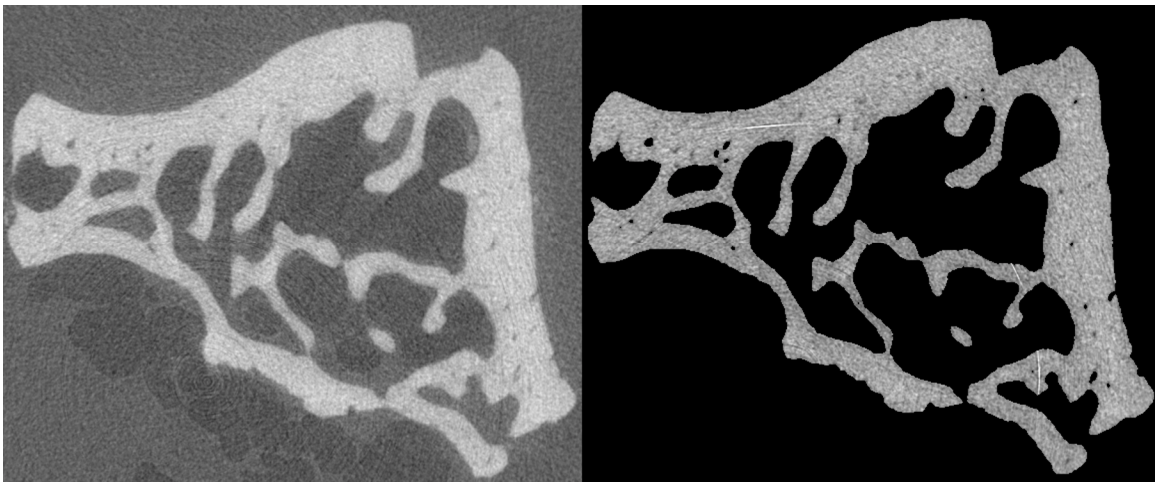

Figure 7-2: The same transverse slice of a rat vertebra before (left) and after (right) applying the mask with the "gray_filter2" IDL function.

6. **Renaming and loading files into IDL**

We give the filtered image file (the image after the mask is applied) a new name, so that it contains the size etc. Opening IDL and loading the new file giving it a temporary arbitrary variable name *"vol3"*.

6.1 Example of giving image file a new name (Note: this step can be omitted if the full name is provided in the *gray_filter* command, i.e., instead of 'assembledvol', you could directly prescribe 'assembledvol.16b.724.608.487.vol':

```
[kaynia@biomech4 GeneralTesting]$ ls
assembledvol       C0004839.8b.724.608.487.vol      ManualSteps~
C0004839.16b.730.612.491.vol  ManualSteps
[kaynia@biomech4 GeneralTesting]$ mv assembledvol
assembledvol.16b.724.608.487.vol
[kaynia@biomech4 GeneralTesting]$ ls
assembledvol.16b.724.608.487.vol  C0004839.8b.724.608.487.vol
ManualSteps~     C0004839.16b.730.612.491.vol      ManualSteps
```

6.2 Example of loading 16-bit file into IDL:

```
[kaynia@biomech4 GeneralTesting]$ IDL
IDL Version 6.2 (linux x86_64 m64). (c) 2005, Research Systems,
Inc.
Installation number: 213000.
Licensed for use by: UC Berkeley
IDL>
read_intdat,'assembledvol.16b.724.608.487.vol',vol3,724,608,487
IDL> scanvol,bytscl(vol3)
```

7. **Creating an 8-bit image from 16-bit image**

The maximum number of materials that we can use in our finite element models is 254 (since material 255 is automatically mapped to material 1 for use in homogeneous analyses of segmented binary images). As such, we must convert the 16-bit filtered image file into an 8-bit image, specifying that the upper grayscale limit is 254. Afterwards, we can print out image statistics to find the mean, SD, min, max, etc. of the grayscale values in the image. Save the 8-bit image under a new name, following the same naming convention.

7.1 Example of converting into 8-bit:

```
IDL> vol4=bytscl(vol3,TOP=254)
IDL> scanvol,vol4
IDL> nonzeromask= vol4 ne 0
IDL>
image_statistics,vol4,COUNT=elementno,MASK=nonzeromask,MAXIMUM=vo
lumeMax, MEAN=VolumeMean, MINIMUM=VolumeMIN,STDDEV=vsd,
VARIANCE=vvar
IDL> print, elementno, volumeMax,VolumeMean,VolumeMIN,vsd,vvar
      40594529   254.000   154.933   5.00000   18.8936    356.969
IDL> write_bindat,'assembledvol.8b.724.608.487.vol',vol4
```

III. FINAL EDITING OF THE IMAGE

8. Removing ring artifacts

Some images have ring artifacts that result from the scanning process (appear as lines/circles, **Figure 7-3 A**) that should be removed or minimized before the FE analysis. *Note that the function described in this section could be modified to operate on the 16-bit image prior to converting into an 8-bit image.*

8.1 A ring artifact may be either brighter or darker than the surrounding bone. The general approach here is to identify ring artifacts, and then replace the artificially high or low grayscale values with a value that is an average of the surrounding tissue. To do this, custom IDL functions, "*artifact*" and "*artifact2*" (for bright and dark artifacts respectively), have been written. Use the function as follows:

```
artifact,'grayscale.8bit.vol',vol,x,y,z-size,artifact-
threshold,max-affected-vol-fraction,'output.8bit.vol'
```

First, plot histograms of ONE slice affected by an artifact (it will be easier to see what grayscale values the artifacts are occurring at in one slice than for the entire volume) and find the second small local peak(s) that represents the artifact (**Figure 7-3 B**). Choose a value that clearly thresholds out this second peak (typically, a value of about 230 for bright artifacts or about 80 for dark artifacts); also choose a maximum volume fraction that you will accept as being modified by the script (typically about 0.005 is accepted). These are inputs to the IDL function.

Example of making histogram of the filtered image (black background) from which to select the threshold values for removing the artifacts:

```
IDL> h=histogram(vol(*,*,slice#),min=1,max=255)
IDL> plot,h
```

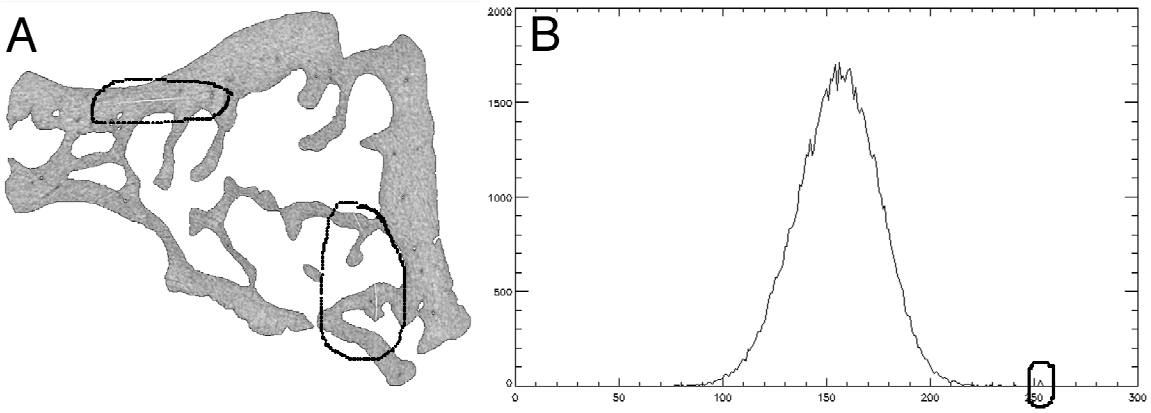

Figure 7-3: A transverse slice of a rat vertebra containing bright ring artifacts (left) and the histogram of that slice (right).

8.2 There are two functions that edit the grayscale values of voxels in the volume. The function "artifact" removes points above a given value (bright artifacts). The file "artifact2" removes points below a given value (dark artifacts). The function prints out the number of slices in the volume that were modified and the mean and standard deviation of the grayscale values in the modified volume. We call the last result file "final……."

Example of removing the artifacts when threshold values are 230 and 80.

```
IDL>
artifact,'assembledvol.8b.724.608.487.vol',vol5,724,608,487,2
30,0.005,'output.8b.724.608.487.vol'
number of affected slices:        0
new mean +/- SD (range):       154.933,       18.8936 (
5.00000-
      254.000)
IDL>
artifact2,'output.8b.724.608.487.vol',vol6,724,608,487,80,0.0
05,'final.8b.724.608.487.vol'
number of affected slices:        0
new mean +/- SD (range):       154.933,       18.8936 (
5.00000-
      254.000)
```

VI. PREPARING FOR FE-ANALYSIS

9. Connecting the image.

We want to get rid of all disconnected voxels so that the image is connected and the finite element analysis can be performed without any instability problems.

9.1 Example of connecting our final file using the "*connect*" program

```
[kaynia@biomech4 GeneralTesting]$ $HOME/bin/connect -v
final.8b.724.608.487.vol -x 724 -y 608 -z 487 -o
final.8b.724.608.487.vol.connect
nbytes=214373504
nelements = 40594529

Element sweeping algorithm
   maximum number of sweeps set to: 2172

Table III: voxel groups
   group   |  #sweeps  |  #voxels
-----------+-----------+-----------
         2 |        10 |  40584250  40584250
 Largest group found, search ended
-----------------------------------

Table IV: Results voxel sweep
-----------------------------------------+----------
   largest group                         |         2
   number of bone voxels in this group|  40584250
   number of non-connected bone voxels|     10279
-------------------------------------------------
 40584250 elements
Assigning boundary conditions: Done
Writing final.8b.724.608.487.vol.connect: Done
```

9.2 Example of loading the FINAL file into IDL and viewing it for check:

```
[kaynia@biomech4 GeneralTesting]$ idl
IDL>
read_bindat,'final.8b.724.608.487.vol.connect',vol7,724,608,48
7
IDL> scanvol,vol7
```

10. Creating an FE input file (*.feap*) with the node code for analysis with Olympus

As with homogeneous models, the node code (e.g. "*node_new_softlayer*") is used to generate the input file (*.feap*) for Olympus. The only difference between the heterogeneous and homogeneous models for this step is the number of materials. Here, the number of materials will be equal to the maximum grayscale value in the image (typically, this will be 254), regardless of whether there are actually voxels with every value up to 254.

Sample header from *.feap* file showing that there are 254 materials in model:

```
FEAP xyconstrained_1%compression_ratVB
  11830999  10031656       254         3         3         8
<remainder of file omitted for brevity>
```

11. Creating material file 'mate' before running the analysis in Olympus

The remaining part is running the finite element analysis using the prepared final image-file. The only **important** difference from a regular homogenous FE analysis is mainly in the MATERIAL FILE ("*mate*", see page 54 in Sarah Easley's labnotes). In a "*mate*" file for a homogeneous analysis, there is only one material defined. For the heterogeneous analyses, the "*mate*" file will have up to 253 materials (material #2-254), where the grayscale values in the image will be directly mapped to that material number (note that the materials numbers must **start at 2 and be sequential up to the maximum value**, even if there are no materials defined for certain grayscale values).

It is straightforward to convert the grayscale values to tissue density using the calibration information given with the scanner; see section 2.2. However, the relationship between the tissue density and the tissue modulus is not well established. There is a relationship in Sarah Easley's labnotes derived by plotting data from the literature for a variety of testing methods, species, and anatomic sites and taking a power-law fit (this was used in Easley et al, Bone, 2010). Depending on the application, and as new data is developed, an updated relationship may be more appropriate.

To create a "*mate*" file with 253 materials (2-254), use a custom Python script (e.g. "*createMateLin6.py*" that was used for analyses in Easley et al. Bone, 2010). The script combines the grayscale-to-density and the density-to-modulus relationships in one operation and automatically writes out the "*mate*" file. Note that there are variables containing the scanner calibration data that will need to be updated for a different batch of scans.

Sample "*mate*" file:

```
mate,2
solid
elastic,isotropic,1000*0.001,0.3

mate,3
solid
elastic,isotropic,1000*0.001,0.3

<mate 4-252 omitted for brevity>

mate,253
solid
elastic,isotropic,1000*61.009,0.3

mate,254
solid
elastic,isotropic,1000*61.464,0.3
```

V. CALCULATING TISSUE MINERAL DENSITY

12. Removing outer layers of voxels for calculations of tissue mineral density.

The grayscale values in the calibrated micro-CT scan scan are used to estimate tissue mineral density in the specimen (note that this measure is sometimes called TMD — tissue mineral density — or DMB — degree of mineralization of bone — in the literature). In addition to using this information to assign elastic modulus to each element in the FE model, this can also be used to determine the mean TMD, standard deviation (SD) of the TMD, and coefficient of variation (CV) of TMD, as well as other summary statistics for each specimen. Because of beam hardening and volume averaging artifacts, the outer two layers of voxels are typically eroded from the bone surfaces before making these measurements.

The custom IDL function "*erodesurfs2*" calculates the mean, standard deviation, and coefficient of variation of the density for a 16-bit filtered (black backgound) volume file for 0, 1, and 2 voxel layers eroded from the surfaces. You must supply the density calibration information from the scanner. Note that there are additional scripts, "*erodesurfs3*" and "*erodesurfs4*", that take in a an 8-bit trabecular compartment and cortex, respectively, to be used as masks to calculate the density in those compartments only if they have been separated, as was the case in this example. A Python script "*getDensity2*" exists to recursively extract the density information from a series of specimen folders after running "*erodesurfsX*" to make compiling in a spreadsheet more efficient.

For more detailed information about the distribution of the density within a bone specimen, custom IDL function "*histo_erode*" and "*quant_histo*" were developed to calculate characteristics of the histogram of the grayscale values, as described in Roschger et al 2008. This includes the mean, peak, width at half height. Again, this is done for 0, 1, and 2 voxels eroded from the surfaces. Currently, this function operates on an 8-bit grayscale image with black background (not a 16-bit image, though this could be updated).

7.3 Standard Operating Procedure for Specimen Preparation of Whole Rat Vertebrae for Biomechanical Testing

University of California Berkeley
Orthopaedic Biomechanics Laboratory
Standard Operating Procedure

Specimen Preparation of Whole Rat Vertebrae for Biomechanical Testing

SOP #, Version 1
Date: 4/12/07

Author:
Principle Investigator: Tony M. Keaveny

Summary: This document summarizes the method of embedding the rat VB and removing the endplates to obtain a specimen with planoparallel ends that is approximately the middle 50% of the original VB and is parallel to the long axis of the original VB.

Key Words: Rat vertebral bodies, embedding, PMMA, Isomet

Materials:

Rat VB's,
Jig,
Laboratory stand (4),
Burette clamp (4),
_____,
Bosworth Fastray powder and liquid,
Peel-A-Way plastic embedding molds VWR P/N _____,
Forceps with roughened tips,
Base-mounted tweezers with rubber tips (4),
4" Isomet blade P/N _____,
Absorbent pads,
Digital calipers,
Several 0.625" dia x 0.08" thick discs of 304 SS
Ultrasonic cleaner
Scissors
Rubber-tipped tweezers,
Loctite 401,
SS swivel pad MSC P/N
Digital camera
Scalpels with #22 blades
Set of standard Allen keys
3/8" crescent wrench
Nail clippers
Gauze
Sharpies
1.5 oz. specimen containers
Glass vials

I. PROCEDURE

1.0 Dissection and Cleaning

1.0 Thaw specimens if needed.
1.1 Use a scalpel and forceps to remove as much soft tissue as possible.
1.2 Place 6 specimens in glass vials filled with DI water and place in ultrasound bath for 10 min.
1.3 Water jet each specimen for 1-2 min at moderate pressure. Use scalpel and tweezers to remove any loose tissue.
1.4 Repeat steps 1.2-1.3 until specimen is sufficiently clean for embedding (3 cycles total should suffice). Use fresh DI water each time.

2.0 Embedding

2.1 Set up four stations with the base-mounted tweezers hanging vertically from the burette clamp attached to the stand.
2.2 Place an embedding mold on each jack below the base-mounted tweezers.
2.3 Affix a VB in each pair of tweezers such that the long axis of each VB is horizontal.
2.4 Mix equal amounts of Bosworth Fastray powder and liquid for 75 seconds.
2.5 Pour the mixture up to the top of each mold and QUICKLY raise the each jack so that the posterior elements of the VB are mostly submerged in the mixture. The body of the VB should not make contact with the surface of the mixture.
2.6 Place a tiny roll of saline-soaked gauze on top of each VB inside the tweezers and leave specimen for 1 hour to let the PMMA harden.
2.7 Remove each specimen from the tweezers, wrap saline-soaked gauze around each VB and store overnight in refrigerator (4°C) to allow PMMA to finish curing.

3.0 Cutting

3.1 Cut six slices off a dressing stick @ 175 rpm to sharpen the saw blade.
3.1 Screw the swivel pad into the jig and glue the swivel pad to the center of the SS disc using Loctite.
3.2 Remove gauze from first specimen and check that specimen is firmly embedded.
3.3 Remove disc material from each VB with a scalpel.
3.2 Take three measurements of length at 90° intervals. Calculate average height, H.
3.3 Place specimen in jig with inferior side towards Isomet arm.
3.3 Adjust the four allen screws so that the rat VB is horizontal and perpendicular to the Isomet arm.
3.3 Move blade to against inferior side of VB and zero the position.
3.3 Raise Isomet arm and move blade to the right H/4 mm.
3.4 Adjust speed to 250 rpm and make one cut all the way through the VB.
3.3 Raise Isomet arm and move blade (H/2 + BW) to the right, where BW = Blade Width = 0.26 mm ≅ 0.3 mm
3.3 Make a second cut at 250 rpm.

3.4 Remove desired portion and measure height 4 times with calipers at 90° intervals. Calculate the mean.
3.3 Calculate maximum percentage variation in specimen height to determine planoparallelism. Value should be les than 1.5% of mean height.
3.3 Repeat steps 3.3 to3.xx for all other VBs.

7.4 Standard Operating Procedure for Compressive Testing of Whole Rat Vertebrae on the MTS

University of California Berkeley
Orthopaedic Biomechanics Laboratory
Standard Operating Procedure

Compressive Testing of Whole Rat Vertebrae on the MTS

SOP #, Version 2
Date: 4/12/07

Author:
Principle Investigator: Tony M. Keaveny

Summary: This document summarizes the method for compressive testing of whole rat vertebral bodies with the endplates removed.

Key Words: Rat vertebral bodies, mechanical testing, MTS

Materials: Rat VBs, MTS test frame, top and bottom platens, adapter plate, absorbent pads, 1” extensometer, 250-lb load cell, calipers, rubber-tipped tweezers

---

I. PROCEDURE

Before beginning this procedure, ensure that the MTS platens are aligned optimally and the crosshead is at the optimal height. Start and warm up MTS (see SOP entitled “MTS System Startup”).

1.1 Divide mean specimen height by 25.4. Use this ratio to calculate extensometer strain or strain rate values corresponding to 0.3%, 8% and 0.5%/s.
1.2 In TestWare, program 5 preload cycles to 0.3% specimen strain and a ramp to 8% specimen strain, all at a rate of 0.5% specimen strain per second.
1.3 Place VB on bottom platen.
1.4 Lower top platen to just above top of VB. Change displacement range to 10 mm.
1.5 Go to displacement control and zero load.
1.6 Lower top platen onto the specimen VERY SLOWLY until load reads ~5 N.
1.7 Add extensometer, remove pin, zero strain value and check offset (ε offset should be < 7%).
1.8 Go to load control, zero displacement, then return to displacement control.
1.9 Check interlocks: Load value is +/- 800N, strain is +/- 4%, all others disabled.
1.10 Turn on scope.
1.11 Check procedure and file name in TestWare, then execute test.
1.12 Check that strain has returned to zero, insert extensometer pin and remove extensometer.
1.13 In Testware, close data file, control -> reset. Repeat entire procedure for each specimen.

DATE:_____

TestStar File Path: _____

TestWare File Path: _____

Specimen # _____

H1_____ H2_____ H3_____ H4_____ $\mathbf{H_{AVG}}$_____

0.003_____ 0.005_____ 0.08_____

Initial load_____ Peak Load?_____ Pre-test_____

Pin out? _____ Interlocks?_____ Offsets? _____

Comments_____

_____

Specimen # _____

H1_____ H2_____ H3_____ H4_____ $\mathbf{H_{AVG}}$_____

0.003_____ 0.005_____ 0.08_____

Initial load_____ Peak Load? _____ Pre-test_____

Pin out? _____ Interlocks?_____ Offsets? _____

Comments_____

_____